Dynamic control of magnetization for spintronic applications studied by magneto-optical methods

Martin Zahradník

Dynamic control of magnetization for spintronic applications studied by magneto-optical methods

Thèse de doctorat de l'Université Charles
et de l'Université Paris-Saclay
préparée à l'Université Paris-Sud

Institute of Physics of Charles University
Spécialité de doctorat : Optique quantique et optoélectronique

École doctorale n°575 Physique et ingénierie : Electrons, Photons, Sciences du vivant (EOBE)
Spécialité de doctorat : Électronique et optoélectronique, nano- et microtechnologie

Thèse présentée et soutenue à Prague, le 28 juin 2019, par

Martin Zahradník

Composition du Jury :

Prof. Ing. Jan Franc, DrSc. Charles University	Président
Ing. Dominik Legut, Ph.D. VSB Technical University of Ostrava	Rapporteur
Dr. Gervasi Herranz Institute of Materials Science of Barcelona ICMAB-CSIC	Rapporteur
Dr. André Thiaville Université Paris-Sud (LPS)	Examinateur
RNDr. Martin Veis, Ph.D. Charles University	Directeur de thèse
Prof. Philippe Lecoeur Université Paris-Sud (C2N)	Co-Directeur de thèse

I declare that I carried out this doctoral thesis independently, and only with the cited sources, literature and other professional sources.

I understand that my work relates to the rights and obligations under the Act No. 121/2000 Sb., the Copyright Act, as amended, in particular the fact that the Charles University has the right to conclude a license agreement on the use of this work as a school work pursuant to Section 60 subsection 1 of the Copyright Act.

In date

First and foremost, I would like to express my thanks and my deep appreciation to Dr. Martin Veis, who has been my supervisor for nearly ten years. He was leading me with great patience and understanding throughout my studies, first as a teacher, then becoming a supervisor during my bachelor studies, and finally standing at my side as a friend and collegue, helping me selflessly on my academic journey. Thank you!

I am very grateful to my supervisor Prof. Philippe Lecoeur for the opportunity to become a part of his research group during my doctoral studies. His exceptional kindness in combination with his tremendous knowledge was truly inspirational to me.

Great thanks are addressed to Dr. Klára Uhlířová for her essential help with measurements of magnetic force microscopy and SQUID magnetometry, as well as for her guidance, knowledge and effort dedicated to help me learn more about these areas of research.

I would like to express my special thanks to the two closest collegues from the Centre for Nanoscience and Nanotechnology. To Dr. Thomas Maroutian for his essential help with pulsed laser deposition and X-ray diffraction, for his attentive reading of my thesis manuscript, as well as for the moments of laughter that always brightened up my dark days. To Dr. Guillaume Agnus for his indispensable help with cleanroom processing, as well as for his attentive care that helped me many times to overcome the administrative difficulties, and to make my stay in France much easier.

I am also thankful to other collegues, who significantly contributed to the present thesis. To Dr. Nicolas Vernier for his essential help with magneto-optical Kerr effect microscopy. To Dr. Martin Zelený for his important contribution of the *ab initio* calculations. To Dr. Lukáš Horák for his fundamental help with analysis of X-ray diffraction data.

I am greatful for sharing my office with few special people, who made my hard working days easier. Thank you Dr. Georg Kurij, you helped me more than you think. Thank you Abdelnour Benamar. Thank you Lukáš Beran.

I am thankful for the opportunity to work in research teams full of amazing, brilliant people. I would like to thank all the collegues from the laboratory of magneto-optics: Prof. Štefan Višňovský, Assoc. Prof. Miroslav Kučera, Dr. Roman Antoš, Dr. Eva Jakubisová, Dr. Rathaiah Mamilla, Kristupas Kazimieras Tikuišis, Vojtěch Kletečka and Tomáš Maleček. I could also not forget the former collegues: Dr. Zuzana Lučeničová, Dr. Martin Hanuš, Eva Jesenská, Lukáš Ohnoutek and Jan Dušek. Last, but not least, I would like to thank all my collegues from the oxide team as well: Prof. Pascal Aubert, Dr. Sylvia Matzen, Dr. Ngoc Nguyen, Dr. Van Son Nguyen, Guillaume Marcaud, Etienne Thiebaut, Loïc Guillemot and Amina Aidoud.

Very special thanks belong to my family and my friends for their everlasting support during my studies. They made it possible.

There are no words that could possibly express my gratitude enough, Zuzanka, my dear soulmate. "This morning I, too, pruned my rose trees..."

Contents

Introduction

The present thesis is devoted to systematic study of physical properties of two magnetic oxides, which both offer a broad range of important applications in oxide electronics.

Hole doped manganites $La_{1-x}M_xMnO_3$, where M stands for either Ca, Sr or Ba, are well known materials thanks to their unique combination of physical properties. The colossal magnetoresistance (CMR) [1] together with high degree of spin polarization is common for the whole family of hole doped manganites. The extensive research dedicated to the particular case of $La_{2/3}Sr_{1/3}MnO_3$ (LSMO) has been initiated by its high Curie temperature ($T_{C,bulk} \sim 370$ K) [2] and almost 100 % spin polarization [3]. Such combination of physical properties makes LSMO an interesting candidate for various applications in the field of spintronics.

The ferromagnetic ordering of LSMO originates in the presence of mixed valence manganese ions Mn^{3+} and Mn^{4+}. It has been theoretically explained by C. Zener [4] with a mechanism called double-exchange (DE) interaction. It arises from e_g electron transfer between Mn^{3+} and Mn^{4+} ions via O^{2-} $2p$ state. The probability of DE electron transitions strongly depends on Mn^{3+}-O-Mn^{4+} geometry, i.e. on Mn-O bong length and Mn-O-Mn bond angle. As a result the main factors responsible for changes in magnetic properties of LSMO are rotations and distortions of MnO_6 octahedra, which are induced in the films either by epitaxial strain coming from lattice mismatched substrate or by coupling of octahedral rotations at the LSMO/substrate interface [5].

While the interfacial nature of oxygen octahedra coupling (OOC) restricts this effect to a distance of several monolayers, thin films of LSMO deposited on mismatched substrate remains fully strained up to thicknesses of several tens of nanometers. This makes the factor of strain even more important with respect to magnetic properties, considering that the first few monolayers, which are most likely to be influenced by OOC, are at the same time typically magnetically inert.

To a thin LSMO layer, strain can be transfered either in a static or a dynamic way. While static approach by use of different lattice mismatched substrates provides a great background for basic research, the ability to tune the strain dynamically is essential for following applications.

The presented work was motivated by dynamic control of domain wall motion in a spin-valve structure, realized by use of underlaying piezoelectric layer [6]. As schematically shown in Fig. 1, magnetization reversal process was controlled by external voltage application on the piezoelectric underlayer, as the voltage induced strain created potential for domain wall pinning in the spin-valve nanowire.

In this work we try to elucidate the impact of epitaxial strain on magnetic and magneto-optical properties of LSMO ultrathin films. We investigated LSMO grown on four different substrate materials, which induce a variaty of strains, ranging from large compressive strain on $LaAlO_3$ (LAO), through small compressive strain on $(LaAlO_3)_{1/3}(Sr_2AlTaO_6)_{2/3}$ (LSAT) and small tensile strain on $SrTiO_3$ (STO), up to large tensile strain on $DyScO_3$ (DSO). Subsequently we try to achieve dynamical control of magnetization in patterned LSMO by use of piezoelectric underlayer.

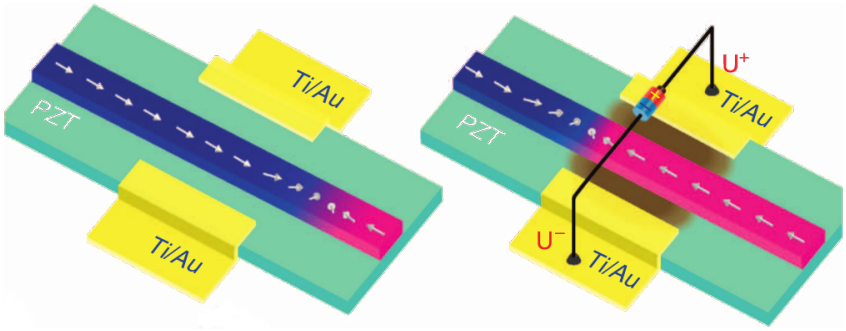

Figure 1: Schematic representation of magnetization reversal process in spin valve nanowire, dynamically controlled by strain via use of external voltage on piezoelectric underlayer (taken from [6]).

$SrRuO_3$ (SRO) is another well known ferromagnetic oxide ($T_{C,bulk} \sim 160$ K [7]), which offers a broad range of applications in oxide electronics. The combination of good conducting properties and nearly ideal epitaxial growth has made it the most popular material for electrodes fabrication in oxide heterostructures [8]. Furthermore, multilayer systems of SRO and other oxides as STO [9] or LSMO [10, 11] exhibit suitable properties for fabrication of all-oxide magnetic tunnel junctions.

Despite several decades of investigation, the exact nature of magnetic anisotropy of SRO still remains a subject of scientific debate in both bulk SRO [8] as well as in thin films [12]. However the importance of this knowledge is stressed on as attempts of dynamical magnetization switching in SRO films are emerging. After current induced domain wall nucleation [13] and domain wall motion [14] has been introduced, temperature induced [15] as well as current induced [16, 17] magnetization reversal in SRO films has been demonstrated. Even dynamical control of magnetization by use of piezoelectric underlayer was reported by Zhou *et al.* [18], yet magnetization reversal was not achieved this way. For proper functioning of potential spintronic devices using the magnetization reversal process in SRO, not only a precise description of magnetic anisotropy, but detailed knowledge of dynamic behaviour of magnetic domains is essential, especially when aiming at devices of fast operation.

Growth of SRO on the most commonly used substrate of STO is possible in six different crystallographic orientations, so called variants [19, 20]. Multi-variant growth can be suppressed by proper choice of substrate miscut angle, yielding single-variant SRO films of higher overall quality.

In this work we report on time evolution of magnetic domains in multi-variant and almost single-variant SRO thin films. By means of magnetic and magneto-optical methods we investigate the magnetization dynamics and magnetic domain formation in both single and multi-variant SRO thin films. We observe significant differences in the magnetic domain wall motion behaviour. We argue that those differences are related to defects emerging in the polycrystalline films as a result of the multi-variant growth.

Thesis outline

Structure of the work is organised as follows. The first chapter provides readers with general introduction to the structural and magnetic properties of the two investigated magnetic oxides - LSMO and SRO. We highlight the important structural element of oxygen octahedra, and we describe the significant changes of physical properties of the materials when going from the bulk form to ultrathin layers. These changes manifest essential influence of the epitaxial strain, which is one of the main topics of this work. The end of this introductory chapter deals briefly with the influence of Barkhausen effect on magnetization dynamics, i.e. on time evolution of domain wall motion mechanism, which is the second major topic of the work.

The second chapter provides necessary theoretical background to the key techniques used in this study. A combination of spectroscopic ellipsometry and magneto-optical spectroscopy is a powerful tool for investigation of ultrathin layers. It allows us to determine spectral dependence of the full tensor of permittivity, thus providing valuable information not only about material properties of the sample, but also about its electronic structure. In the second chapter we provide the theoretical aparatus for treating the optical, and especially the magneto-optical phenomena, including procedures for extraction of the elements of permittivity tensor from experimental data.

The third chapter gives a brief overview of the most important experimental techniques used in this work. Functioning of the optical and magneto-optical characterization methods is explained in detail with the use of the theoretical aparatus developed in the second chapter.

The fourth chapter presents all the individual samples investigated in this work. It includes LSMO single layers on various substrates, where the effect of static epitaxial strain is studied. Then a heterostructure with LSMO on piezoelectric underlayer, which serves for dynamic application of the strain. The last material system consists of SRO single layers, in which the effect of substrate miscut angle is investigated.

The fifth and the sixth chapter summarize the achieved results. First part of the fifth chapter deals with the static application of strain to LSMO by use of various substrates, the second part deals with the dynamic application of strain via piezoelectric underlayer. Finally the sixth chapter presents the influence of substrate miscut on magnetization dynamics of SRO.

1. Structural and magnetic properties of oxide ultrathin layers

The first introductory chapter presents the principal topics of this work more in detail. We familiarise the reader with the two investigated oxide materials. We describe their basic structural and magnetic properties, starting from their bulk form, and explaining the changes underwent during transition into the ultrathin layers.

These changes originate in the deposition process, where the growing layer adjusts its properties depending on the substrate. Such changes may pertain across the whole thickness of the deposited layer, as for example composition of variants induced by substrate miscut angle, or they may only be present in close proximity of the layer/substrate interface, as for example strain induced changes of the orbital ordering, which are relaxing with the thickness of the film as the epitaxial strain is relaxing away from the interface.

We focus on the role of epitaxial strain, which is one of the key elements in influencing structural and magnetic properties of ultrathin perovskite oxides. We pay a special attention to the so called oxygen octahedra rotations. The oxygen octahedra are an essential building element of the oxide materials, and their strain induced rotations may have consequences that reach far beyond mere changes in the crystallographic structure.

The last section of this chapter stands aside, covering another topic - magnetization dynamics. The magnetization reversal process is described on the theoretical basis of pinning centers, as presented by H. Barkhausen, which provides necessary understanding of the magnetization dynamics phenomena that will be studied later on in this thesis.

1.1 Bulk $La_{2/3}Sr_{1/3}MnO_3$ and $SrRuO_3$

An ideal crystallographic structure of manganese oxides is cubic perovskite - ABO_3, such as shown in Fig. 1.1. A-site cation is located in the unit cell corner, while B-site cation is in the center of the unit cell. Oxygen atoms are located in between the B atoms, in the middle of their distance. In such a way the B atoms are surrounded by six oxygen atoms, creating a BO_6 octahedron. This structure belongs to $Pm\bar{3}m$ space group (No. 221).

The structure of manganese oxides obeys the so called tolerance factor [22]

$$t = \frac{r_A + r_O}{\sqrt{2(r_B + r_O)}}, \tag{1.1}$$

where r_A, r_B and r_O are ionic radii of the A and B atoms and oxygen, respectively. For the ideal cubic perovskite $t = 1$, while the structure remains stable for $0.89 < t < 1.02$ [21]. Typically, t significantly differs from unity as a result of variations in cation ionic radii, which leads to a distorted rhombohedral

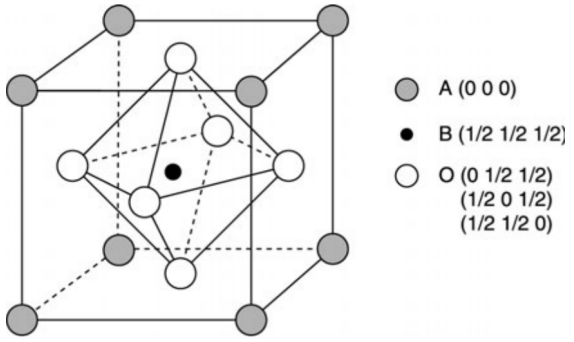

Figure 1.1: Schematic view of ideal cubic perovskite structure ABO_3 (taken from [21]). Six oxygen atoms around the B-site cation create BO_6 octahedron.

or orthorhombic structure. The orthorhombic crystal structure of LSMO parent compound $LaMnO_3$ is shown in Fig. 1.2(a).

Unit cell of bulk $La_{2/3}Sr_{1/3}MnO_3$ can be described as rhombohedral with lattice constants $a_r = 5.471$ Å and $\alpha_r = 60.43°$ [23]. This structure belongs to $R\bar{3}c$ space group (No. 167).

Magnetic properties of manganites are driven by manganese ion spins and their mutual exchange interactions, which are given by the overlap of manganese d-orbitals and oxygen p-orbitals. The superexchange interaction leads to antiferromagnetic behaviour in case of Mn^{4+}-O-Mn^{4+}, while for Mn^{3+}-O-Mn^{3+} it can be both ferromagnetic and antiferromagnetic [26]. In LSMO, the presence of mixed valence manganese ions Mn^{3+}/Mn^{4+} leads to ferromagnetic ordering, which was explained by C. Zener [4] by a different mechanism, so called double exchange (DE) interaction. It originates in e_g electron transfer between Mn^{3+} and Mn^{4+} ions via O^{2-} $2p$ state, as schematically depicted in Fig. 1.3(a).

In bulk LSMO, the easy axis of magnetization lies in the pseudocubic [111] direction [27, 28]. Concerning the Curie temperature, Jonker and van Santen [2] grew $La_{1-x}Sr_xMnO_3$ oxides of various values of Sr doping. They found that for

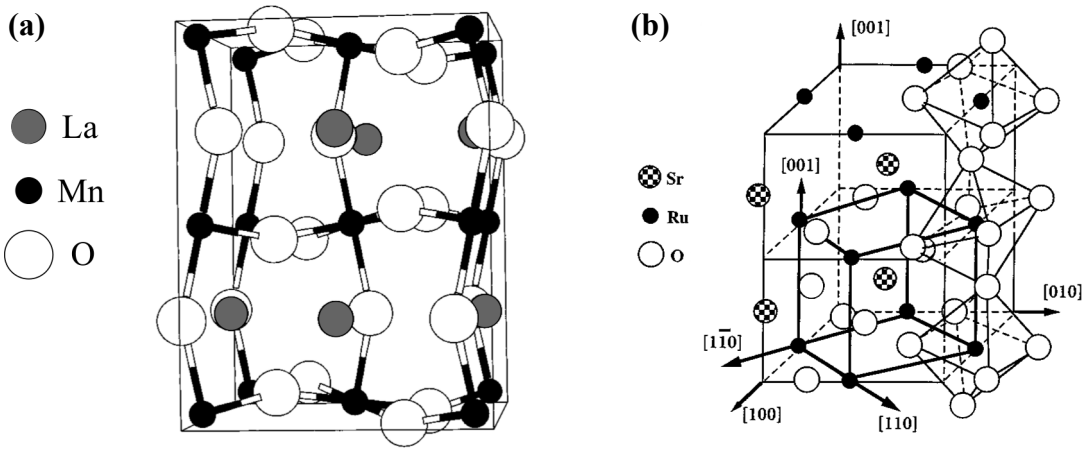

Figure 1.2: Schematic view of orthorhombic structure of: (a) LSMO parent compound $LaMnO_3$ (taken from [24]), (b) $SrRuO_3$, the highlighted cube represents pseudocubic unit cell (taken from [25]).

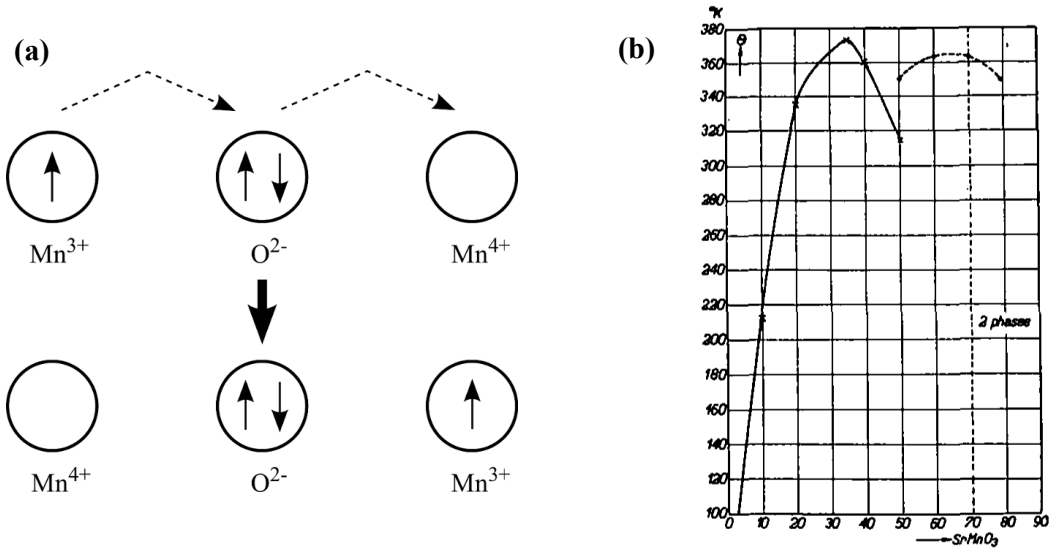

Figure 1.3: (a) Schematic diagram of double exchange interaction. (b) Dependence of Curie temperature of $La_{1-x}Sr_xMnO_3$ on Sr doping (taken from [2]).

$x = 1/3$ the $La_{2/3}Sr_{1/3}MnO_3$ has the highest Curie temperature $T_C \sim 370$ K, see Fig. 1.3(b).

$SrRuO_3$ is a member of the Ruddlesden-Popper [29] series of Sr ruthenates $Sr_{n+1}Ru_nO_{3n+1}$, with $n = \infty$. Unit cell of SRO is of the $GdFeO_3$ type. At room temperature, it can be described as orthorhombic with lattice constants $a_o = 5.567$ Å, $b_o = 5.530$ Å and $c_o = 7.845$ Å [30]. This structure belongs to Pbnm space group (No. 62). It is schematically depicted in Fig. 1.2(b).

Transport and magnetic properties of the Ruddlesden-Popper series members differ significantly as a function of n. For example, for $n = 1$ we get Sr_2RuO_4, which is the first known perovskite superconductor without copper [31]. The infinity case ($n = \infty$) of SRO is an itinerant ferromagnet with $T_C \sim 160$ K [7]. Magnetocrystalline anisotropy of bulk SRO remains an unresolved issue, as different directions of the easy axis of magnetization (in $(001)_o$ plane and $\langle 110 \rangle_c$ directions) as well as different anisotropy field values were reported [8].

1.2 Oxygen octahedra rotations and Glazer notation system

In previous section we have introduced an important structural element of perovskite materials - the BO_6 octahedron (see Fig. 1.1). If we imagine the B-site cation as an origin of Cartesian coordinate system, in which the oxygen atoms lie on its principal axes, we say that the BO_6 octahedron is not tilted, which is the case of ideal cubic perovskite structure. If the octahedra are departed from this ideal position while remaining rigid, i.e. with no distortion, we say they underwent oxygen octahedra rotations (OOR).

An example of such OOR can be seen in Fig. 1.2(b), where the orthorhombic SRO structure is introduced. Several RuO_6 octahedra are highlighted and their mutual tilt is clearly visible.

The OOR patterns can have significant impact on resulting physical properties of magnetic oxides. In order to classify the OOR patterns, Glazer introduced a notation system [33], which was later extended by Woodward [34, 35]. In this system, the OOR are expressed as a combination of three independent rotations around three Cartesian coordinate axes, which are given by the three pseudocubic axes $[100]_c$, $[010]_c$ and $[001]_c$. Relative magnitudes of the rotations are denoted by letters a, b and c for each of the pseudocubic directions. Rotations of two adjacent octahedra can be either in phase or out of phase, which is denoted by $+$ or $-$ sign in the superscript. When 0 occurs in the superscript, there is no rotation around the respective axis.

Few of the simplest examples are shown in Fig. 1.4. The cubic structure, which possesses no OOR, is denoted as $a^0a^0a^0$. This means that relative magnitudes of rotations around all three pseudocubic axes are equal, which is obvious as they are all absent. The Glazer notation for tetragonal structure is $a^0a^0c^+$. We can see that rotations around $[100]_c$ and $[010]_c$ axes are still absent, but rotations around the $[001]_c$ axis, which points out from the picture, take place. The $+$ sign indicates in phase rotations of adjacent octahedra, which means that the octahedra rotate in the same direction, keeping the oxygen atoms aligned along the rotational $[001]_c$ axis. Note that the last letter c is different from the first two, indicating different rotation magnitude. The example of rhombohedral structure is denoted by $a^-a^-a^-$. This means that rotations around all three axes are present, same in magnitude and all out of phase. The out of phase rotations represent two adjacent octahedra rotating in opposite direction, so that the oxygen atoms are no longer aligned along the rotational axis. In all the cases we can see that the oxygen octahedra retain corner connectivity, which is a simple geometric constraint forcing two adjacent octahedra to maintain a common oxygen atom. When thin layer of oxide material is being deposited on a substrate, one of the possible ways to accommodate the imposed epitaxial strain is via OOR, which help to maintain the corner connectivity accross the interface.

As shown by Glazer [33], there are 23 possible tilt systems. The rhombohedral

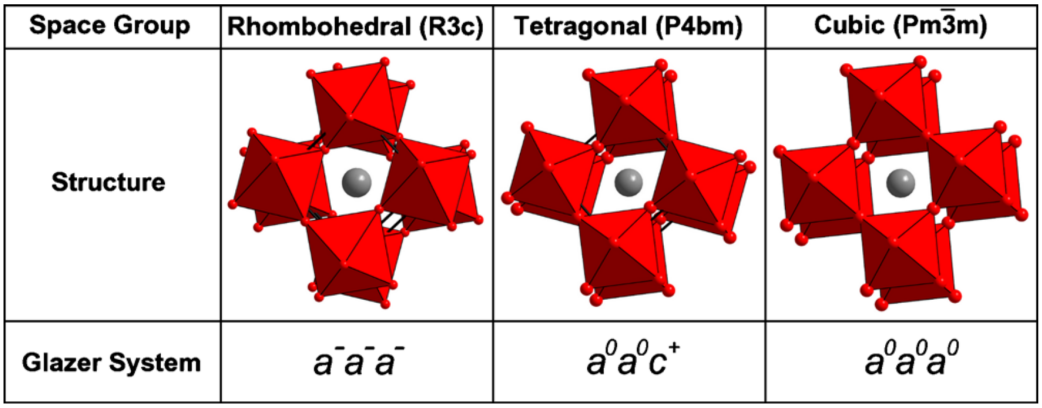

Figure 1.4: Schematic diagram of BO_6 octahedra rotation patterns in cubic, tetragonal and rhombohedral perovskite structure (taken from [32]). The Glazer notation is given assuming [001] pseudocubic axis pointing out of the image plane, [100] and [010] pseudocubic axes lie in the image plane and are aligned along the horizontal and vertical direction.

structure of bulk LSMO is sorted as system #14, noted as $a^-a^-a^-$. Such a system we introduced in Fig. 1.4. The orthorhombic structure of bulk SRO belongs to system #10: $a^+b^-b^-$. Here the two rotations around $[010]_c$ and $[001]_c$ axes are both out of phase and of the same magnitude, while the rotation around $[100]_c$ axis is in phase and of a different magnitude than the latter two.

1.3 Strain modifications of crystallographic structure

Initial crystallographic structure of a bulk material is modified when we grow such material as a thin layer. The difference between lattice parameters of substrate and deposited layer is quantified by lattice mismatch

$$m = \frac{a_l - a_s}{a_s}, \tag{1.2}$$

where a_l and a_s are initial bulk values of in-plane lattice constants of the layer and substrate material. The lattice mismatch induces epitaxial strain in the layer. For $a_l > a_s$, i.e. positive value of m, the layer is grown under compressive strain. The opposite case of negative m is called tensile strain.

Growth of magnetic oxide layers is typically realized on cubic oxide substrates such as $SrTiO_3$ or $LaAlO_3$. The strained layer deposited on (001) oriented cubic substrate can be usually described as monoclinic with (110) orientation, but it is often treated as pseudocubic. In our case, for description of LSMO and SRO unit cells, both these approaches can be used. Relations between the main cubic (pseudocubic) and monoclinic crystallographic directions of a substrate and deposited layer are shown in Fig. 1.5.

The monoclinic unit cell is characterized by lattice parameters a_m, b_m, c_m, α_m, β_m and γ_m, where $\alpha_m = \beta_m = 90°$. They are related to the pseudocubic lattice

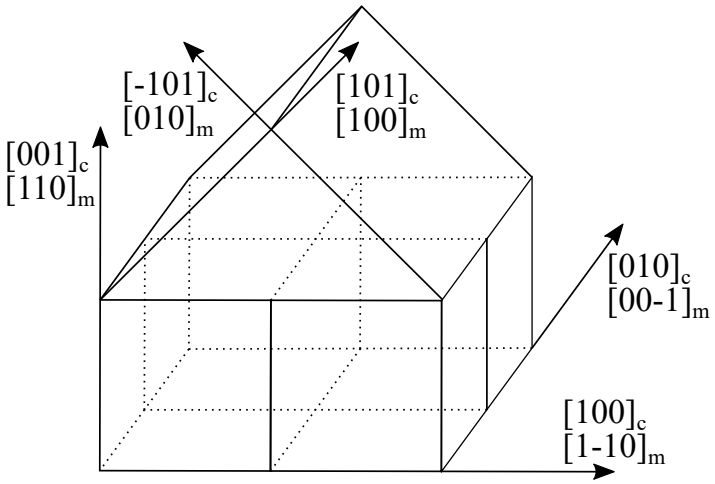

Figure 1.5: Relations between the main cubic (pseudocubic) and monoclinic crystallographic directions in a (001) oriented cubic substrate and (110) oriented monoclinic (pseudocubic) growing layer.

parameters a_c, b_c, c_c and α_c via

$$a_c = \frac{\sqrt{a_m^2 + b_m^2 - 2a_m b_m \cos\gamma_m}}{2}, \tag{1.3}$$

$$b_c = \frac{c_m}{2} \approx \frac{a_m}{\sqrt{2}} \approx \frac{b_m}{\sqrt{2}}, \tag{1.4}$$

$$c_c = \sqrt{\frac{a_m^2 + b_m^2 - 2a_c^2}{2}}, \tag{1.5}$$

$$\alpha_c = \arccos\left(\frac{a_c^2 + c_c^2 - a_m^2}{2a_c c_c}\right). \tag{1.6}$$

Typical distortion of pseudocubic and monoclinic crystallographic structure under compressive and tensile strain is shown in Fig. 1.6. It has been found that compressively stressed LSMO [36, 23] and SRO [23] accommodate the strain differently along different crystallographic in-plane axes. Periodic lattice modulations were observed along the $[001]_m$ direction, while lattice distortions occur in the $[1\text{-}10]_m$ direction. We can imagine the lattice modulations as relative displacements of the unit cells in $[110]_m$ direction [23]. They have certain amplitude and they are periodic in the $[001]_m$ direction. Different stress relief mechanism was observed along the $[1\text{-}10]_m$ direction. The unit cell becomes distorted, accommodating the strain by reduction of the γ_m angle, as shown in Fig. 1.6(b). In the monoclinic unit cell $a_m < b_m$ and $\gamma_m < 90°$, in the pseudocubic description $a_c < c_c$ and $\alpha_c < 90°$. The tensile strain in LSMO and SRO was studied as well [23]. Similar mechanism leading to distortion of the unit cell was observed as shown in Fig. 1.6(c). In this case the unit cell becomes tetragonal with $a_m = b_m$ and $\gamma_m > 90°$, in the pseudocubic description $a_c > c_c$ and $\alpha_c = 90°$. Such behaviour of lattice distortions was observed in coherently strained LSMO and SRO thin films, but it is assumed to be of general character among perovskite oxides [23].

Imposing strain, either compressive or tensile, on perovskite crystal structure results in its distortion, as we have just described and as we can see in Fig. 1.6. Such distortion obviously leads to changes in crystal symmetry and related alternations of the OOR pattern. It has been shown [23] that despite exhibiting

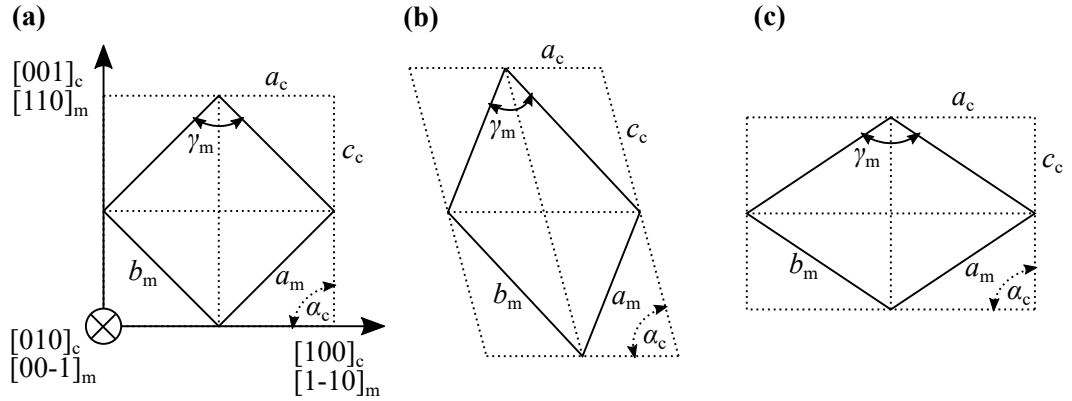

Figure 1.6: Schematic projection of monoclinic and pseudocubic unit cell, when it is (a) not distorted, (b) distorted under compressive strain, (c) distorted under tensile strain; a_m, b_m and γ_m are monoclinic lattice parameters, a_c, c_c and α_c are pseudocubic lattice parameters.

different OOR patterns in their bulk form, both LSMO and SRO possess the same Glazer tilt system #9: $a^+a^-c^-$, when grown on a cubic substrate under compressive strain. The OOR pattern slightly changes if the substrate is not perfectly cubic, i.e. $a_c \neq b_c$, but it still remains the same for both LSMO and SRO. The presence and phase of the rotations is preserved, but all three rotations now have different magnitudes. It is the tilt system #8: $a^+b^-c^-$. However, both these tilt systems are very similar and they both correspond to $P2_1/m$ space group (No. 11). In the case of tensile strain, elongation of the pseudocubic in-plane lattice parameters results in suppression of OOR around the out-of-plane axis. Rotations around the latter two axes are maintained. The situation is again the same for both LSMO and SRO, it is tilt system #18: $a^+a^-c^0$, which corresponds to Cmcm space group (No. 63).

1.4 Strain influence on physical properties of magnetic oxides

In previous section we described changes arising in crystal structure of perovskite oxides when being deposited as thin films on susbstrates, which impose epitaxial strain. Such changes, which are related to modifications of OOR pattern and crystal symmetry, may be expected to lead to changes in other physical properties of the materials. Distortion of the perfectly cubic perovskite unit cell leads to symmetry lowering, which lifts the degeneracy of d energy levels. Such changes in electron structure then inevitably result in modifications of transport and magnetic properties of perovskite oxides.

1.4.1 Orbital ordering

Schematic diagram of manganese $3d$ energy levels is shown in Fig. 1.7. In a spherical field of isolated Mn atom, all five energy levels are degenerated. In a crystal field of perfect cubic symmetry, the levels split into 2 e_g and 3 t_{2g} levels. The degeneracy is further lifted as the symmetry of the cubic field is lowered. Compressive or tensile strain leads to distortion of MnO_6 octahedra, which leads to stabilization of the out-of-plane or in-plane e_g and t_{2g} orbitals.

Fig. 1.7 also shows, that the MnO_6 distortion is strongly supported by Mn^{3+}, while Mn^{4+} prefers to keep its energy unchanged. This is known as Jahn-Teller effect. Even if the content of Mn^{4+} is increased, the remaining e_g electrons of Mn^{3+} do not occupy the e_g orbitals at random and an orbital order is achieved [21]. Stabilization of the e_g orbitals, as it is shown in Fig. 1.7, was confirmed by several independent studies. Aruta *et al.* showed by means of linear dichroism (LD) in X-ray absorption spectroscopy (XAS), that LSMO films grown under compressive strain on LAO substrates stabilize the out-of-plane $(3z^2 - r^2)$ e_g orbitals [37], while preferential in-plane $(x^2 - y^2)$ orbital ordering is achieved in LSMO films grown under tensile strain on STO substrates [37, 38]. Tebano *et al.* [39] also demonstrated by LD-XAS preferential $(3z^2 - r^2)$ ordering for LSMO grown under compressive strain on LAO and $NdGaO_3$ (NGO) substrates. Their further results of tensilely strained LSMO on STO revealed $(x^2 - y^2)$ orbital ordering in agreement with Aruta *et al.*, but below a critical thickness of approx-

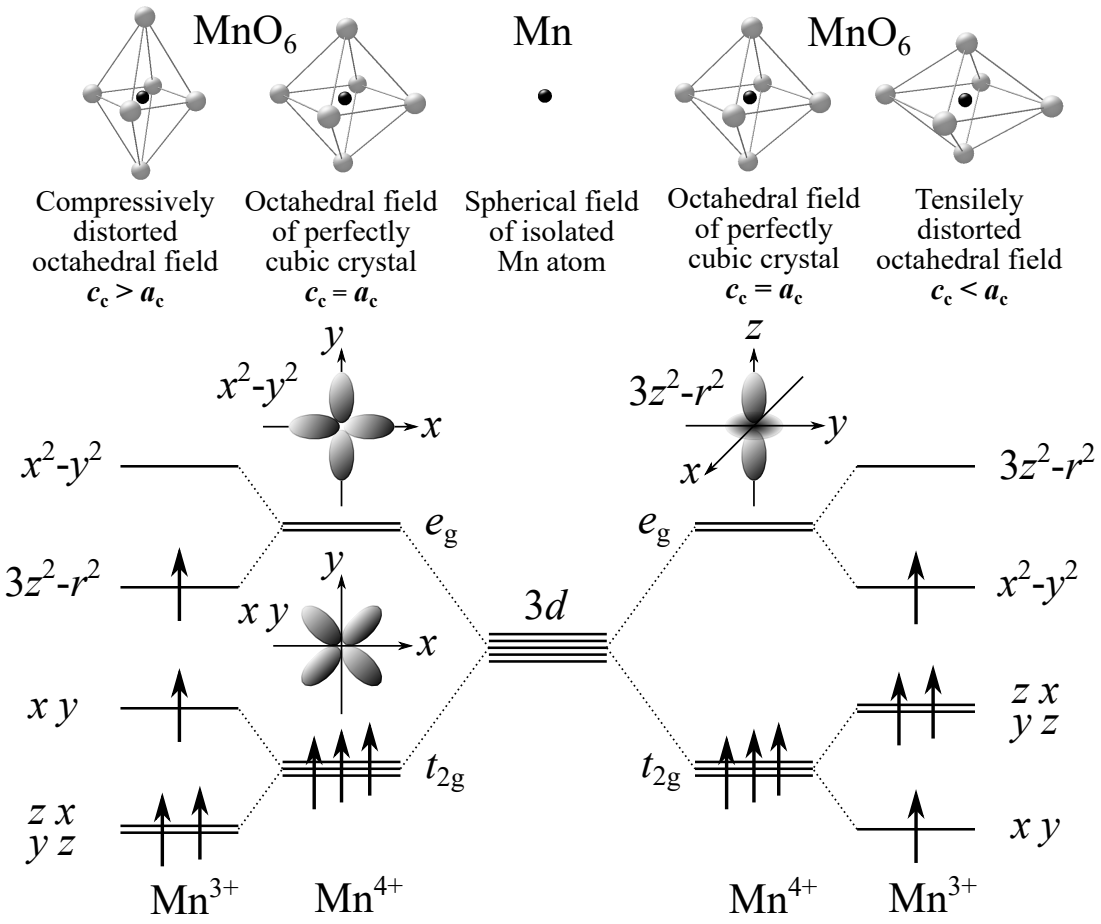

Figure 1.7: Schematic diagram of Mn $3d$ energy levels. Their degeneracy is partially lifted in cubic crystal field, where they split into 2 e_g and 3 t_{2g} levels. Further stabilization of out-of-plane and in-plane orbitals is achieved in a crystal field of lower symmetry, resulting from epitaxial strain. Occupation of the energy levels shows that the octahedra distortion is supported by Mn^{3+} presence via Jahn-Teller effect.

imately 6 unit cells, orbital reconstruction was observed, favouring in contrast the $(3z^2 - r^2)$ orbitals. They explain these results as a consequence of symmetry breaking at the interface. They further confirm these findings by means of angle-resolved photoemission spectroscopy [40]. In contradiction, Huijben *et al.* [41] reported on $(3z^2 - r^2)$ orbitals stabilization in tensilely strained LSMO on STO up to film thicknesses of 70 unit cells. However, Pesquera *et al.* [42, 43] also reported studies of LSMO grown on various substrate materials providing both compressive and tensile strain. Their XAS results are in agreement with previous findings of the groups of Aruta and Tebano.

The strain dependent orbital ordering has further consequences on resulting magnetic properties of LSMO. Fig. 1.8(a) shows phase diagram of $La_{1-x}Sr_xMnO_3$ in the plane of epitaxial strain represented by pseudocubic c/a ratio and doping level x. Figs. 1.8(b)-(d) explain the relations between strain induced orbital ordering and related ferromagnetic or antiferromagnetic (AF) order. It has been reported [44] that the preferential $(3z^2 - r^2)$ orbital ordering favours chain-type (C-type) AF ordering, while stabilization of $(x^2 - y^2)$ orbitals leads to layer-type (A-

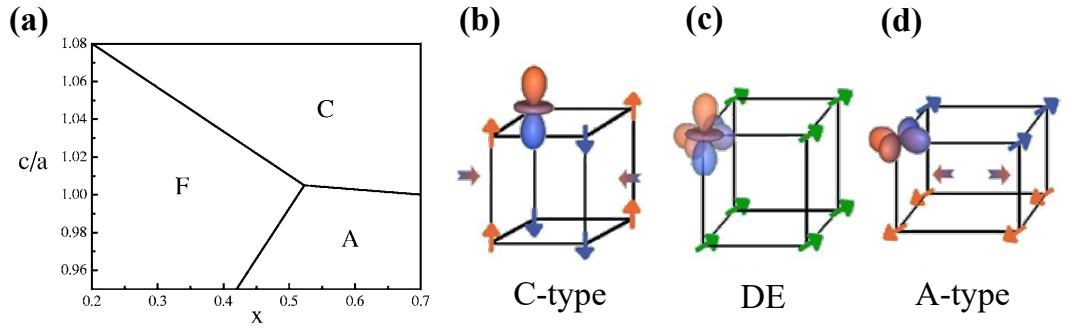

Figure 1.8: (a) Phase diagram of $La_{1-x}Sr_xMnO_3$ in the plane of epitaxial strain and Sr doping level x (taken from [47]). Strain is represented by pseudocubic c/a ratio. The letters A, F and C denote A-type antiferromagnetic ordering, ferromagnetic ordering and C-type antiferromagnetic ordering, respectively. (b)-(d) Schematic representation of strain induced changes in magnetic ordering (taken from [39]); (b) C-type antiferromagnetic ordering, (c) ferromagnetic ordering with enabled double-exchange, (d) A-type antiferromagnetic ordering.

type) AF order. The ferromagnetic double-exchange mechanism is most strongly manifested in undistorted structure with strongly degenerated e_g levels. The strain induced suppression of DE mechanism has been revealed as the most plausible explanation for the so called magnetically inert layer at the LSMO/substrate interfaces of epitaxially strained LSMO thin films [39, 40, 45, 46].

1.4.2 Magnetic anisotropy

Magnetic anisotropy of LSMO exhibits strong dependence on epitaxial strain. Easy axis of magnetization, which for bulk LSMO lies along the pseudocubic $[111]_c$ direction [27, 28], shifts typically into the sample plane of thin films[1]. LSMO grown under tensile strain on STO substrate shows in-plane magnetic anisotropy [48, 49, 50, 51, 21], which further depends on temperature. Above 250 K, the two in-plane directions $\langle 100\rangle_c$ and $\langle 110\rangle_c$ are equivalent easy axes of magnetization [48, 50, 51]. Below 250 K, the easy axis along $\langle 100\rangle_c$ direction remains, but the easy axis behaviour is more pronounced in the $\langle 110\rangle_c$ directions [50, 21]. Such behaviour corresponds to prevailing contribution to magnetic anisotropy coming from the substrate symmetry, while additional contribution is introduced along the direction of epitaxial strain. This can even lead to perpendicular magnetic anisotropy, which was reported below 200 K on LSMO films grown under compressive strain on LAO substrates [49, 50]. LSMO films grown under small compressive strain on LSAT and NGO exhibit temperature dependent combination of uniaxial anisotropy along $\langle 100\rangle_c$ direction and biaxial anisotropy along $\langle 110\rangle_c$ directions [50]. The easy axis always remains in-plane as compressive strain is here not strong enough to induce perpendicular magnetic anisotropy.

Magnetic anisotropy of SRO is also influenced by epitaxial strain. Easy axis of magnetization, which is not clearly understood in bulk SRO [8], being reported in both $(001)_o$ plane and $\langle 110\rangle_c$ directions, turns into $[010]_m$ direction in SRO thin films grown under tensile strain on the most common substrate of STO [52,

[1]See Fig. 1.5 for definition of basic crystallographic directions.

53]. However, it exhibits peculiar temperature dependence. Below T_C, the easy axis of magnetization, while remaining in the $(001)_m$ plane, it rotates from the surface normal from $\sim 45°$, i.e. the $[010]_m$ direction, to $\sim 30°$ with decreasing temperature [54].

1.4.3 Interplay of OOR and epitaxial strain

In section 1.3 we have described the strain modifications of crystallographic structure and related changes in OOR patterns. The OOR can be induced not only by epitaxial strain, but by the substrate symmetry as well. Moreover the oxygen octahedra can not only be rotated, but distorted as well, as we have shown sooner in this section. Interplay of epitaxial strain, substrate symmetry, oxygen octahedra rotations and distortions is a complex topic undergoing extensive research, which reveals significant impact of oxygen octahedra related phenomena on physical properties of magnetic oxides.

Fundamental research in this domain investigates origin and possible control of OOR and its relation to epitaxial strain and crystallographic structure of the substrates [23, 55, 56]. More complex studies are trying to explain the exact impact of OOR on resulting magnetic and transport properties and to suggest possibilities of direct tuning of the physical properties by OOR engineering [57, 58, 59, 60].

The first group of research is focused on the basic structural properties. As we have already shown in section 1.3, the group of Vailionis *et al.* [23] revealed different OOR pattern in LSMO films grown under compressive and tensile strain. They further report on OOR evolution accross the LSMO/STO interface in thin LSMO films [55]. Moon *et al.* [61] try to isolate the effect of epitaxial strain from OOR by growing LSMO on two substrates of similar lattice constants and different crystal symmetries. They find that the transport and magnetic properties differ significantly when grown on cubic LSAT or orthorhombic NGO, which both impose small compressive strain on LSMO, but both induce different OOR pattern. By means of scanning transmission electron microscopy, Liao *et al.* [60] confirm presence of OOR at the LSMO/NGO interface. They further observe that OOR can be supressed using STO buffer layer in between the NGO substrate and LSMO layer on top. The suppression of OOR is observable after use of even one monolayer of the STO. Similar behaviour was observed in LSMO single layers grown on STO substrates [57] and even in LSMO/STO superlattices [59]. The OOR in LSMO are suppressed at the LSMO/STO interface, but they evolve slowly to their bulk value with the distance from the interface in both LSMO single layers and superlattices.

Concerning the influence of OOR on other physical properties, the presence of OOR in LSMO thin films is mostly argued to significantly affect the transport and magnetic properties [57, 59]. However, the exact nature of these phenomena has not yet been satisfactorily explained, as some reports, for example, reveal deterioration of magnetic properties with increasing octahedral tilt [57], and other reports, on the contrary, demonstrate deterioration of magnetism with decreasing octahedra tilt angle [59]. Liao *et al.* [60] try to be even more specific, describing a precise impact of OOR on magnetic anisotropy.

In general, the behaviour and influence of OOR in LSMO is in agreement with

results observed in SRO. Vailionis *et al.* [23] reports the same OOR pattern for LSMO and SRO under compressive and tensile strain. Theoretical study of He *et al.* [56] reports on OOR in both LSMO and SRO. They conclude that OOR in SRO are suppressed near the SRO/substrate interface and with distance from the interface evolve towards their bulk value. Thomas *et al.* [62] study SRO layers grown on DSO substrate and covered with an STO capping layer. The use of STO capping layer suppresses OOR in the SRO layer, leading to an enhancement of its magnetic properties. Tuning of the magnetic anisotropy of SRO by use of a buffer layer was achieved by group of Kan *et al.* [58].

In contrast to the research presenting importance of OOR on resulting physical properties stands the study of Souza-Neto *et al.* [63], reporting an X-ray absorption spectroscopy study of LSMO films on STO and LAO substrates. They emphasize the importance of MnO_6 octahedra distortion rather than the OOR. Thus we can see that altough the impact of OOR and oxygen octahedra distortions is unequivocal, the exact nature of these phenomena and their relation to the epitaxial strain and substrate symmetry remains an open question.

1.5 Magnetization dynamics and Barkhausen effect

A ferromagnetic material can react on external magnetic field in two possible ways. One of them is coherent rotation, i.e. rotation of magnetization direction of magnetic domains or even of the whole sample. Another way uses domain wall (DW) motion to change the sample magnetization. As coherent rotation requires movement of magnetization away from easy axis in large volume of the sample, it is typically energeticaly less favourable.

The DW motion process consists of two mechanisms. First it is the domain nucleation, i.e. creation of new magnetic domains, and second the actual DW motion or DW propagation. It has been already observed by H. Barkhausen [64] in 1919, when he detected the so called Barkhausen noise, that this process is not continuous, which is caused by its energy requirements. Formation of domains demands activation energy, which is needed to overcome a critical domain size. DW motion costs in principle no energy, because the DW energy required at given position is released at its previous location. However, no crystal material is perfect and presence of crystallographic defects is inevitable. These defects act as pinning centers for the DWs and to release DWs from such pinning centers, activation energy is needed as well. Fig. 1.9(a) shows schematic visualization of the magnetization reversal process in a sample, where the black dots visible on sample surface represent the crystallographic defects acting as pinning centers for DWs. Release of DW from such pinning center is accompanied by so called Barkhausen jump, which is a step-like increment of overall sample magnetization. Fig. 1.9(b) shows part of a magnetization hysteresis loop, where the Barkhausen jumps are highlighted in the zoomed inset of the figure. Visualisation of the magnetization reversal process can be realized not only by measurements of Barkhausen noise, but also by direct techniques. Especially when the dynamics is slow enough, magnetic domains can be observed, e.g. by Kerr microscopy [65] or magnetic force microscopy [66].

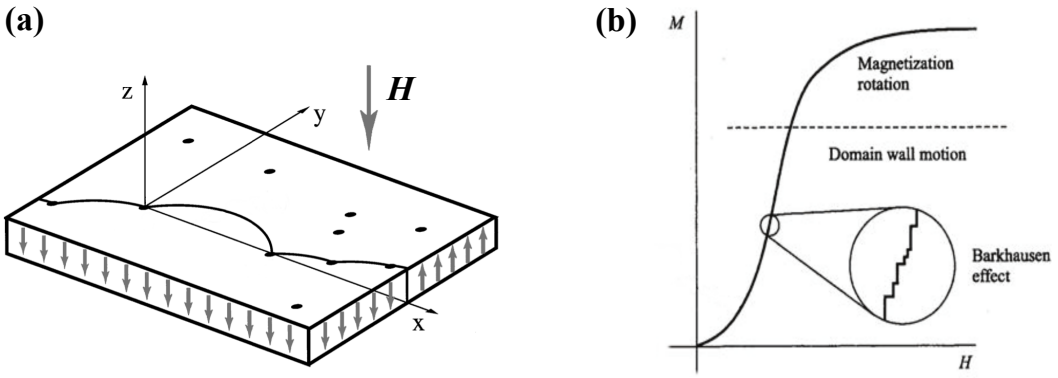

Figure 1.9: (a) Schematic visualization of magnetization reversal process (taken from [67]). Black dots on sample surface act as pinning centers for DW motion. (b) Part of a magnetization hysteresis loop (taken from [68]). Zoomed inset shows individual Barkhausen jumps.

Exact knowledge of the magnetization reversal process in magnetic oxides gains importance with increased interest in magnetization switching of these materials. In SRO thin films, phenomena of current induced DW nucleation [13] and DW motion [14] have recently been demonstrated, as well as temperature induced [15] and current induced [16, 17] magnetization reversal and even periodic control of magnetization with use of piezoelectric substrate [18]. Investigating the magnetization dynamics, which as we have just seen is closely related to presence of crystallographic defects, may help us to better understand the related physical phenomena and to improve functioning of future device applications.

2. Basic theory of light polarization and magneto-optical effects

The second chapter provides theoretical introduction to optical, and especially magneto-optical phenomena, which are the essence of the key techniques used in this work - spectroscopic ellipsometry and magneto-optical spectroscopy.

In order to deal with the magneto-optical phenomena, first we need to develop tools to treat the light itself. Therefore at the beginning of this chapter we introduce polarized light, which is the starting element of any magneto-optical experiment. Next we present a simple mathematical way how to treat the light propagation through an arbitrary optical system, i.e. the Jones calculus. At this point we are ready to quantify the magneto-optical effects, i.e. define the magneto-optical angles.

The investigated material comes into play via its permittivity tensor, which is defined in the following section. Then we present a way how to obtain spectral dependence of the elements of the permittivity tensor in both the microscopic and the macroscopic approach. The microscopic theory provides us with essential understanding of the origin of magneto-optical phenomena, furthermore it gives us the mathematical description of the experimental spectra in terms of contributions from the individual electron transitions. The macroscopic theory of Yeh formalism gives us a strong mathematical apparatus for calculation of magneto-optical response in an arbitrary multilayer structure. It can be used either to calculate magneto-optical effects when we know material properties of the investigated system, or on the contrary, it can be used to determine unknown elements of the permittivity tensor from experimentally measured spectral dependence of the magneto-optical effects.

2.1 Light polarization and Jones calculus

Light is an electromagnetic wave, therefore we can describe some of its properties by simple description of the wave motion. Electric component is dominating in the interaction of light with matter, thus we use the vector of electric field strength to define the polarization of light. It is given by time evolution of the vector of electric field strength at a given point in space. If we assume the light as a time-harmonic plane wave consisting of three independent oscillations along the Cartesian axes, we can write it as

$$\boldsymbol{E} = E_x\boldsymbol{x} + E_y\boldsymbol{y} + E_z\boldsymbol{z}, \qquad E_i = A_{0i}\cos\left(\omega t + \delta_i\right), \qquad i = x, y, z, \tag{2.1}$$

where $\boldsymbol{x}, \boldsymbol{y}$ and $\boldsymbol{z}$ are unit vectors alongside the respective Cartesian axes, A_{0i} and δ_i are amplitudes and phase shifts of the individual components, and ω is the angular frequency. It can then be shown [69] that the electric field strength vector traces an ellipse. In other words, the most general case of light polarization is an elliptic polarization. Fig. 2.1 shows the ellipse of polarization in a plane

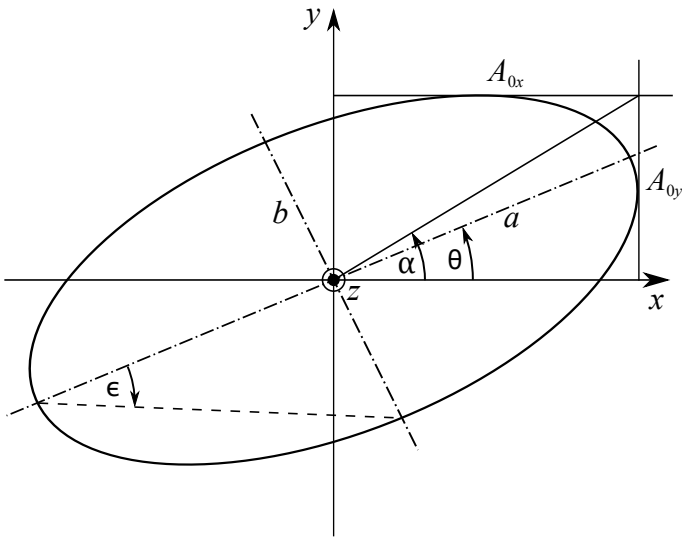

Figure 2.1: Ellipse of polarization when looking against the propagation direction of a light wave. The semi-major a and semi-minor axes b, amplitudes A_{0x} and A_{0y}, as well as the azimuth θ and ellipticity angle ϵ are shown.

perpendicular to the wave vector. It is an example of a wave travelling along the z axis when looking against the propagation direction. The ellipse is uniquely determined by four parameters, however for complete description of an arbitrary polarization state only two of them are necessary. They are

- the azimuth θ - an oriented angle between the major axis of the ellipse and positive x half-axis, it determines the orientation of the ellipse in its plane and it ranges from $-\pi/2$ to $\pi/2$, and
- the ellipticity e - a ratio of the lengths of the semi-minor and the semi-major axes, $e = b/a$. It ranges from -1 to 1. According to the sign of the ellipticity we assign a handedness to the polarization state. Positive sign corresponds to a right-handed polarization, while negative sign to a left-handed polarization. When looking against the propagation direction, what we actually see is a clockwise motion of the electric field vector in case of the right-handed polarization and anti-clockwise motion in case of the left-handed polarization. A quantity ϵ defined by $e = \tan\epsilon$ is called ellipticity angle and according to the ellipticity range it spreads from $-\pi/4$ to $\pi/4$.

The latter two quantities, which are not necessary for defining the polarization state, are the amplitude A and the absolute phase δ_0. The amplitude is given by the lengths of the axes of the ellipse as $A = \sqrt{a^2 + b^2}$. It is related to the intensity I by $I = \boldsymbol{E}^\dagger \boldsymbol{E} = A^2 = a^2 + b^2$, where $\boldsymbol{E}$ is the electric field strength and $\dagger$ denotes a Hermitian conjugate. The absolute phase provides information about the initial state. It is an angle between the electric field vector in time $t = 0$ and the major axis of the ellipse, thus it ranges from $-\pi$ to π.

The simplest, yet powerful description of polarized light in optical system is Jones calculus [69], which deals with completely polarized light, i.e. light that can be considered as consisting of only one polarization state. The light is represented by Jones vectors and optical elements by Jones matrices. This allows us to easily calculate the polarization outcome of light passed through an optical system.

In order to work with Jones calculus, we first introduce the Jones vector. Let us have a completely polarized monochromatic plane wave, which propagates along the z axis as in Fig. 2.1. It can be expressed as a superposition of two components, which oscillate in the directions of x and y axes, as

$$\boldsymbol{E}(z,t) = [A_{0x}e^{i(\omega t - k_z z + \delta_x)}]\boldsymbol{x} + [A_{0y}e^{i(\omega t - k_z z + \delta_y)}]\boldsymbol{y}. \tag{2.2}$$

The two components have amplitudes A_{0x}, A_{0y} and absolute phases δ_x, δ_y; k_z denotes the z-component of the wave vector. The Jones vector can now be defined as

$$\boldsymbol{J} = \begin{bmatrix} A_{0x}e^{i\delta_x} \\ A_{0y}e^{i\delta_y} \end{bmatrix} = \begin{bmatrix} E_{0x} \\ E_{0y} \end{bmatrix}, \tag{2.3}$$

where E_{0x} and E_{0y} are complex amplitudes of the light wave. As we have already mentioned, the ellipse of polarization is fully described by four real parameters, therefore the two complex amplitudes E_{0x} and E_{0y} provide complete information about the polarization state of the light wave. However, we typically do not need to know magnitude of the ellipse, only the shape and handedness of the polarized light is important for us. We can therefore normalize the Jones vector to unitary intensity

$$I = \boldsymbol{E}^\dagger \boldsymbol{E} = a^2 + b^2 = A_{0x}^2 + A_{0y}^2 = 1. \tag{2.4}$$

If we further introduce $\tan\alpha = A_{0y}/A_{0x}$ and phase shift $\delta = \delta_y - \delta_x$, the normalized Jones vector can be defined as

$$\boldsymbol{J} = \begin{bmatrix} \cos\alpha \\ \sin(\alpha)e^{i\delta} \end{bmatrix} = \cos\alpha \boldsymbol{J}_x + \sin(\alpha)e^{i\delta}\boldsymbol{J}_y, \tag{2.5}$$

where the Cartesian basis of linear polarizations $\boldsymbol{J}_x$ and $\boldsymbol{J}_y$ is given as

$$\boldsymbol{J}_x = \begin{bmatrix} 1 \\ 0 \end{bmatrix}, \qquad \boldsymbol{J}_y = \begin{bmatrix} 0 \\ 1 \end{bmatrix} \tag{2.6}$$

and relations of α and δ to the azimuth θ and ellipticity ϵ are [69]

$$\tan 2\theta = \tan 2\alpha \cos\delta, \tag{2.7}$$

$$\sin 2\epsilon = \sin 2\alpha \sin\delta. \tag{2.8}$$

Having described the polarized light wave, next we need to find out the polarization change while passing through the optical system. In Jones calculus, any reflection or transmission element, which affects the light wave polarization, can be characterized by 2×2 matrix.

In order to describe response of a reflection element, we consider two coordinate systems $\mathrm{S}^{(I)}$ and $\mathrm{S}^{(R)}$ as shown in Fig. 2.2(a). Direction of x axes is perpendicular to the plane of incidence. Light, which is linearly polarized in this direction, is called s-polarized (from German *senkrecht* - perpendicular). Direction of y axes is parallel to the plane of incidence. Light linearly polarized in this direction is called p-polarized. In case of normal light incidence this distinction becomes irrelevant.

In the system $\mathrm{S}^{(I)}$, polarization of the incident wave is characterized by Jones vector $\boldsymbol{J}^{(I)}$. In the system $\mathrm{S}^{(R)}$, reflected wave is described by Jones vector $\boldsymbol{J}^{(R)}$.

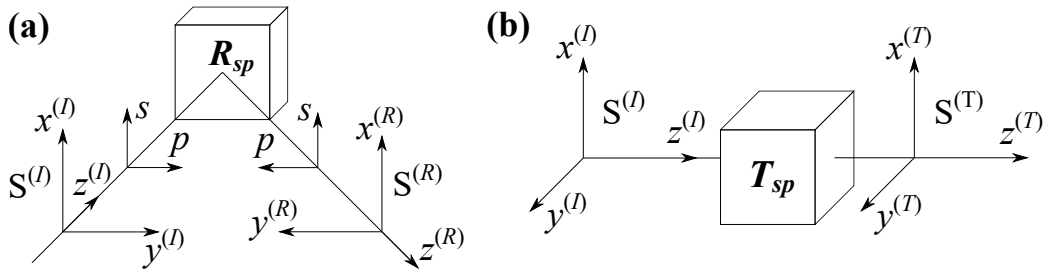

Figure 2.2: (a) Reflection optical element characterized by Jones reflection matrix $\boldsymbol{R}_{sp}$ in coordinate system of incident $\mathrm{S}^{(I)}$ and reflected wave $\mathrm{S}^{(R)}$. (b) Transmission optical element characterized by Jones transmission matrix $\boldsymbol{T}_{sp}$ in coordinate system of incident $\mathrm{S}^{(I)}$ and transmitted wave $\mathrm{S}^{(T)}$.

Both vectors are related by transformation, which can be written in a matrix form

$$\boldsymbol{J}^{(R)} = \boldsymbol{R}_{sp} \cdot \boldsymbol{J}^{(I)}, \tag{2.9}$$

where $\boldsymbol{R}_{sp}$ is the Jones reflection matrix

$$\boldsymbol{R}_{sp} = \begin{bmatrix} r_{ss} & r_{sp} \\ r_{ps} & r_{pp} \end{bmatrix}, \tag{2.10}$$

which characterizes change of polarization state of the light wave reflected on an arbitrary structure. Meaning of the matrix elements follows from the defining equation (2.9). If we denote complex amplitudes of both incident and reflected wave $E_{0x} = E_{0s}$ and $E_{0y} = E_{0p}$, we get

$$r_{ss} = \left(\frac{E_{0s}^{(R)}}{E_{0s}^{(I)}} \right)_{E_{0p}^{(I)}=0}, \tag{2.11}$$

$$r_{sp} = \left(\frac{E_{0s}^{(R)}}{E_{0p}^{(I)}} \right)_{E_{0s}^{(I)}=0}, \tag{2.12}$$

$$r_{ps} = \left(\frac{E_{0p}^{(R)}}{E_{0s}^{(I)}} \right)_{E_{0p}^{(I)}=0}, \tag{2.13}$$

$$r_{pp} = \left(\frac{E_{0p}^{(R)}}{E_{0p}^{(I)}} \right)_{E_{0s}^{(I)}=0}. \tag{2.14}$$

In order to describe response of a transmission element, we use two Cartesian coordinate systems $\mathrm{S}^{(I)}$ and $\mathrm{S}^{(T)}$ as defined in Fig. 2.2(b). Axes $x^{(I)}$ and $x^{(T)}$ are parallel, $y^{(I)}$ and $y^{(T)}$ are also parallel, $z^{(I)}$ and $z^{(T)}$ are identical. In analogy to the previous case of reflection, Jones vector $\boldsymbol{J}^{(I)}$ describes polarization of the incident wave in the system $\mathrm{S}^{(I)}$ and Jones vector $\boldsymbol{J}^{(T)}$ characterizes the reflected light in the system $\mathrm{S}^{(T)}$. Their relation can be then written in a matrix form

$$\boldsymbol{J}^{(T)} = \boldsymbol{T}_{sp} \cdot \boldsymbol{J}^{(I)}, \tag{2.15}$$

where $\boldsymbol{T}_{sp}$ stands for Jones transmission matrix of a given optical element. It can be expressed as

$$\boldsymbol{T}_{sp} = \begin{bmatrix} t_{ss} & t_{sp} \\ t_{ps} & t_{pp} \end{bmatrix}. \tag{2.16}$$

Meaning of the matrix elements is analogically to the reflection case determined by eq. (2.15). We can write

$$t_{ss} = \left(\frac{E_{0s}^{(T)}}{E_{0s}^{(I)}}\right)_{E_{0p}^{(I)}=0}, \tag{2.17}$$

$$t_{sp} = \left(\frac{E_{0s}^{(T)}}{E_{0p}^{(I)}}\right)_{E_{0s}^{(I)}=0}, \tag{2.18}$$

$$t_{ps} = \left(\frac{E_{0p}^{(T)}}{E_{0s}^{(I)}}\right)_{E_{0p}^{(I)}=0}, \tag{2.19}$$

$$t_{pp} = \left(\frac{E_{0p}^{(T)}}{E_{0p}^{(I)}}\right)_{E_{0s}^{(I)}=0}. \tag{2.20}$$

Now we have defined all necessary elements and we can describe response of the whole optical system. Let us have a system consisting of N optical elements, which are described by Jones matrices $\boldsymbol{X}_1$, $\boldsymbol{X}_2$, ..., $\boldsymbol{X}_N$, where $\boldsymbol{X}$ stands for either reflection or transmission matrix. If we assume that light passes through the elements in consecutive order $1, 2, \ldots, N$, then the relation between the incident and final Jones vectors $\boldsymbol{J}^{(I)}$ and $\boldsymbol{J}^{(X)}$ is given as

$$\boldsymbol{J}^{(X)} = \boldsymbol{X}_N \cdot \boldsymbol{X}_{N-1} \cdots \boldsymbol{X}_1 \cdot \boldsymbol{J}^{(I)}. \tag{2.21}$$

2.2 Magneto-optical angles

Having introduced basic theory of polarized light, we will now be defining magneto-optical (MO) quantities with use of the Jones formalism. In section 2.1 we explained that in order to describe polarization state, neither the amplitude nor the absolute phase of the light wave are necessary. We need the two real parameters (θ, ϵ) or (α, δ). It is therefore convenient to further work with the complex polarization parameter χ, which is given by ratio of the second and first component of Jones vector. As then follows from eq. (2.5), one can write

$$\chi = \frac{E_{0y}}{E_{0x}} = \tan(\alpha) e^{i\delta}. \tag{2.22}$$

The parameters (α, δ) are then related to the complex polarization parameter χ simply by

$$|\chi| = \tan\alpha, \tag{2.23}$$

$$\arg\chi = \delta. \tag{2.24}$$

If we now take a Jones vector of arbitrary elliptical polarization, given by its azimuth θ and ellipticity angle ϵ in Cartesian representation, we can further relate the complex polarization parameter χ to θ and ϵ by [70]

$$\chi = \frac{\sin\theta\cos\epsilon + i\cos\theta\sin\epsilon}{\cos\theta\cos\epsilon - i\sin\theta\sin\epsilon} = \frac{\tan\theta + i\tan\epsilon}{1 - i\tan\theta\tan\epsilon}. \tag{2.25}$$

Assuming small angles θ and ϵ, we can approximate tangents by their arguments: $\tan\theta \approx \theta, \tan\epsilon \approx \epsilon$. If we also neglect the second order term in denominator of eq. (2.25), it simplifies into

$$\chi \approx \theta + i\epsilon. \tag{2.26}$$

Before we finally relate the complex polarization parameter to magneto-optical angles, we need to introduce the coordinate system of our experiment. Typically we work in the Cartesian basis of s-polarized and p-polarized wave as defined in Fig. 2.2.

Let us have in such system an optically isotropic sample, which is characterized by diagonal Jones reflection matrix. If an s-polarized incident wave, which comes from optically isotropic medium (typically air), is reflected upon this sample, its polarization state remains unchanged due to diagonality of the Jones reflection matrix. The same situation occurs in case of a p-polarized wave. Its polarization does not change when reflecting upon optically isotropic sample.

Different situation occurs in case of an optically anisotropic sample. In our experiment the anisotropy is induced by non-zero magnetic moment of magnetized ferromagnetic material. The Jones reflection matrix then acquires non-zero off-diagonal elements and a change of polarization state of incident s or p-polarized wave can be observed upon reflection on such sample.

Let us consider the case of s-polarized wave. Using eqs. (2.11) and (2.13), we can express ratio of the off-diagonal r_{ps} to the diagonal r_{ss} element of Jones reflection matrix as

$$\frac{r_{ps}}{r_{ss}} = \left(\frac{\frac{E_{0p}^{(R)}}{E_{0s}^{(I)}}}{\frac{E_{0s}^{(R)}}{E_{0s}^{(I)}}} \right)_{E_{0p}^{(I)}=0} = \left(\frac{E_{0p}^{(R)}}{E_{0s}^{(R)}} \right)_{E_{0p}^{(I)}=0} = \chi^{(R)}_{E_{0p}^{(I)}=0} = \chi_s^{(R)}, \tag{2.27}$$

where we used definition (2.22) of the complex polarization parameter χ to get the third equality. We can therefore denote the ratio as complex polarization parameter $\chi_s^{(R)}$ of the reflected wave. In our case parameters $\theta^{(R)}$ and $\epsilon^{(R)}$ of the reflected wave are small enough to simplify eq. (2.25) and write expression analogical to (2.26)

$$\chi_s^{(R)} \approx \theta^{(R)} + i\epsilon^{(R)}. \tag{2.28}$$

Now we can finally define the complex Kerr magneto-optical angle Φ_{Ks} for incident s-polarized wave as

$$\Phi_{Ks} \stackrel{\text{def}}{=} -\frac{r_{ps}}{r_{ss}} = -\chi_s^{(R)} \approx \theta_{Ks} - i\epsilon_{Ks}, \tag{2.29}$$

where θ_{Ks} and ϵ_{Ks} are the magneto-optical angles called Kerr rotation and Kerr ellipticity,

$$\theta_{Ks} \stackrel{\text{def}}{\approx} -\theta^{(R)}, \tag{2.30}$$

$$\epsilon_{Ks} \stackrel{\text{def}}{\approx} \epsilon^{(R)}. \tag{2.31}$$

In case of incident p-polarized wave we can proceed in analogical way. Using eqs. (2.12) and (2.14) we find out that ratio of the off-diagonal r_{sp} to diagonal

r_{pp} element of Jones reflection matrix equals to inverse value of the complex polarization parameter $\chi_p^{(R)}$ of reflected wave. We can further simplify the inverse value of complex polarization parameter [70], thus the complex Kerr MO angle for incident p-polarized wave can be defined as

$$\Phi_{Kp} \overset{\text{def}}{=} \frac{r_{sp}}{r_{pp}} = (\chi_p^{(R)})^{-1} \approx \theta_{Kp} - i\epsilon_{Kp}, \tag{2.32}$$

where Kerr rotation θ_{Kp} and Kerr ellipticity ϵ_{Kp} are given by

$$\theta_{Kp} \overset{\text{def}}{\approx} -\theta^{(R)} + \frac{\pi}{2}, \tag{2.33}$$

$$\epsilon_{Kp} \overset{\text{def}}{\approx} \epsilon^{(R)}. \tag{2.34}$$

In case of normal light incidence there is no plane of incidence and no distinction between s-polarized and p-polarized incident wave. Therefore we expect both definitions to become equal with the same resulting complex Kerr MO angles for both incident polarizations. It can be shown [71] that in case of normal light incidence the diagonal and off-diagonal elements of Jones reflection matrix are related by

$$r_{pp} = -r_{ss}, \qquad r_{ps} = r_{sp}, \tag{2.35}$$

therefore the definitions (2.29) and (2.32) give the same final expression of the complex Kerr MO angle Φ_K in case of normal light incidence,

$$\Phi_{Ks} = \Phi_{Kp} = \Phi_K = -\frac{r_{ps}}{r_{ss}} \approx \theta_K - i\epsilon_K, \tag{2.36}$$

where θ_K and ϵ_K are the MO angles Kerr rotation and Kerr ellipticity.

2.3 Permittivity tensor

Main goal of the second chapter is to present mathematical apparatus for theoretical calculation of MO response. In order to do so, we need to introduce the permittivity tensor, which provides the way to insert physical input into the basic definition of MO angles presented in previous section. It provides information about material properties of the investigated system. Knowledge of the full permittivity tensor allows us to solve the wave equation, as we will show later on in this chapter, and thus to obtain reflectivity coefficients needed to calculate MO angles via eq. (2.36).

Material properties are usually described by either permittivity, optical conductivity or susceptibility, which are all mutually related. Here we focus on the permittivity. In general it is a second-order tensor

$$\boldsymbol{\varepsilon} = \begin{bmatrix} \varepsilon_{xx} & \varepsilon_{xy} & \varepsilon_{xz} \\ \varepsilon_{yx} & \varepsilon_{yy} & \varepsilon_{yz} \\ \varepsilon_{zx} & \varepsilon_{zy} & \varepsilon_{zz} \end{bmatrix}, \tag{2.37}$$

but as we will show later, the general form can be significantly simplified in special cases.

When a material is inserted into external magnetic field $\boldsymbol{M} = (M_x, M_y, M_z)$, the material and consequently its permittivity tensor becomes affected by this

external field. However, the influence is typically small, so that it can be considered as a small perturbation of the system, and we can expand elements of the permittivity tensor into MacLaurin series

$$\varepsilon_{ij} = \varepsilon_{ij}(0) + \left(\frac{\partial \varepsilon_{ij}}{\partial M_k}\right)_{M=0} M_k + \left(\frac{\partial^2 \varepsilon_{ij}}{\partial M_k \partial M_l}\right)_{M=0} M_k M_l + \dots \tag{2.38}$$

Here M_k and M_l are components of the magnetization vector, i, j, k, l are indeces of the Cartesian axes x, y, z. The first term of eq. (2.38) $\varepsilon_{ij}(0)$ determines the tensor elements in case that no external magnetic field is applied. The next terms are related to linear and quadratic MO effects. In this work we deal only with magneto-optical Kerr effect (MOKE), which is linearly proportional to magnetization, therefore restriction to first two terms in the series (2.38) is sufficient.

For investigation of the magneto-optical Kerr effect, there are three basic geometries. As shown in Fig. 2.3, distinction between the three configurations is given by relative orientation of the magnetization vector $\boldsymbol{M}$ to the plane of incidence and sample surface. In polar geometry, the magnetization vector lies in the plane of incidence and it is perpendicular to sample surface, i.e. it points against the direction of z axis. In longitudinal geometry, the magnetization vector lies in both the plane of incidence and the interface plane (it points along the y axis). Finally in transverse geometry, the magnetization vector lies in the surface plane and it is perpendicular to the plane of incidence (it points against the x axis). Here we are mostly interested in the case of polar geometry.

Let us now simplify the general form of the permittivity tensor (2.37). Typically, the diagonal elements are equal to each other and the off-diagonal in comparison to the diagonal are negligibly small,

$$\varepsilon_{ii} \approx \varepsilon_{jj}, \qquad \varepsilon_{ij} \ll \varepsilon_{jj}, \qquad i, j = x, y, z \text{ and } i \neq j. \tag{2.39}$$

Permittivity tensor in magnetic field has to satisfy symmetry arguments [71]. Considering also specific geometry of the polar configuration, as shown in Fig. 2.3,

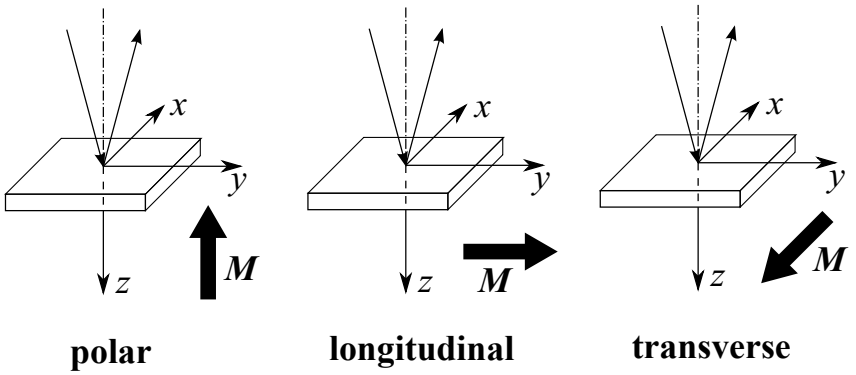

Figure 2.3: Three basic configurations of magneto-optical Kerr effect given by direction of the magnetization vector $\boldsymbol{M}$. The plane of incidence is schematically indicated by arrows representing the k vector of incident and reflected wave, it is indentical with the yz plane.

we can express the permittivity tensor as

$$\boldsymbol{\varepsilon} = \begin{bmatrix} \varepsilon_{xx} & \varepsilon_{xy} & 0 \\ -\varepsilon_{xy} & \varepsilon_{xx} & 0 \\ 0 & 0 & \varepsilon_{zz} \end{bmatrix} \approx \begin{bmatrix} \varepsilon_1 & -i\varepsilon_2 & 0 \\ i\varepsilon_2 & \varepsilon_1 & 0 \\ 0 & 0 & \varepsilon_1 \end{bmatrix}, \tag{2.40}$$

where to get the second equality we used approximation (2.39) and introduced notation

$$\varepsilon_1 = \varepsilon_{xx} \approx \varepsilon_{zz}, \qquad i\varepsilon_2 = -\varepsilon_{xy}. \tag{2.41}$$

The permittivity tensor in case of polar configuration then has only two independent complex elements: the diagonal element ε_1 and the off-diagonal element ε_2.

2.4 Microscopic theory of magneto-optical effects

Having introduced the permittivity tensor, next step is to calculate its elements. In this section we present classical and semiclassical approach for calculation of the diagonal and off-diagonal elements of permittivity tensor. The classical approach is suitable for description of the optical response of materials, and a basic formula for the off-diagonal elements can be also derived in the scope of this model. However, the semiclassical theory is necessary for more precise description of the magneto-optical effects.

2.4.1 Classical theory (Lorentz model)

Lorentz model is the classical microscopic approach, which describes interaction of light wave with harmonically bounded electron. Let us have the magnetic flux density of external magnetic field pointing against the direction of the z axis, i.e. $\boldsymbol{B} = (0, 0, -B_z)$. As we have mentioned in section 2.1, electric component of light wave dominates over the magnetic component in the interaction with matter. Therefore neglecting contribution of the magnetic field component, the equation of motion for electron in parabolic potential, interacting with a wave propagating along the z axis, is given by

$$m\frac{\partial^2 \boldsymbol{r}}{\partial t^2} + m\Gamma\frac{\partial \boldsymbol{r}}{\partial t} + m\omega_0^2 \boldsymbol{r} - e\frac{\partial \boldsymbol{r}}{\partial t} \times \boldsymbol{B} = eE_0 \mathrm{e}^{i\omega t}, \tag{2.42}$$

where m and e is the electron mass and elementary charge, $\boldsymbol{r}$ and ω_0 stand for electron's position vector and its natural frequency, $\Gamma = 1/\tau$ is a damping constant given by relaxation time τ and $E_0\mathrm{e}^{i\omega t}$ is electric component of the interacting wave. Eq. (2.42) can be decomposed into three components according to respective Cartesian axes, which consequently yields solution to all three components of the $\boldsymbol{r}$ vector.

In order to relate the $\boldsymbol{r}$ vector to permittivity tensor, we introduce the average dipole moment per unit volume $\boldsymbol{P}$ as

$$\boldsymbol{P} = Ne\boldsymbol{r}, \tag{2.43}$$

where N stands for concentration of electrons. If we further realize that the average dipole moment is identical with polarization density $\boldsymbol{P}$ defined as

$$\boldsymbol{P} = \varepsilon_0 \boldsymbol{\chi} \boldsymbol{E} = \varepsilon_0 (\boldsymbol{\varepsilon} - 1) \boldsymbol{E}, \tag{2.44}$$

where ε_0 is the permittivity of vacuum, $\boldsymbol{\chi}$ is the susceptibility tensor and $\boldsymbol{E}$ is external electric field of the light wave, then eqs. (2.43) and (2.44) bind together the components of position vector $\boldsymbol{r}$ with elements of the permittivity tensor $\boldsymbol{\varepsilon}$.

As the light wave propagates against z axis, from symmetry of the problem we would expect the z component of solution of eq. (2.42) to be different from the other two, yielding consequently different diagonal components of the permittivity tensor. However, as we have used (2.41) in order to simplify the tensor into (2.40), we obtain the diagonal permittivity tensor elements resulting from Lorentz model in identical form [71]

$$\varepsilon_1 = 1 + \omega_p^2 \frac{1}{\omega_0^2 - \omega^2 + i\Gamma\omega}, \tag{2.45}$$

where $\omega_p = Ne^2/m\varepsilon_0$ is the so called plasma frequency. Off-diagonal elements are then given by [71]

$$\varepsilon_2 = -\omega_p^2 \frac{\omega_c \omega}{\left(\omega_0^2 - \omega^2 + i\Gamma\omega\right)^2 - \omega_c^2 \omega^2}, \tag{2.46}$$

where frequency $\omega_c = -eB_z/m$ is the cyclotron frequency of circular electron motion in magnetic field.

2.4.2 Semiclassical theory

In the semiclassical theory of MO effects we still treat the light wave as a classical electromagnetic wave, the quantum description enters the problem on the part of the matter. MO effects arise from splitting of energy levels involved in given optical transitions. The splitting originates in spin-orbit coupling, which enables the electrons to distinguish between two senses of circularly polarized light. In absence of spin-orbit coupling, there is no contribution to off-diagonal permittivity tensor elements ($\varepsilon_2 = 0$) and therefore there are no MO effects. Optical transitions, which form the spectral dependence of the off-diagonal part of permittivity tensor and hence are MO active, can be sorted into two types, as presented in Fig. 2.4.

Type I are so called double transitions, which originate in spin-orbit splitting of the final states. Let us consider a transition from singlet ground state to excited state, which is split by spin-orbit interaction by ΔE given by [73]

$$\Delta E = 2\hbar\Delta\omega_0 = 2\hbar(\omega_{0+} - \omega_{0-}), \tag{2.47}$$

where $\omega_{0\pm}$ are resonant frequencies for left and right circular polarizations. Derivation of the spectral behaviour of the off-diagonal elements of permittivity tensor for such transition can be found elsewhere [73]. Here we skip the procedure, and assuming $\Delta\omega_0 \ll \Gamma_0$ we get the final formula in the form [74]

$$\varepsilon_2 = \Gamma_0^2 (\varepsilon_2^{'})_{max} \frac{(\omega - \omega_0)^2 - \Gamma_0^2 + 2i\Gamma_0(\omega - \omega_0)}{\left[(\omega - \omega_0)^2 + \Gamma_0^2\right]^2}, \tag{2.48}$$

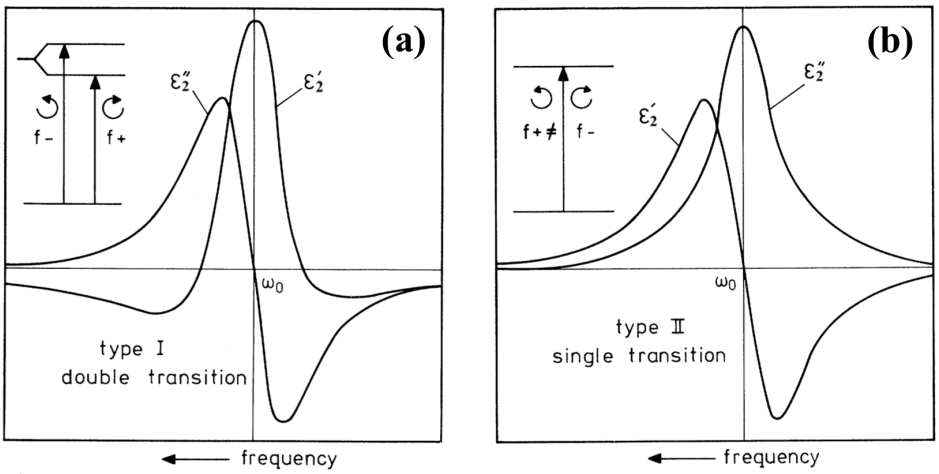

Figure 2.4: Spectral line shapes and mechanisms of two types of MO transitions; ω_0 is the resonant frequency, $\varepsilon_2^{'}$ and $\varepsilon_2^{''}$ denotes real and imaginary parts of ε_2. (a) Type I, so called double or diamagnetic transitions. Inset shows spin-orbit splitting of excited state. (b) Type II, so called single or paramagnetic transitions. Inset shows different oscillator strengths f_+ and f_- (taken from [72]).

where ω_0 and Γ_0 are the resonant frequency and half-width at half-maximum, $(\varepsilon_2^{'})_{max}$ stands for the maximum amplitude of the real part of ε_2, which occurs for $\omega = \omega_0$. For historical reasons [75], optical transitions of this type are called diamagnetic transitions. Real and imaginary parts of ε_2 are even and odd functions of $(\omega - \omega_0)$, respectively. The real part has a simple dissipative line shape and the imaginary part exhibits simple dispersive behaviour, as shown in Fig. 2.4(a).

Type II are so called single transitions. In this case there is no splitting of the energy levels, the spin-orbit interaction causes a difference between oscillator strengths f_+ and f_- of respective circular polarizations. The difference can be evaluated by quantity called the fractional dichroism $\xi = (f_- - f_+)/(f_- + f_+)$. Spectral dependence of these transitions can be derived analogically [73], the off-diagonal elements of permittivity tensor are given by [74]

$$\varepsilon_2 = 2\Gamma_0(\varepsilon_2^{''})_{max}\frac{\omega(\omega^2 - \omega_0^2 + \Gamma_0^2) - i\Gamma_0(\omega^2 + \omega_0^2 - \Gamma_0^2)}{(\omega^2 - \omega_0^2 - \Gamma_0^2)^2 + 4\Gamma_0^2\omega^2}, \tag{2.49}$$

where $(\varepsilon_2^{''})_{max}$ is the maximum amplitude of the imaginary part of ε_2, which occurs for $\omega = \omega_0$. For historical reasons [75], these transitions are called paramagnetic transitions. Real and imaginary parts of ε_2 are odd and even functions of $(\omega - \omega_0)$, respectivelly. For $\Gamma_0 \ll \omega_0$, their spectral shapes are opposite to previous case. The real part exhibits simple dispersive behaviour while the imaginary part has a simple dissipative line shape, as shown in Fig. 2.4(b).

2.5 Macroscopic theory of magneto-optical effects (Yeh formalism)

In this section we will crown the theory of MO effects. Earlier in section 2.2 we have defined MO angles by reflection coefficients. In previous section we

have introduced microscopical models, which served us to derive both diagonal and off-diagonal elements of permittivity tensor. Here we will show how the permittivity enters the basic definition of MO angles and we will derive final expressions of MO angles, which allow us to calculate MO response of arbitrary multilayer structure. The transfer matrix formalism, which we present here, was initially developed by P. Yeh [76] and further extended for absorbing media by Š. Višňovský [77].

First let us describe the sample, in which we want to calculate the MO response. We consider a structure consisting of N layers, as shown in Fig. 2.5. All interfaces of the multilayer are mutually parallel and they are also perpendicular to z axis. Surrounding half spaces 0 and $N+1$ are isotropic media, which are characterized by permittivity scalars $\varepsilon^{(0)}$ and $\varepsilon^{(N+1)}$. Each of the N layers is characterized by complex permittivity tensor $\boldsymbol{\varepsilon}^{(n)}$ and thickness t_n for $n = 1, 2, \ldots, N$. Plane of incidence is perpendicular to x axis, making the x component of wave vector equal to zero. Angle of incidence is denoted by φ_0.

In order to calculate the MO response, we need to solve the wave equation in all layers of the investigated sample. Let us consider the sample to be magnetized ferromagnetic (therefore optically anisotropic) medium without free charges, which is impacted by monochromatic plane wave with defined polarization, com-

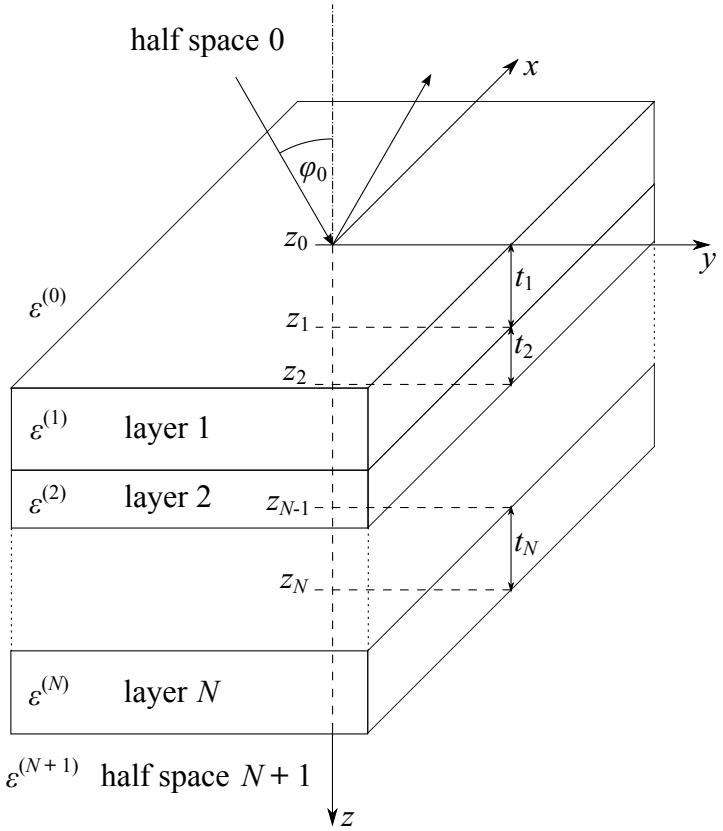

Figure 2.5: Multilayer structure consisting of N optically anisotropic layers and surrounded by two optically isotropic half spaces; $\varepsilon^{(0)}$ and $\varepsilon^{(N+1)}$ are permittivity scalars of the half spaces, $\boldsymbol{\varepsilon}^{(n)}$ and t_n for $n = 1, \ldots, N$ are complex permittivity tensors and thicknesses of the layers, z_n for $n = 0, \ldots, N$ denotes z coordinates of the interfaces and φ_0 stands for the angle of incidence.

ing from vacuum or air. Electromagnetic wave in such medium can be described by Maxwell and constitutive equations. In general, the relative permittivity and permeability are second-order tensors. For now we assume the permittivity tensor in its general form (2.37), while it has been shown elsewhere [78] that the relative permeability $\mu = 1$ is a suitable simplification. Wave equation for the electric component of the wave in n-th layer is then given in its well known form as

$$\Delta \boldsymbol{E}^{(n)} - \frac{\boldsymbol{\varepsilon}^{(n)}}{c^2} \frac{\partial^2 \boldsymbol{E}^{(n)}}{\partial t^2} - \nabla \left(\nabla \cdot \boldsymbol{E}^{(n)} \right) = 0, \tag{2.50}$$

where c is the speed of light in vacuum. We assume solution of eq. (2.50) in form of plane wave with frequency ω and wave vector $\boldsymbol{k}^{(n)}$,

$$\boldsymbol{E}^{(n)} = \boldsymbol{E}_0^{(n)} e^{i(\omega t - \boldsymbol{k}^{(n)} \cdot \boldsymbol{r})}, \tag{2.51}$$

where $\boldsymbol{r}$ is the position vector. We further introduce reduced wave vector $\boldsymbol{N}^{(n)}$ as

$$\boldsymbol{N}^{(n)} = \frac{c}{\omega} \boldsymbol{k}^{(n)} = (N_x x + N_y y + N_z^{(n)} z). \tag{2.52}$$

Choice of the Cartesian system as shown in Fig. 2.5 yields its x component zero throughout the whole structure, while the y component is unchanged in all layers, given by Snell law as

$$N_y = N_0 \sin \varphi_0, \tag{2.53}$$

where N_0 is real refractive index of the isotropic front medium. Inserting such plane wave into eq. (2.50), it can be rewritten in a matrix form as [70]

$$\begin{bmatrix} \varepsilon_{xx}^{(n)} - N_y^2 - (N_z^{(n)})^2 & \varepsilon_{xy}^{(n)} & \varepsilon_{xz}^{(n)} \\ \varepsilon_{yx}^{(n)} & \varepsilon_{yy}^{(n)} - (N_z^{(n)})^2 & \varepsilon_{yz}^{(n)} + N_y N_z^{(n)} \\ \varepsilon_{zx}^{(n)} & \varepsilon_{zy}^{(n)} + N_y N_z^{(n)} & \varepsilon_{zz}^{(n)} - N_y^2 \end{bmatrix} \begin{bmatrix} E_{0x}^{(n)} \\ E_{0y}^{(n)} \\ E_{0z}^{(n)} \end{bmatrix} = 0, \tag{2.54}$$

where $E_{0x}^{(n)}, E_{0y}^{(n)}$ and $E_{0z}^{(n)}$ are components of the complex wave amplitude. Nontrivial solution of eq. (2.54) is given by condition of zero determinant, which leads to characteristic equation for four eigenvalues $N_{zj}^{(n)}$. The four solutions describe four eigenmodes of light waves in a given layer n. The modes are determined by four eigenvectors $\boldsymbol{e}_j^{(n)}$ and four eigenvalues $N_{zj}^{(n)}$, giving general solution of eq. (2.54) as their linear combination

$$\boldsymbol{E}^{(n)} = \sum_{j=1}^{4} E_{0j}^{(n)}(z_n) \boldsymbol{e}_j^{(n)} \mathrm{e}^{i\left\{\omega t - \frac{\omega}{c}\left[N_y y + N_{zj}^{(n)}(z - z_n)\right]\right\}}, \tag{2.55}$$

where z_n is z component of the interface between n-th and $n+1$st layer. Relation between electric and magnetic field component of electromagnetic wave follows from Maxwell equations as

$$\boldsymbol{B}^{(n)} = \frac{1}{c} \boldsymbol{N}^{(n)} \times \boldsymbol{E}^{(n)}. \tag{2.56}$$

Therefore the magnetic component will be given as

$$\boldsymbol{B}^{(n)} = \frac{1}{c} \sum_{j=1}^{4} E_{0j}^{(n)}(z_n) \boldsymbol{b}_j^{(n)} \mathrm{e}^{i\left\{\omega t - \frac{\omega}{c}\left[N_y y + N_{zj}^{(n)}(z - z_n)\right]\right\}}, \tag{2.57}$$

where the eigenvectors $\boldsymbol{b}_j^{(n)}$ are with respect to eq. (2.56) given by

$$\boldsymbol{b}_j^{(n)} = \boldsymbol{N}^{(n)} \times \boldsymbol{e}_j^{(n)}. \tag{2.58}$$

Having solution of the wave equation, next step will be application of boundary conditions. As follows from Maxwell equations, tangential components of the electric and magnetic field vectors are continuous at an interface between two media. With the solutions (2.55) and (2.57), this requirement can be expressed for $n-1$st and n-th layer as [70]

$$\sum_{j=1}^{4} E_{0j}^{(n-1)}(z_{n-1})\boldsymbol{e}_j^{(n-1)} \cdot \boldsymbol{x} = \sum_{j=1}^{4} E_{0j}^{(n)}(z_n)\boldsymbol{e}_j^{(n)} \cdot \boldsymbol{x} \mathrm{e}^{i\frac{\omega}{c}N_{zj}^{(n)}t_n}, \tag{2.59}$$

$$\sum_{j=1}^{4} E_{0j}^{(n-1)}(z_{n-1})\boldsymbol{b}_j^{(n-1)} \cdot \boldsymbol{y} = \sum_{j=1}^{4} E_{0j}^{(n)}(z_n)\boldsymbol{b}_j^{(n)} \cdot \boldsymbol{y} \mathrm{e}^{i\frac{\omega}{c}N_{zj}^{(n)}t_n}, \tag{2.60}$$

$$\sum_{j=1}^{4} E_{0j}^{(n-1)}(z_{n-1})\boldsymbol{e}_j^{(n-1)} \cdot \boldsymbol{y} = \sum_{j=1}^{4} E_{0j}^{(n)}(z_n)\boldsymbol{e}_j^{(n)} \cdot \boldsymbol{y} \mathrm{e}^{i\frac{\omega}{c}N_{zj}^{(n)}t_n}, \tag{2.61}$$

$$\sum_{j=1}^{4} E_{0j}^{(n-1)}(z_{n-1})\boldsymbol{b}_j^{(n-1)} \cdot \boldsymbol{x} = \sum_{j=1}^{4} E_{0j}^{(n)}(z_n)\boldsymbol{b}_j^{(n)} \cdot \boldsymbol{x} \mathrm{e}^{i\frac{\omega}{c}N_{zj}^{(n)}t_n}. \tag{2.62}$$

It can be further rewritten in a matrix form as

$$\boldsymbol{D}^{(n-1)}\boldsymbol{E}_0^{(n-1)}(z_{n-1}) = \boldsymbol{D}^{(n)}\boldsymbol{P}^{(n)}\boldsymbol{E}_0^{(n)}(z_n), \tag{2.63}$$

where we introduced the so called dynamical $\boldsymbol{D}^{(n)}$ and propagation $\boldsymbol{P}^{(n)}$ matrix of n-th layer. The dynamical matrix characterizes transformation of the light wave at interface. It consists of x and y components of the eigenmodes as

$$\boldsymbol{D}^{(n)} = \begin{bmatrix} \boldsymbol{e}_1^{(n)} \cdot \boldsymbol{x} & \boldsymbol{e}_2^{(n)} \cdot \boldsymbol{x} & \boldsymbol{e}_3^{(n)} \cdot \boldsymbol{x} & \boldsymbol{e}_4^{(n)} \cdot \boldsymbol{x} \\ \boldsymbol{b}_1^{(n)} \cdot \boldsymbol{y} & \boldsymbol{b}_2^{(n)} \cdot \boldsymbol{y} & \boldsymbol{b}_3^{(n)} \cdot \boldsymbol{y} & \boldsymbol{b}_4^{(n)} \cdot \boldsymbol{y} \\ \boldsymbol{e}_1^{(n)} \cdot \boldsymbol{y} & \boldsymbol{e}_2^{(n)} \cdot \boldsymbol{y} & \boldsymbol{e}_3^{(n)} \cdot \boldsymbol{y} & \boldsymbol{e}_4^{(n)} \cdot \boldsymbol{y} \\ \boldsymbol{b}_1^{(n)} \cdot \boldsymbol{x} & \boldsymbol{b}_2^{(n)} \cdot \boldsymbol{x} & \boldsymbol{b}_3^{(n)} \cdot \boldsymbol{x} & \boldsymbol{b}_4^{(n)} \cdot \boldsymbol{x} \end{bmatrix}. \tag{2.64}$$

The propagation matrix describes propagation of the light wave in n-th layer. It is given as

$$\boldsymbol{P}^{(n)} = \begin{bmatrix} \mathrm{e}^{i\frac{\omega}{c}N_{z1}^{(n)}t_n} & 0 & 0 & 0 \\ 0 & \mathrm{e}^{i\frac{\omega}{c}N_{z2}^{(n)}t_n} & 0 & 0 \\ 0 & 0 & \mathrm{e}^{i\frac{\omega}{c}N_{z3}^{(n)}t_n} & 0 \\ 0 & 0 & 0 & \mathrm{e}^{i\frac{\omega}{c}N_{z4}^{(n)}t_n} \end{bmatrix}. \tag{2.65}$$

We can further rewrite the matrix form of continuity requirements (2.63) as

$$\boldsymbol{E}_0^{(n-1)}(z_{n-1}) = \left(\boldsymbol{D}^{(n-1)}\right)^{-1}\boldsymbol{D}^{(n)}\boldsymbol{P}^{(n)}\boldsymbol{E}_0^{(n)}(z_n) = \boldsymbol{T}^{(n-1,n)}\boldsymbol{E}_0^{(n)}(z_n), \tag{2.66}$$

where we introduced the transfer matrix $\boldsymbol{T}^{(n-1,n)}$. It binds the field components in two adjacent layers. The field components are bound analogically at all interfaces for $n = 1, \ldots, N+1$, except for the last interface. Propagation of the light

wave after this interface cannot be characterized by propagation matrix, because we find ourselves in the second half space with no defined thickness. The last transfer matrix therefore consists of only the dynamical matrices

$$\boldsymbol{E}_0^{(N)}(z_N) = \left(\boldsymbol{D}^{(N)}\right)^{-1} \boldsymbol{D}^{(N+1)} \boldsymbol{E}_0^{(N+1)}(z_N) = \boldsymbol{T}^{(N,N+1)} \boldsymbol{E}_0^{(N+1)}(z_N). \tag{2.67}$$

If we then successively multiply all transfer matrices, we can express relation between light waves in the two surrounding media as

$$\boldsymbol{E}_0^{(0)}(z_0) = \left(\prod_{n=1}^{N+1} \boldsymbol{T}^{(n-1,n)}\right) \boldsymbol{E}_0^{(N+1)}(z_N) = \boldsymbol{M}\boldsymbol{E}_0^{(N+1)}(z_N), \tag{2.68}$$

where we introduced the matrix $\boldsymbol{M}$, which characterizes an arbitrary anisotropic multilayer.

In the last step we rewrite eq. (2.68) using two assumptions. We assume that the incident wave in the front half space can be decomposed into two orthogonal polarizations (eigenvectors) $\boldsymbol{e}_1^{(0)}$ and $\boldsymbol{e}_3^{(0)}$ with amplitudes $E_{01}^{(0)}$ and $E_{03}^{(0)}$. Analogically, the components of the reflected wave in the front half space are described by orthogonal polarizations $\boldsymbol{e}_2^{(0)}$ and $\boldsymbol{e}_4^{(0)}$ with amplitudes $E_{02}^{(0)}$ and $E_{04}^{(0)}$. We next take into account that there is no source of light in the back half space, therefore $E_{02}^{(N+1)} = E_{04}^{(N+1)} = 0$. Eq. (2.68) can then be written as

$$\begin{bmatrix} E_{01}^{(0)} \\ E_{02}^{(0)} \\ E_{03}^{(0)} \\ E_{04}^{(0)} \end{bmatrix} = \begin{bmatrix} M_{11} & M_{12} & M_{13} & M_{14} \\ M_{21} & M_{22} & M_{23} & M_{24} \\ M_{31} & M_{32} & M_{33} & M_{34} \\ M_{41} & M_{42} & M_{43} & M_{44} \end{bmatrix} \begin{bmatrix} E_{01}^{(N+1)} \\ 0 \\ E_{03}^{(N+1)} \\ 0 \end{bmatrix}. \tag{2.69}$$

From eq. (2.69) we can finally calculate the reflection coefficients in terms of components of the matrix $\boldsymbol{M}$. They are given by [79]

$$r_{21} = \left(\frac{E_{02}^{(0)}}{E_{01}^{(0)}}\right)_{E_{03}^{(0)}=0} = \frac{M_{21}M_{33} - M_{23}M_{31}}{M_{11}M_{33} - M_{13}M_{31}}, \tag{2.70}$$

$$r_{23} = \left(\frac{E_{02}^{(0)}}{E_{03}^{(0)}}\right)_{E_{01}^{(0)}=0} = \frac{M_{11}M_{23} - M_{21}M_{13}}{M_{11}M_{33} - M_{13}M_{31}}, \tag{2.71}$$

$$r_{41} = \left(\frac{E_{04}^{(0)}}{E_{01}^{(0)}}\right)_{E_{03}^{(0)}=0} = \frac{M_{41}M_{33} - M_{43}M_{31}}{M_{11}M_{33} - M_{13}M_{31}}, \tag{2.72}$$

$$r_{43} = \left(\frac{E_{04}^{(0)}}{E_{03}^{(0)}}\right)_{E_{01}^{(0)}=0} = \frac{M_{11}M_{43} - M_{41}M_{13}}{M_{11}M_{33} - M_{13}M_{31}}. \tag{2.73}$$

Assuming that the decomposition of incident and reflected wave into two orthogonal polarizations consists of s-polarized and p-polarized component, the reflection coefficients (2.70) - (2.73) are related to their previous definition via Jones reflection matrix (2.10) as

$$\boldsymbol{R}_{sp} = \begin{bmatrix} r_{ss} & r_{sp} \\ r_{ps} & r_{pp} \end{bmatrix} = \begin{bmatrix} r_{21} & r_{23} \\ -r_{41} & -r_{43} \end{bmatrix}. \tag{2.74}$$

Therefore we have all we need in order to calculate the MO response of arbitrary anisotropic multilayer. The matrix $\boldsymbol{M}$ contains information about optical properties of all layers of the system. Its elements then express the reflection coefficients via eqs. (2.70) - (2.73) and according to definition (2.36) the resulting MO Kerr angle is given by ratio of the reflection coefficients.

Moreover a reverse procedure is also possible. Measuring first MO Kerr effect of given sample, from known MO response of the material we can derive elements of the permittivity tensor.

3. Experimental techniques

The third chapter provides a brief overview of the most important experimental methods that were used in this work. We start with pulsed laser deposition that was employed to grow all the investigated samples. Concerning X-ray diffraction, which is a standard characterization technique, we present here mainly the calculations necessary to determine the whole monoclinic unit cell from measured reciprocal space maps. Next we introduce the basic working principle of superconducting quantum interference device magnetometry that was used to characterize magnetic properties of our samples. The most important optical and magneto-optical techniques - spectroscopic ellipsometry, MO Kerr spectroscopy and microscopy - are presented in detail in terms of the Jones calculus, which was introduced in previous chapter. Last method is magnetic force microscopy that can provide complementary information about magnetic properties of the investigated samples.

3.1 Pulsed laser deposition

Discovery of laser in the 1960s was soon afterwards followed by first attempts to use it for thin films fabrication [80, 81]. At first however, quality of laser deposited films used to be inferior compared to other conventional methods as molecular beam epitaxy (MBE) or metalorganic chemical vapour deposition (MOCVD). In the late 1980s situation began to change, when groups of Dijkkamp *et al.* [82] and Inam *et al.* [83] by means of pulsed laser deposition (PLD) succeeded in high quality growth of superconducting Y-Ba-Cu-O thin films. Since then PLD has become widely spread method for fabrication of thin films of various materials, including metals, semiconductors, insulators, polymers and even biological materials [84].

Fig. 3.1 shows typical experimental set-up of PLD. The material we want to deposit as thin layer is placed in vacuum chamber in form of dense ceramic target. A laser pulse of short duration ($\sim$ ns) and high energy ($\sim$ J/cm^2) impacts on the ceramic target and ablates small amount of the material, which creates a plasma plume. After few microseconds, the plume hits a substrate placed in the chamber on a heater. The heater maintains the substrate at high temperature, typically hundreds of degrees Celsius. As reaching the substrate, the plume condenses contributing to volume of the growing film. Analogically to MBE, reflection high-energy electron diffraction (RHEED) can be utilized to monitor proper epitaxial growth of the films.

Concerning epitaxial (i.e. ordered oriented) growth, PLD has proven to be remarkably efficient when fabricating multicomponent inorganic materials [84]. The epitaxial growth can be achieved when the ablation plume consists mostly of atomic, diatomic and other low-mass components. This can be realized by nanosecond laser pulses of ultraviolet light, which cause strong absorption in small volume of the ceramic target. For other materials, such as polymers or organic materials, different conditions are applied. In addition to good epitaxial growth, PLD is of high interest for thin film growth due to other reasons, such as stoichiometric transfer of material between target and substrate or compatibility with

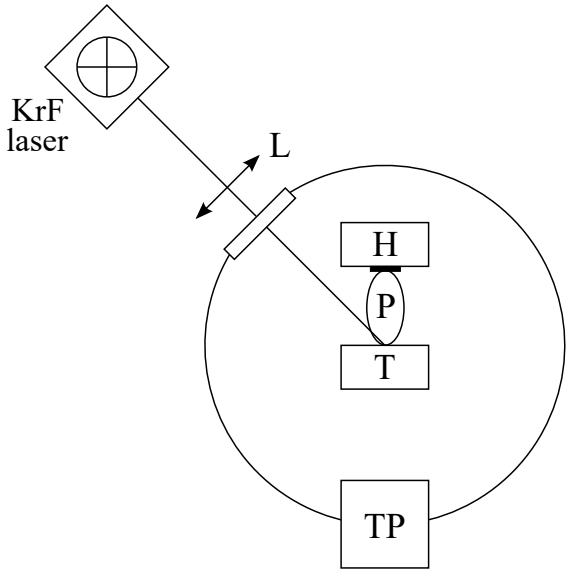

Figure 3.1: Schematic depiction of typical pulsed laser deposition system. The chamber is kept at high vacuum by turbomolecular pump (TP). Ultraviolet laser pulses are led to the chamber by a system of lenses (L) and other optical elements. Then the pulses ablate a ceramic target (T), and created plasma plume (P) hits a substrate placed on a heater (H).

backgroung pressures ranging from ultrahigh vacuum ($\sim 10^{-7}$ Pa) up to circa 10^2 Pa. In contrast to MOCVD, which works at almost atmospheric pressure, it is however necessary to have at least medium vacuum.

PLD process requires presence of a background gas, which serves two purposes. In case of oxide films, oxygen atmosphere helps to provide proper stoichiometry of the fabricated films. The second reason is due to relatively high energy of the ablated species, which according to plasma plume dynamics studies could reach several hundred electron volts [85]. However, already from energy ~ 50 eV the film structure could be damaged. The background gas can decrease energy of the species in the plume down below 1 eV and therefore prevent undesirable disruption of the growth process.

Post-deposition treatment might further improve quality of the films. In case of oxide materials, post-deposition oxygen annealing can either help to additionally oxidize the grown film or in contrary to remove extra oxygen. It has been shown that such treatment in oxide films leads to essential improvements of T_C and CMR [86].

3.2 X-ray diffraction

X-ray diffraction (XRD) is a basic characterization technique, which provides information about crystallographic structure and crystalline quality of investigated material. It is based on detection of X-rays diffracted on lattice planes of the investigated sample. Peak position of diffracted radiation is determined by Bragg law

$$2d_{hkl} \sin\theta = \lambda, \tag{3.1}$$

where d_{hkl} is distance between two lattice planes given by Miller indeces hkl, λ is the wavelength of X-ray radiation and θ is the angle of incidence, at which the diffraction peak occurs.

Fig. 3.2(a) shows basic XRD experimental set-up, where several rotation angles of the sample are defined. The sample can be rotated in the plane of incidence, as denoted by angle ω, which is measured between surface plane of the sample and incident X-ray beam. The angle 2θ is measured between incident and detected X-ray beam. The sample can be further rotated outside of the plane of incidence, as denoted by angles φ and ψ.

Basic XRD scan is a symmetric θ-2θ scan. In such scan the X-ray source is kept at fixed position. The sample and detector are then adjusted so that $\psi = 0$ and $\omega = 2\theta/2$, i.e. the diffracted intensity is always measured under the double of the angle of incidence 2θ. As a result, signal detected during this scan comes from diffraction on lattice planes parallel with sample surface, which provides information about the out-of-plane lattice parameter of the sample.

In order to describe the whole unit cell of the investigated sample, it is necessary to measure asymmetric scans, which can provide information about the in-plane lattice parameters. Asymmetric θ-2θ scan is performed similarly to the symmetric scan with one substantial difference, which is initial offset of the sample position given by the ω angle, which now $\omega \neq 2\theta/2$. The detected signal then comes from lattice planes which are no longer parallel to surface plane, i.e. given by arbitrary Miller indeces (hkl). When properly adjusting the azimuth φ, we can separate contributions of the two in-plane lattice parameters by measuring diffraction signal on the $(h0l)$ or $(0kl)$ lattice planes, respectively.

Set of multiple asymmetric scans for different values of ω offset is known as reciprocal space map (RSM) and it allows us to obtain complete information about unit cell of the investigated sample. As we have shown in section 1.3, epitaxial LSMO unit cell can be described as monoclinic. Therefore we now show how to calculate lattice parameters from RSMs in case of monoclinic unit cell.

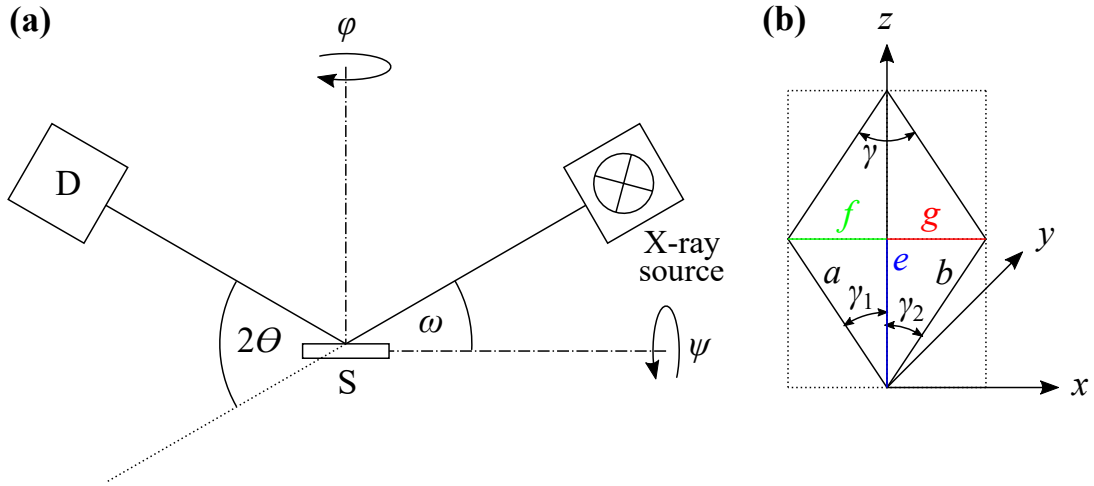

Figure 3.2: (a) Schematic diagram of basic X-ray diffraction experimental set-up; D - detector, S - sample, angles ω, φ and ψ define rotation of the sample, 2θ defines the detection angle. (b) Schematic representation of monoclinic unit cell with introduction of complementary quantities e, f, g and γ_1, γ_2.

We begin the calculation of monoclinic lattice parameters a, b, c and γ with introduction of basic quantities in both real and reciprocal space. Unit cell vectors $\boldsymbol{a}, \boldsymbol{b}$ and $\boldsymbol{c}$ in real space are related to reciprocal unit cell vectors $\boldsymbol{a}^*, \boldsymbol{b}^*$ and $\boldsymbol{c}^*$ as

$$\boldsymbol{a}^* = 2\pi \frac{\boldsymbol{b} \times \boldsymbol{c}}{V}, \qquad \boldsymbol{b}^* = 2\pi \frac{\boldsymbol{c} \times \boldsymbol{a}}{V}, \qquad \boldsymbol{c}^* = 2\pi \frac{\boldsymbol{a} \times \boldsymbol{b}}{V}, \tag{3.2}$$

where V stands for unit cell volume in real space

$$V = (\boldsymbol{a} \times \boldsymbol{b}) \cdot \boldsymbol{c}. \tag{3.3}$$

Diffraction peak described by Miller indeces hkl is then given by reciprocal space vector $\boldsymbol{Q}$ as

$$\boldsymbol{Q} = (Q_x, Q_y, Q_z) = h\boldsymbol{a}^* + k\boldsymbol{b}^* + l\boldsymbol{c}^*. \tag{3.4}$$

Fig. 3.2(b) shows monoclinic unit cell, in which we introduce several complementary quantities e, f, g and γ_1, γ_2. Their relation to unit cell parameters is apparent from the picture, they are given as

$$a = \sqrt{e^2 + f^2}, \qquad b = \sqrt{e^2 + g^2}, \tag{3.5}$$

$$\gamma = \gamma_1 + \gamma_2 = \arctan\left(\frac{f}{e}\right) + \arctan\left(\frac{g}{e}\right). \tag{3.6}$$

The unit cell vectors in real space can be expressed in terms of the complementary quantities as

$$\boldsymbol{a} = (-f, 0, e), \qquad \boldsymbol{b} = (g, 0, e), \qquad \boldsymbol{c} = (0, c, 0), \tag{3.7}$$

which inserted into eq. (3.3) yields the unit cell volume V as

$$V = (f + g)ec. \tag{3.8}$$

Inserting the unit cell vectors in the form (3.7) into eq. (3.2) and using the unit cell volume (3.8) gives us the reciprocal unit cell vectors as

$$\boldsymbol{a}^* = \frac{2\pi}{f+g}\left(-1, 0, \frac{g}{e}\right), \quad \boldsymbol{b}^* = \frac{2\pi}{f+g}\left(1, 0, \frac{f}{e}\right), \quad \boldsymbol{c}^* = \frac{2\pi}{c}(0, 1, 0). \tag{3.9}$$

Using now eq. (3.9) yields the components of reciprocal space vector $\boldsymbol{Q}$ (3.4) as

$$Q_x = \frac{2\pi}{f+g}(k - h), \tag{3.10}$$

$$Q_y = \frac{2\pi}{c} l, \tag{3.11}$$

$$Q_z = \frac{2\pi}{f+g}\left(h\frac{g}{e} + k\frac{f}{e}\right). \tag{3.12}$$

If we know coordinates of the reciprocal space vector $\boldsymbol{Q}$ from measured RSM, we can directly obtain lattice parameter c from eq. (3.11) for an arbitrary diffraction with non-zero Miller index l. Lateral periodicity $(f + g)$, which is usually known as the (ab) distance

$$(ab) = \sqrt{a^2 + b^2 - 2ab\cos\gamma}, \tag{3.13}$$

can be obtained from eq. (3.10) for a diffraction with $h \neq k$. To calculate the remaining parameters a, b and γ, we combine eqs. (3.10) and (3.12), which yields an equation with two unknown complementary quantities e and g

$$Q_z e + Q_x g = 2\pi k. \tag{3.14}$$

As we have only one equation for two unknown quantities, we need to use two diffractions with non-colinear reciprocal space vectors $\boldsymbol{Q}$, which gives us set of two linear equations for two unknown quantities e and g. As we already know the lateral distance $(f + g)$, f can be afterwards easily calculated and the lattice parameters a, b and γ are finally given by eqs. (3.5) and (3.6).

3.3 Superconducting quantum interference device magnetometry

Superconducting quantum interference device (SQUID) is a highly sensitive method designed for measurements of extremely weak magnetic signals down to 10^{-8} emu. Its working principle is based on application of Josephson effect [87, 88]. We distinguish two kinds of SQUID, based on number of employed Josephson junctions. The so called radio frequency (RF) SQUID contains only one Josephson junction, while direct current (DC) SQUID consists of two Josephson junctions. We will focus on DC-SQUID, which is more sensitive and it is employed in our experimental set-up.

Fig. 3.3(a) shows Quantum design commercial Magnetic Properties Measurement System (MPMS), which is a magnetometer of DC-SQUID type. Schematic

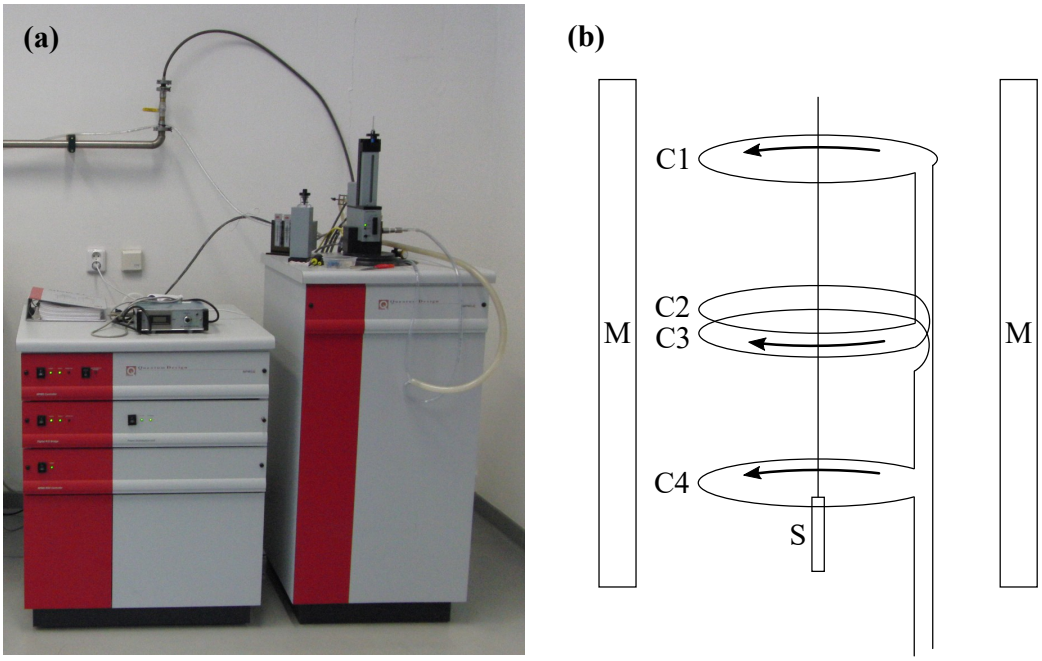

Figure 3.3: (a) Commercial Quantum design SQUID magnetometer MPMS XL 7T (taken from [89]). (b) Basic diagram of SQUID magnetometer; C1, C2, C3, C4 - pickup coils, M - superconducting electromagnet, S - sample.

diagram of its basic working principle is shown in Fig. 3.3(b). Measurement chamber contains superconducting electromagnet M, which provides external magnetic field in vertical direction, up to 7 T in case of the MPMS. Inside of the electromagnet M, there are four pickup coils C1 - C4, through which the sample S is moved during the measurement process. When moving sample through a pickup coil, positive or negative current is induced in the coil depending on sense of the coil winding and direction of the sample movement. Winding sense of coils C1 and C4 is opposite to that of coils C2 and C3, which results in bell shaped curve of the induced current. Two measurement modes are possible. During DC mode, sample is moved in one direction by discrete steps, recording the induced current at each position. The more precise reciprocating sample option (RSO) mode performs sinusoidal oscillations through the whole measuring space, while recording the induced current profile. The induced current is further brought to key element of the DC-SQUID, which are two Josephson junctions in parallel configuration. They allow to measure change of magnetic flux by the current induced in pickup coils. Fitting the space dependence of induced current by model function, combined with conversion via Josephson junctions allows eventually for presice determination of the sample magnetic moment.

The measuring chamber is typically placed in liquid helium, which allows proper functioning of the superconducting electromagnet. High temperature superconductors enabled construction of SQUID systems working with liquid nitrogen. Such systems are apparently more cost effective, however less sensitive as well. MPMS works with liquid helium in temperature range between 1.9 K and 400 K.

3.4 Spectroscopic ellipsometry

In previous chapter we learned how to calculate MO response of arbitrary multilayer. We have seen that the MO description requires detailed knowledge about optical properties of investigated materials, i.e. about diagonal elements of permittivity tensor. That is where spectroscopic ellipsometry (SE) plays an important role, providing information about the complex index of refraction, which is directly linked to the diagonal permittivity tensor elements. The SE is suitable for optical characterization of bulk crystals as well as thin films.

Fig. 3.4 shows basic experimental set-up of spectroscopic ellipsometer. Light coming out of the source passes through polarizer P, which makes the light wave linearly polarized. The light further reflects on the investigated sample S, passes through compensator C and analyzer A and finally it is measured by the detector D. Such sequence of optical elements is often reffered to as PSCA configuration.

Polarization plane defined by the polarizer P is given by angle α measured with respect to x axis, which is perpendicular to both wave vector and plane of incidence as defined in Fig. 2.2. In terms of Jones calculus, we can express Jones transmission matrix of the polarizer $\boldsymbol{T}_P$ as

$$\boldsymbol{T}_P = \begin{bmatrix} \cos^2\alpha & \cos\alpha\sin\alpha \\ \cos\alpha\sin\alpha & \sin^2\alpha \end{bmatrix}. \tag{3.15}$$

Reflection upon sample S is characterized by Jones reflection matrix as defined by eq. (2.10). Typically we deal with optically isotropic materials, in which case

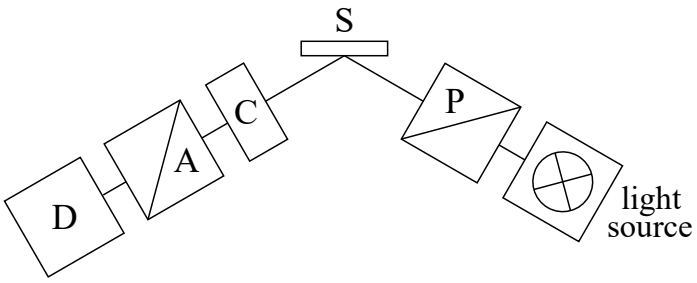

Figure 3.4: Basic experimental set-up of spectroscopic ellipsometry known as PSCA configuration; A - analyzer, C - compensator, D - detector, P - polarizer, S - sample.

the Jones reflection matrix $\boldsymbol{R}_{sp}$ has a simplified diagonal form

$$\boldsymbol{R}_{sp} = \begin{bmatrix} r_s & 0 \\ 0 & r_p \end{bmatrix}. \tag{3.16}$$

Typical SE set-up involves compensator C. It is usually a phase retarder, which allows to measure how much of the reflected light became unpolarized, e.g. due to non-uniformity of the sample or as a result of backside reflection at the film/substrate interface. Jones transmission matrix of the compensator $\boldsymbol{T}_C$ characterized by phase shift δ is given as

$$\boldsymbol{T}_C = \begin{bmatrix} \mathrm{e}^{i\frac{\delta}{2}} & 0 \\ 0 & \mathrm{e}^{-i\frac{\delta}{2}} \end{bmatrix}. \tag{3.17}$$

The analyzer A is a polarizer, which transmits linearly polarized light in plane given by angle ξ measured to x axis. Then analogically to eq. (3.15) Jones transmission matrix of the analyzer $\boldsymbol{T}_A$ is given as

$$\boldsymbol{T}_A = \begin{bmatrix} \cos^2\xi & \cos\xi\sin\xi \\ \cos\xi\sin\xi & \sin^2\xi \end{bmatrix}. \tag{3.18}$$

Relation between incident $\boldsymbol{J}^{(I)}$ and final $\boldsymbol{J}^{(X)}$ Jones vector, which determines light polarization state after passing through an arbitrary system of optical elements, is given by eq. (2.21). Knowing Jones matrices of all elements of SE system, we can then using eqs. (3.15) - (3.18) express the relation between incident and detected light as

$$\begin{aligned} \boldsymbol{J}^{(X)} = \boldsymbol{T}_A \cdot \boldsymbol{T}_C \cdot \boldsymbol{R}_{sp} \cdot \boldsymbol{T}_P \cdot \boldsymbol{J}^{(I)} = \begin{bmatrix} \cos^2\xi & \cos\xi\sin\xi \\ \cos\xi\sin\xi & \sin^2\xi \end{bmatrix} \cdot \\ \cdot \begin{bmatrix} \mathrm{e}^{i\frac{\delta}{2}} & 0 \\ 0 & \mathrm{e}^{-i\frac{\delta}{2}} \end{bmatrix} \cdot \begin{bmatrix} r_s & 0 \\ 0 & r_p \end{bmatrix} \cdot \begin{bmatrix} \cos^2\alpha & \cos\alpha\sin\alpha \\ \cos\alpha\sin\alpha & \sin^2\alpha \end{bmatrix} \cdot \boldsymbol{J}^{(I)}, \end{aligned} \tag{3.19}$$

which allows us to calculate the detected intensity I as

$$I = \left(\boldsymbol{J}^{(X)}\right)^{\dagger} \boldsymbol{J}^{(X)}. \tag{3.20}$$

SE works via investigation of change between s and p-polarized wave component upon reflection on the sample. This change can be expressed by complex reflectance ratio ρ as

$$\rho = r_p/r_s = \tan(\Psi)\mathrm{e}^{i\Delta}, \tag{3.21}$$

where we introduced the ellipsometric angles Ψ and Δ. We will not present here the full calculation of intensity according to eq. (3.20), it can be found elsewhere [69]. It can be shown that the detected intensity contains overall information, from which the ellipsometric angles Ψ and Δ can be extracted. Spectra of the ellipsometric angles then allow us to calculate optical properties of the sample, i.e. index of refraction n and extinction coefficient k. The complex index of refraction $\tilde{n} = n + ik$ is related to diagonal element of permittivity tensor $\varepsilon_1 = \varepsilon_1^{'} + i\varepsilon_1^{''}$ as

$$\varepsilon_1 = (\tilde{n})^2. \tag{3.22}$$

In addition to optical properties, we can also obtain refined values of layers thicknesses. In data processing procedure we consider model structure of the investigated sample and numerically adjust desired parameters by repeated comparison with experimental data. Typically we want to determine optical properties in one layer of multilayer structure, where optical properties of other layers as well as these of the substrate are known. Then in the layer of unknown properties, optical transitions in spectra of diagonal elements of permittivity tensor are modelled with corresponding line shapes, e.g. as Lorentz transitions as presented in section 2.4. Fitting such model to experimental data yields optimized parameters of the optical transitions and refined values of nominal layers thicknesses, which are also included in the initial model.

3.5 Magneto-optical Kerr spectroscopy

MO Kerr spectroscopy is a highly sensitive technique for measuring magnetic properties of materials. Its ability to detect MO angles with precision of millidegrees makes it suitable for probing weak signals of ultrathin films and multilayer systems. There are two basic classes of MO experimental methods. The simple class employs direct intensity detection, the more sophisticated methods are based on azimuth or ellipticity modulation combined with synchronic detection. The modulation techniques generally provide higher signal to noise ratio, however we have recently demonstrated that it is possible to achieve similar or even higher precision using one of the intensity methods [90, 91, 92].

Basic principle of MO spectroscopy is essentially identical to SE, which is why it is often referred to as generalized MO ellipsometry [79]. It is also based on investigation of light polarization change upon reflection on a sample. The main difference is introduced by magnetic field application, which makes the sample optically anisotropic. Figure 3.5 shows the experimental set-up of generalized MO ellipsometry with rotating analyzer. We can notice that it is very similar to basic set-up of SE, which we introduced in Fig. 3.4. Light coming out of the source passes through polarizer P, which defines linear polarization of the light wave. The light further reflects on the investigated sample S, which is placed in magnetic field. Then it optionally passes through compensator C and arrives at the key element of the system, which is the rotating analyzer A. Finally the light is measured by detector D.

Analogically to the case of SE, we can express the optical elements in terms of Jones calculus. Polarizer P defines linear polarization in plane given by angle α measured with respect to x axis, its Jones transmission matrix $\boldsymbol{T}_P$ is then given

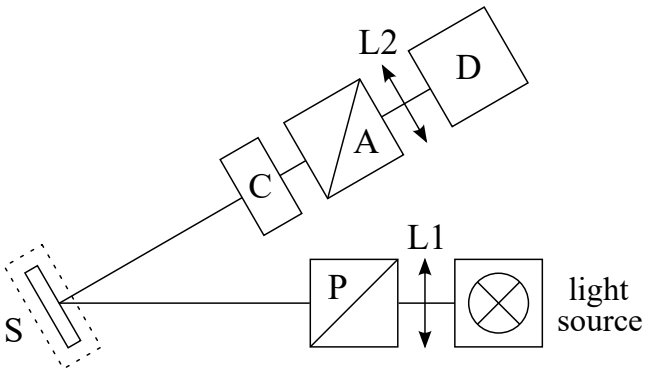

Figure 3.5: Schematic representation of magneto-optical Kerr spectrometer with rotating analyzer; A - rotating analyzer, C - compensator, D - detector, L1, L2 - lenses, P - polarizer, S - sample in magnetic field.

by eq. (3.15). Reflection upon sample S is now characterized by general form of Jones reflection matrix $\boldsymbol{R}_{sp}$ (2.10), as the sample becomes optically anisotropic in magnetic field. If we consider the case of almost normal light incidence, the reflection coefficients are related to each other according to eq. (2.35). Using then the definition of complex Kerr MO angle Φ_K (2.36) via reflection coefficients, general form of the Jones reflection matrix $\boldsymbol{R}_{sp}$ can be rewritten as

$$\boldsymbol{R}_{sp} = \begin{bmatrix} 1 & -\Phi_K \\ -\Phi_K & -1 \end{bmatrix}. \tag{3.23}$$

Compensator C is a phase retarder characterized by phase shift δ, its Jones transmission matrix $\boldsymbol{T}_C$ is therefore given by eq. (3.17). Rotating analyzer A transmits linearly polarized light in plane determined by angle ξ measured to x axis, its Jones transmission matrix $\boldsymbol{T}_A$ is then given by eq. (3.18). Relation between incident $\boldsymbol{J}^{(I)}$ and final $\boldsymbol{J}^{(X)}$ Jones vector can be expressed analogically to eq. (3.19), where the only difference is made by replacement of Jones reflection matrix by eq.(3.23). Therefore we can write

$$\begin{aligned} \boldsymbol{J}^{(X)} = \boldsymbol{T}_A \cdot \boldsymbol{T}_C \cdot \boldsymbol{R}_{sp} \cdot \boldsymbol{T}_P \cdot \boldsymbol{J}^{(I)} = \begin{bmatrix} \cos^2\xi & \cos\xi\sin\xi \\ \cos\xi\sin\xi & \sin^2\xi \end{bmatrix} \cdot \\ \cdot \begin{bmatrix} \mathrm{e}^{i\frac{\delta}{2}} & 0 \\ 0 & \mathrm{e}^{-i\frac{\delta}{2}} \end{bmatrix} \cdot \begin{bmatrix} 1 & -\Phi_K \\ -\Phi_K & -1 \end{bmatrix} \cdot \begin{bmatrix} \cos^2\alpha & \cos\alpha\sin\alpha \\ \cos\alpha\sin\alpha & \sin^2\alpha \end{bmatrix} \cdot \boldsymbol{J}^{(I)}. \end{aligned} \tag{3.24}$$

Let us now consider the polarizer P transmitting p-polarized light, i.e. $\alpha = 90°$ (cf. Fig. 2.2). Further we assume that the analyzer A is initially in crossed position with polarizer P, which means that angle ξ is now measured from the crossed position. In such case the final Jones vector is given as

$$\boldsymbol{J}^{(X)} = \begin{bmatrix} -\Phi_K \mathrm{e}^{i\frac{\delta}{2}}\cos^2\xi - \mathrm{e}^{-i\frac{\delta}{2}}\cos\xi\sin\xi \\ -\mathrm{e}^{-i\frac{\delta}{2}}\sin^2\xi - \Phi_K \mathrm{e}^{i\frac{\delta}{2}}\cos\xi\sin\xi \end{bmatrix}. \tag{3.25}$$

Intensity I measured by detector D is given by eq. (3.20). If we use Jones vector in the form (3.25), the intensity can be calculated as

$$I = \sin^2\xi + |\Phi_K|^2\cos^2\xi + \sin(2\xi)\mathrm{Re}\left\{\Phi_K \mathrm{e}^{i\delta}\right\}. \tag{3.26}$$

The quadratic term in Φ_K in eq. (3.26) can be neglected as a consequence of typically weak MOKE signal. Expressing further the complex Kerr MO angle Φ_K in terms of Kerr rotation θ_K and Kerr ellipticity ϵ_K according to eq. (2.36), the intensity can be rewritten as

$$I = \sin^2 \xi + (\theta_K \cos \delta + \epsilon_K \sin \delta) \sin (2\xi) + I_{\text{dark}}, \tag{3.27}$$

where I_{dark} is a constant term representing dark current in the detector.

From eq. (3.27) the MO angles can be calculated. We see that with no phase retarder in the experimental set-up ($\delta = 0$), Kerr rotation θ_K could be directly measured for known value of the analyzer angle ξ, if no dark current were present. However, the presence of dark current and other noise factors requires measuring of the intensity for several values of the angle ξ. Then the intensity can be fitted as a function of angle ξ and Kerr rotation θ_K is extracted as constant parameter for each wavelength. Looking at eq. (3.27), theoretically we could measure Kerr ellipticity ϵ_K directly as well, using phase retarder with phase shift $\delta = \pi/2$. However, no real phase retarder has constant phase shift in a broad spectral range. The phase retarder used in the system has known but varying phase shift ($0 < \delta < \pi/2$). The intensity is then again fitted as function of angle ξ according to eq.(3.27). Knowing for each wavelength the phase shift δ as well as the parameter of Kerr rotation θ_K extracted from previous measurement without phase retarder, now it is Kerr ellipticity ϵ_K being calculated from the fit.

3.6 Magneto-optical Kerr microscopy

MO Kerr microscopy is a technique for measuring magnetic properties with spatially resolved information, i.e. it allows observation of magnetic domains. The spatial information can be obtained either in a scanning regime or detected all at once with use of charge-coupled device (CCD) detector. It is typically used for recording of static images, but advanced techniques of time resolved Kerr microscopy have also been demonstrated [93].

Fig. 3.6 shows basic experimental set-up of MO Kerr microscope. Light coming out of the source passes through polarizer P, which makes the light wave linearly polarized. The light further passes through beam splitter BS, which ensures normal incidence on the sample surface. After being reflected on sample S placed in a magnetic field, the light passes through beam splitter BS and analyzer A and it is detected by detector D.

We can notice that the set-up of Kerr microscope is similar to MOKE spectrometer presented in previous section, however there are two apparent differences. First is the additional use of beam splitter, which ensures perfectly normal light incidence on sample surface. This prevents unwished image distortion, which would occur in configuration of almost normal light incidence as introduced in case of the spectrometer in Fig. 3.5. Second is the absence of compensator in sequence of the optical elements. As we already know from previous section, MOKE set-up with crossed polarizers and no compensator in the system allows us to directly measure Kerr rotation θ_K. In case of Kerr microscopy we are only interested in obtaining the spatial information, which can be provided by either Kerr rotation or Kerr ellipticity, knowledge of both quantities is now redundant.

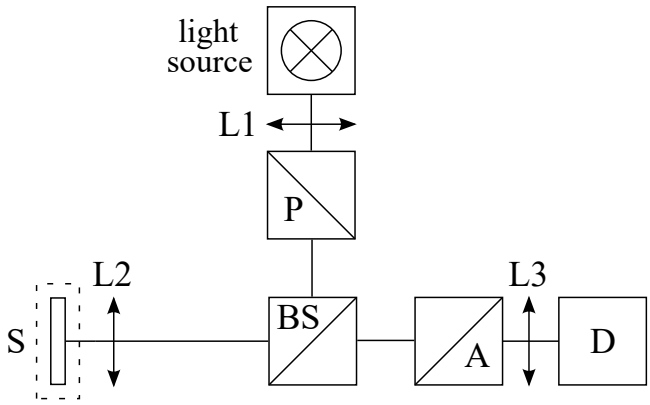

Figure 3.6: Basic experimental set-up of MO Kerr microscope; A - analyzer, BS - beam splitter, D - detector, L1, L2, L3 - lenses, P - polarizer, S - sample in magnetic field.

As measuring Kerr rotation is technically easier, the microscope is designed for this type of measurement with no additional phase retarding element in the system.

As the experimental set-up is analogical to that of MO spectrometer, the intensity arriving at the detector can be derived in terms of Jones calculus the same way as presented in previous section. Final expression of the intensity I measured by CCD detector is given by eq. (3.27), where $\delta = 0$ as there is no phase retarder in the system.

3.7 Magnetic force microscopy

Magnetic force microscopy (MFM) is a technique for measuring magnetic properties of materials, which enables direct visualisation of magnetic domains. Unlike Kerr microscopy it is not an optical technique, therefore its resolution is not limited by optical diffraction limit and it can be several orders of magnitude higher. The technique is akin to classical atomic force microscopy (AFM), which serves for surface topography measurements.

The principle of AFM is based on scanning with a sharp tip. When the tip is moved close above the surface, it is affected by intermolecular van der Waals forces. The forces result in bending of a cantilever, on which the tip is placed. Movement of the cantilever is further tracked by laser light, which allows to extract profile of the sample surface.

Fig. 3.7(a) shows commercial low temperature atomic force microscope attoAFM/MFM Ixs, which can perform measurements of both AFM and MFM. Magnetic information about the sample can be obtained in a way analogical to AFM via scanning movement of a sharp tip. The key difference is magnetic coating of the tip, which enables the tip to sense direction of magnetization in the sample. The intermolecular van der Waals forces are however still present and they are acting on the tip as well, therefore we need to isolate their effect in order to obtain pure information about magnetic properties of the sample. This can be done in two different ways. In lift mode, the topography is measured first by classical AFM when scanning a line in one direction. This is done close

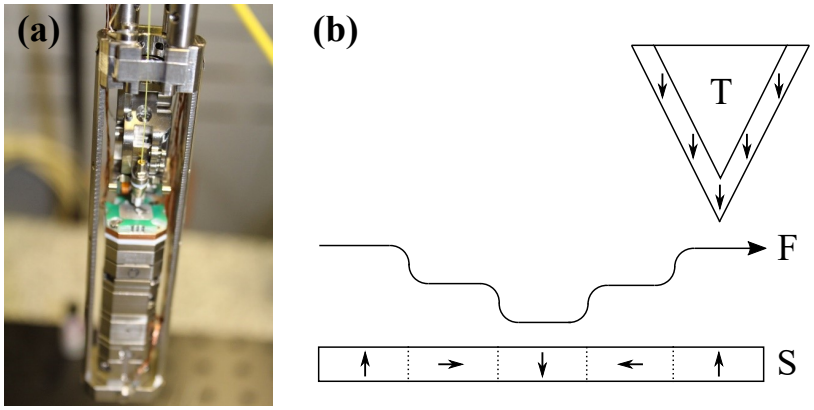

Figure 3.7: (a) Scanning probe of commercial low temperature atomic force microscope attoAFM/MFM Ixs (taken from [89]); C - piezoelectric crystals allowing movement of the scanner, S - sample. (b) Schematic representation of MFM scanning process; F - force acting on scanning tip above sample surface, S - sample, T - tip with magnetic coating. Arrows represent magnetization direction of the sample domains and tip coating.

enough to the surface, where the intermolecular forces are significantly stronger than the magnetic forces. Then for scanning the same line in opposite direction, the tip is lifted and kept at constant distance above the surface due to movement along the topography profile obtained during the first scan. This way the influence of topography is eliminated and the tip is affected only by magnetic forces. In constant height mode, we first determine overall tilt of sample surface in both in-plane directions. Then we adjust the scanner movement so that the tip is always scanning (in both directions) at a constant distance above the average surface plane. This distance is large enough so that the intermolecular forces are negligible. As the lift mode is in reality rather complicated, for samples which are reasonably flat and their tilt can be easily determined the constant height mode is a suitable option.

It is worth noting that MFM does not provide absolute, but only relative information about the magnetization direction in the sample. Fig. 3.7(b) shows schematic depiction of scanning movement of the tip T above surface of sample S. Arrows represent magnetization direction in the tip coating and in magnetic domains of the sample. Observing the resulting force F acting on the tip above the surface, we can see that we can clearly distinguish domains with magnetization parallel and antiparallel compared to the tip coating. These areas will appear with maximum contrast, i.e. black and white on a grey scale. However domains with magnetization perpendicular to the tip coating always affect the tip in exactly same way, therefore they cannot be distinguished even when having opposite direction to each other. Such areas will appear with the same grey contrast on the grey scale. Therefore we cannot obtain complete information about the magnetization direction in the sample, but we can clearly visualise individual magnetic domains.

4. Investigated samples

In this chapter we present technical details of the samples fabrication process and we provide their brief overview. All the samples were fabricated at Centre for Nanoscience and Nanotechnology in Orsay.

4.1 $La_{2/3}Sr_{1/3}MnO_3$ films on various oxide substrates

In order to impose static epitaxial strain on LSMO, we fabricated set of thin films on various oxide materials. The films were grown using a homemade PLD set-up with KrF ultraviolet laser operating at wavelength $\lambda = 248$ nm. Pulse repetition rate was 2 Hz and maximum energy fluence 3 J/cm^2. Background oxygen pressure was 120 mTorr during the deposition process, post-deposition oxygen annealing was performed at 75 Torr. The substrate temperature was maintained at 620 °C.

We used four different substrate materials, either (001) oriented cubic (LAO, LSAT and STO) or (110) oriented orthorhombic (DSO) single crystals. They are all twinfree with exception of LAO, which exhibits microtwins parallel to (001). These substrates provide different type and range of in-plane induced epitaxial strains, from large compressive strain on LAO, through small compressive strain on LSAT and small tensile strain on STO, up to large tensile strain on DSO. Fig. 4.1 illustrates number line with indicated values of bulk cubic or pseudocubic lattice parameters of all four substrates together with LSMO.

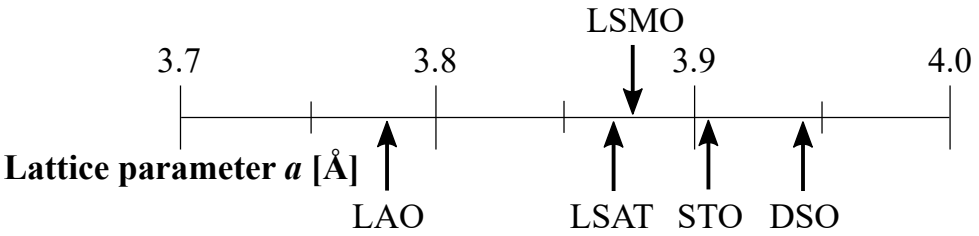

Figure 4.1: Schematic representation of number line with bulk cubic or pseudocubic lattice parameters of all substrates used for deposition of LSMO films.

Pseudocubic lattice parameter of bulk LSMO is $a_{LSMO} = 3.876$ Å [94], the substrates are characterized by cubic or pseudocubic lattice parameters $a_{LAO} = 3.790$ Å, $a_{LSAT} = 3.868$ Å, $a_{STO} = 3.905$ Å and $a_{DSO} = 3.942$ Å. Corresponding lattice mismatch can thus be calculated using eq. (1.2), it is listed for all substrates in Table 4.1.

Material	LAO	LSAT	LSMO	STO	DSO
Lattice parameter a [Å]	3.790	3.868	3.876	3.905	3.942
Lattice mismatch m [%]	2.27	0.21		-0.74	-1.67

Table 4.1: Summary of bulk lattice parameters a and lattice mismatches m for all substrates used for deposition of LSMO films.

We grew set of four LSMO films, one on each type of substrate, all with the same nominal thicknesses of 20 nm. Growth of LSMO on (001) oriented cubic or (110) oriented orthorhombic substrates results in single-crystalline LSMO films with (110) monoclinic unit cell, which can be described as (001) pseudocubic as well. Detailed description of the crystallographic properties will be provided in the following chapter.

4.2 Patterned $La_{2/3}Sr_{1/3}MnO_3$ on piezoelectric underlayer

In order to dynamically control the strain imposed on LSMO, we fabricated a device of patterned LSMO on piezoelectric underlayer. The initial multilayer was grown by PLD and further processed by means of optical lithography, ion beam etching (IBE) and DC sputtering.

The device is schematically depicted in Fig. 4.2. The initial multilayer structure consists of STO substrate, on top of which we subsequently grew 30 nm of SRO bottom electrode, 130 nm of $PbZr_{0.52}Ti_{0.48}O_3$ (PZT) piezoelectric layer and finally 20 nm of LSMO on top. The SRO and LSMO layers were deposited using same deposition parameters as described in previous section. The PZT layer required different conditions, we used nitrous oxide as background gas and higher repetition rate of 10 Hz. Rest of the parameters remained the same.

Combination of optical lithography, IBE and DC sputtering were used to pattern the LSMO film on top and fabricate contacts to both top and bottom electrodes. In order to provide sufficiently large area for investigation by optical and MO methods, 300×300 μm^2 large LSMO pads were fabricated. The bottom SRO electrode was accessed by further etching through the PZT layer and contacted by Ti/Au via DC sputtering. The top LSMO electrode was contacted by Ti/Au as well, using an auxiliary deposition of insulating Si_3N_4 next to the LSMO pads

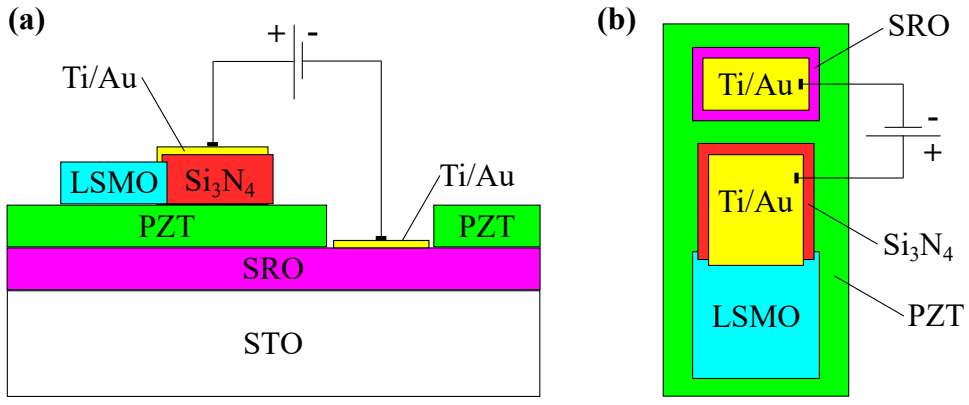

Figure 4.2: (a) Schematic cross section and (b) top view of device used for dynamic application of strain to LSMO; 300×300 μm^2 LSMO pads were fabricated on top of piezoelectric PZT layer. The voltage was applied in direction perpendicular to sample surface via top (LSMO) and bottom (SRO) electrodes contacted by Ti/Au. Additional Si_3N_4 pads allow to keep the LSMO pads accessible for further measurements via optical methods.

(as shown in Fig. 4.2), while keeping the LSMO pads uncovered and susceptible to subsequent optical and MO characterization. This approach also allows to limit problem of leakage current. When applying voltage between the top and bottom electrodes, the PZT layer is electrically polarized in direction perpendicular to sample surface. The whole sample area consists of array of 20 identical LSMO pads and 4 contacts to the bottom electrode, so that malfunctioning due to pattern processing errors and films inhomogeneities can be avoided choosing properly working device components.

4.3 $SrRuO_3$ films on $SrTiO_3$ substrates

Growth of SRO on the most commonly used substrate of (001) oriented STO is possible in six different crystallographic orientations, so called variants [19, 20], as shown in Fig. 4.3(a). They can be sorted into three pairs - X (X'), Y (Y') and

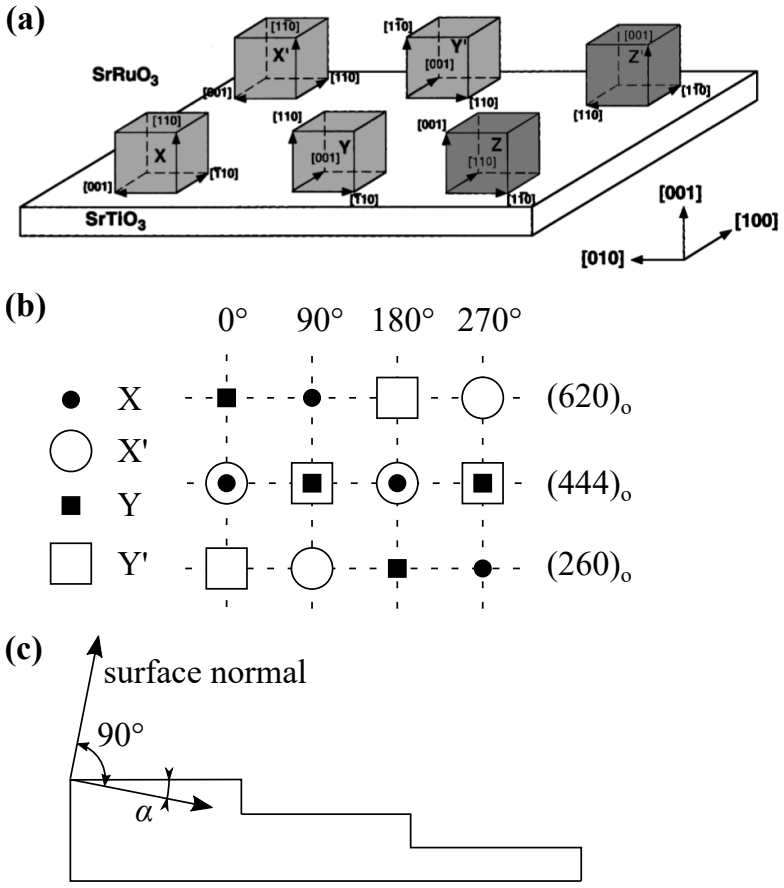

Figure 4.3: (a) Schematic representation of six different crystallographic variants of SRO growing on (001) oriented STO substrate (taken from [19]). Note that the SRO variants are represented as pseudocubic unit cells, while the crystallographic directions are given for orthorhombic structure. (b) Schematic illustration of $(260)_o$, $(444)_o$ and $(620)_o$ Bragg reflections in RSMs measured on multivariant SRO film with X (X') and Y (Y') variants, around four azimuth angles $\varphi = 0°, 90°, 180°$ and 270°. (c) Schematic cross section of vicinal substrate with definition of the miscut angle α.

Z (Z'). By means of conventional XRD, we can distinguish among variants from these three pairs, but we cannot distinguish between the two variants in one pair, unless they are both present in the film. It is illustrated in Fig. 4.3(b), which shows schematic representation of RSMs measured around four values of the azimuth angle $\varphi = 0°, 90°, 180°$ and 270°. Here the relative positions of $(260)_o$, $(444)_o$ and $(620)_o$ Bragg reflections are indicated at each azimuth, when four variants from two pairs X (X') and Y (Y') are present in the SRO film. We can see, for example, that if only X and Y variants were present, this situation would appear the same as presence of only X' and Y' variants. The resulting pattern of Bragg reflections would be a mirror image of one another, but as we have no fixed point, we cannot determine which one would be which. The important information that can be determined, however, is the lone presence or absence of multiple crystallographic variants.

It has been demonstrated [95, 19, 20] that use of vicinal STO substrate leads to supression of formation of several different SRO variants during the deposition and therefore to improvement of overall crystalline quality of the films. Vicinal substrate is characterized by small deviation of its surface normal from one of the major crystallographic axes. This deviation is known as miscut and it is quantified by miscut angle α, as shown in Fig. 4.3(c). Even very small miscut angle ($\alpha < 1°$) was demostrated to suppress formation of the Z (Z') variants growth [95], leading to presence of only X (X') and Y (Y') variants in the films. Larger values of the miscut angle ($\alpha \gtrsim 1°$) can then allow growth of purely single-variant SRO films with only one crystallographic orientation.

Presence of multiple crystallographic variants, related to crystalline quality of the material, naturally influences its magnetic properties, such as magnetocrystalline anisotropy or parameters of the magnetization reversal process [96]. In order to investigate influence of the crystalline quality on magnetization dynamics in SRO films, we fabricated a set of two SRO films on (001) oriented STO substrates with different values of the miscut angle. We deposited one film on substrate of low miscut angle $\alpha = 0.1°$ to achieve multivariant growth. In contrary, to suppress the multivariant growth we used vicinal substrate with $\alpha = 1°$ for the second sample. Both films were deposited by means of PLD, under same experimental conditions as described in section 4.1. We denote the sample on vicinal substrate SRO1, the sample on low miscut substrate SRO2.

5. Strain impact on electronic structure of $La_{2/3}Sr_{1/3}MnO_3$

The fifth chapter presents all the results achieved during investigation of the LSMO samples, whose physical properties were tried to be influenced by both static and dynamic strain.

5.1 Static application of strain

The first part of this chapter covers in detail the investigation process for LSMO samples deposited on different substrates, i.e. having different values of static epitaxial strain. We begin with basic structural characterization by XRD, and morphological study by AFM, which give us basic estimate of the samples quality. The strain state is evaluated more in detail by advanced XRD measurements - reciprocal space maps. Magnetic properties of the samples are determined by SQUID magnetometry. Full tensor of permittivity is determined by combination of spectroscopic ellipsomentry and MO Kerr spectroscopy. Some transitions in the MOKE spectra exhibit dependence on the epitaxial strain, which is further interpreted with the help of *ab initio* calculations. These findings belong to main conclusions of this work.

5.1.1 Basic structural characterization and morphology

Proper crystallinity and surface morphology of the LSMO films was verified by means of XRD and AFM. The XRD measurements were carried out using PANanalytical X'Pert PRO Diffractometer. The AFM images were taken by Veeco/Bruker diInnova AFM Microscope.

Crystallinity of the samples was investigated by symmetric $\theta-2\theta$ scans around (002) Bragg reflection of LSMO. In order to estimate the film thickness and pseudocubic out-of-plane lattice parameter, the diffracted intensity I was fitted by classical interference formula

$$I = I_0 \left[\frac{\sin(\frac{2\pi}{\lambda} t \sin\theta)}{\sin(\frac{2\pi}{\lambda} c_c \sin\theta)} \right]^2, \tag{5.1}$$

where $\lambda = 1.5406$ Å is the X-ray wavelength, t is the film thickness, c_c is the out-of-plane lattice parameter, θ is the Bragg diffraction angle and I_0 is a constant. As shown later this approach reproduces the thickness fringes but neglects interference with substrate peak (so called kinematic approximation). Root mean square (RMS) roughness R_{RMS} was evaluated from the AFM images by Gwyddion software [97]. All the extracted parameters of the investigated films are summarized at the end of this section in Table 5.1.

Fig. 5.1 shows surface AFM images of all four substrates before the LSMO deposition. Presence of micro twins in LAO (Fig. 5.1(a)) is clearly visible and it results in the highest surface roughness among all substrates, $R_{LAO} = 0.71$ nm. LSAT (Fig. 5.1(b)) on the other hand exhibits remarkably flat surface as a result

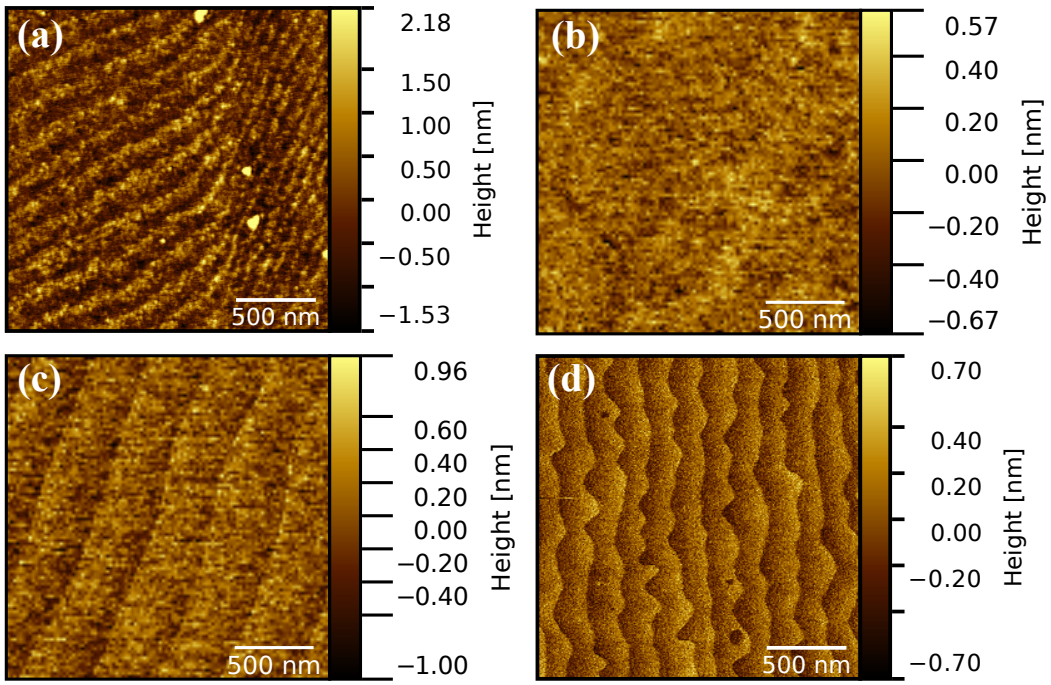

Figure 5.1: 2×2 μm^2 AFM images of (a) LAO, (b) LSAT, (c) STO and (d) DSO substrates. Micro twins are visible in LAO. Atomic steps can be clearly seen in all substrates except for LSAT.

of high crystalline quality and low miscut angle, $R_{LSAT} = 0.19$ nm. Presence of atomic steps can be seen in STO (Fig. 5.1(c)), resulting in $R_{STO} = 0.38$ nm. The last substrate of DSO (Fig. 5.1(d)) exhibits very smooth atomic steps and the lowest surface roughness, $R_{DSO} = 0.11$ nm.

Fig. 5.2(a) shows $\theta - 2\theta$ scan of LSMO/LAO sample. The measured intensity is fitted by formula (5.1), which yields the film thickness $t = 20.0$ nm and pseudocubic out-of-plane lattice parameter $c_c = 4.002$ Å. The substrate peak clearly exhibits multiple maxima corresponding to different crystallographic twins (see

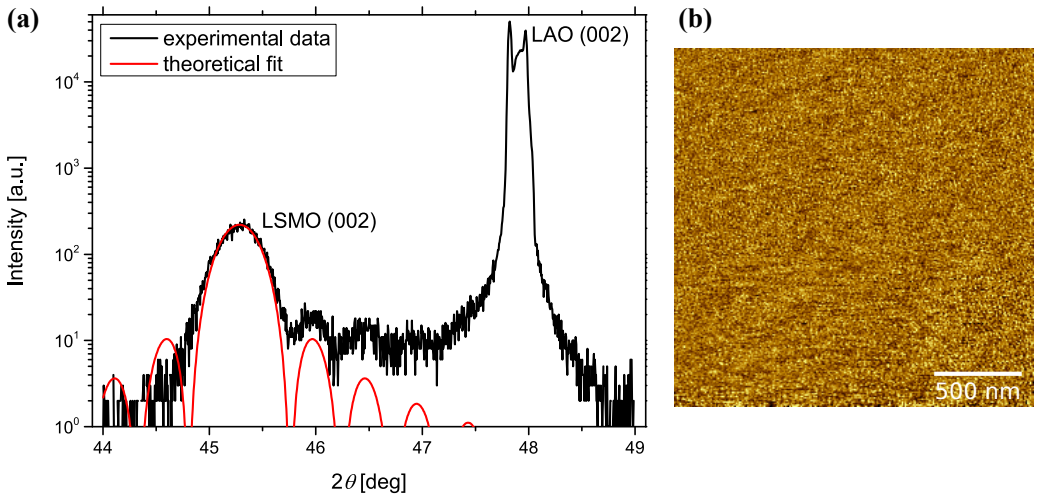

Figure 5.2: (a) Symmetric θ−2θ XRD scan and (b) surface AFM image (2×2 μm^2) of LSMO film deposited on LAO substrate.

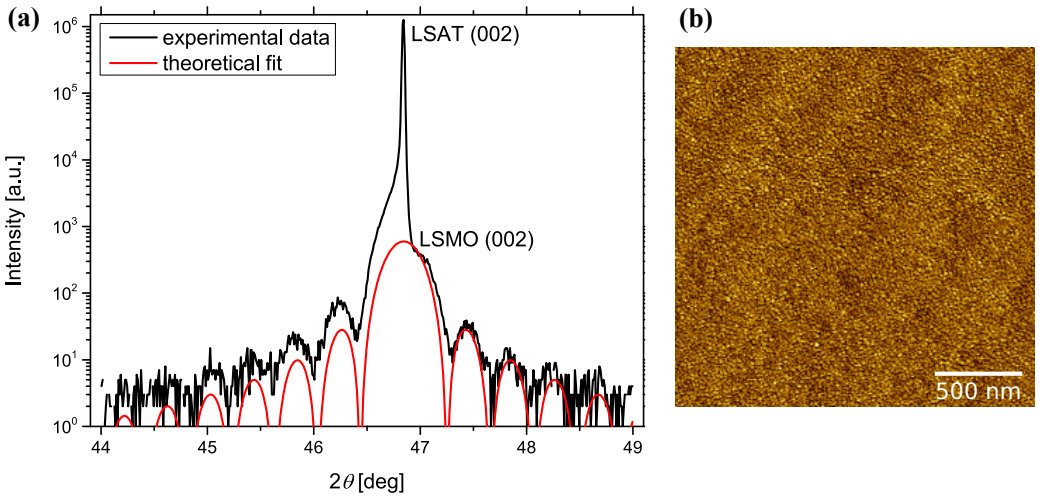

Figure 5.3: (a) Symmetric $\theta-2\theta$ XRD scan and (b) surface AFM image (2×2 μm^2) of LSMO film deposited on LSAT substrate.

Fig. 5.1(a)). Due to the lower crystalline quality of the substrate and the high lattice mismatch (2.27 %) the resulting quality of deposited LSMO layer is lower compared to other films in the set, as can be seen from smaller overall intensity of the LSMO (002) peak as well as from low visibility of the interference fringes. The surface roughness is also the highest among all the samples, $R_{RMS} = 1.3$ nm. Fig. 5.2(b) shows AFM image of the surface, where no signature of atomic steps can be recognized anymore (cf. Fig 5.1(a)).

Fig. 5.3(b) shows $\theta - 2\theta$ scan of LSMO/LSAT sample. The fit according to eq. (5.1) gives film thickness $t = 23.6$ nm and lattice parameter $c_c = 3.876$ Å. Due to high crystalline quality of the nearly lattice matched (0.21 % mismatch) substrate the resulting LSMO film is of high quality. The interference fringes are well visible and the film is atomically flat with surface roughness $R_{RMS} = 0.29$ nm. Fig. 5.3(b) shows AFM image of the surface with no clear signature of the atomic steps, similarly as in case of the bare substrate (see Fig. 5.1(b)).

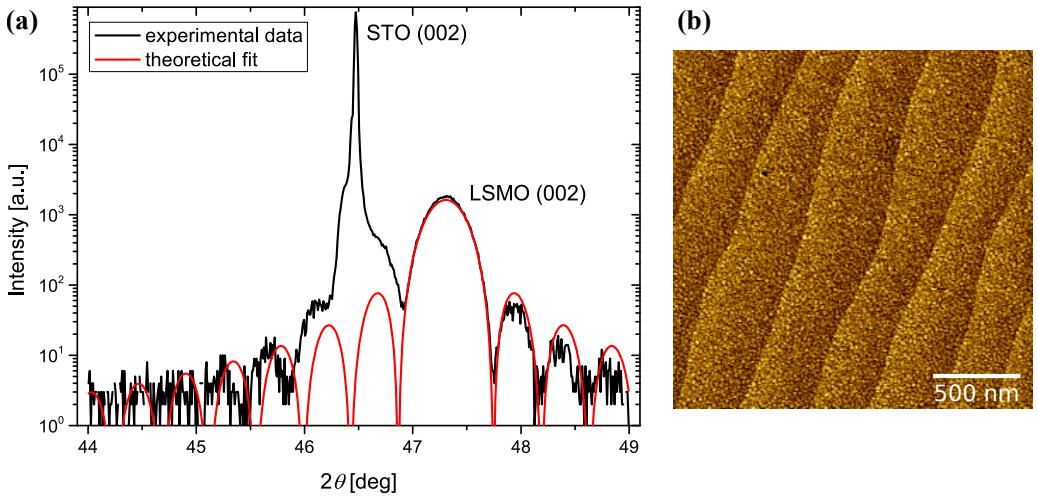

Figure 5.4: (a) Symmetric $\theta-2\theta$ XRD scan and (b) surface AFM image (2×2 μm^2) of LSMO film deposited on STO substrate.

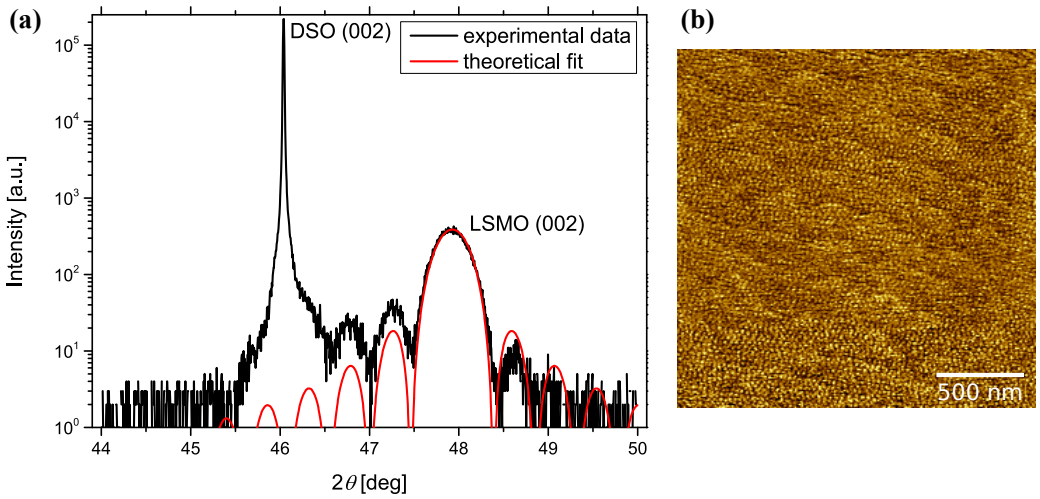

Figure 5.5: (a) Symmetric $\theta-2\theta$ XRD scan and (b) surface AFM image (2×2 μm^2) of LSMO film deposited on DSO substrate.

Fig. 5.4(a) shows $\theta - 2\theta$ scan of the LSMO/STO sample. The fit according to eq. (5.1) gives film thickness $t = 21.9$ nm and lattice parameter $c_c = 3.840$ Å. We can clearly see that the fitted interference fringes are slightly shifted with respect to the experimental curve, especially for values of 2θ smaller than the Bragg peak. This demonstrates limitations of the kinematic approximation, i.e. formula (5.1), and it shows that dynamic theory [98] is needed for more precise description of the experimental data. More complex calculation including interference of both the film-diffracted and the substrate-diffracted beam is described elsewhere [99] for the case of LSMO on STO substrate. It shows excellent agreement with the experimental data and therefore improved precision of the fitted parameters. Fig. 5.4(b) shows AFM image of the smooth film surface with $R_{RSM} = 0.30$ nm, revealing clearly the atomic steps (cf. Fig. 5.1(c)). High quality of the STO substrate and low lattice mismatch (-0.74 %) results in high quality of the deposited film.

Fig. 5.5(a) shows $\theta - 2\theta$ of the LSMO/DSO sample. The fit according to eq. (5.1) gives film thickness $t = 20.9$ nm and lattice parameter $c_c = 3.793$ Å. Large lattice mismatch (-1.67 %) again results in lower quality of the deposited film, which can be seen in less pronounced visibility of the interference fringes. The clear atomic steps of the substrate (see Fig. 5.1(d)) are almost invisible in the

Substrate	m [%]	t [nm]	c_c [Å]	R_{RMS} [nm]	c_c/a_c
LAO	2.27	20.0	4.002	1.3	1.056
LSAT	0.21	23.6	3.876	0.29	1.002
STO	-0.74	21.9	3.840	0.30	0.983
DSO	-1.67	20.9	3.793	0.51	0.962

Table 5.1: Structural parameters of LSMO films grown on four different substrates. We list lattice mismatch m, film thickness t, pseudocubic out-of-plane lattice parameter c_c, surface roughness R_{RMS} and c_c/a_c ratio evaluated while assuming that the films are fully strained, i.e. the in-plane lattice parameter a_c of the film corresponds to bulk lattice parameter of the substrate.

surface morphology of the film, as demonstrated in Fig. 5.5(b). The surface roughness however remains relativly low, $R_{RMS} = 0.51$ nm. The structural parameters of all four LSMO films are summarized in Table 5.1.

5.1.2 Strain state determination by reciprocal space maps

Measurement of a proper set of reciprocal space maps allows us to describe the whole unit cell of investigated thin film, as shown previously in section 3.2. This knowledge also provides information about strain state of the film. In order to determine strain states of our samples, we measured RSMs around the (260), (444), (620) and (44-4) Bragg reflections for each sample. The measurements were carried out using the same equipment as for the symmetric $\theta - 2\theta$ scans presented in previous section, PANanalytical X'Pert PRO Diffractometer. The RSMs for all samples are shown in Figs. 5.6-5.9. The out-of-plane component of reciprocal space vector $Q_\perp$ is given as $Q_\perp = \frac{1}{\lambda}[\sin(2\theta - \omega) + \sin(\omega)]$, where θ is the Bragg diffraction angle, ω is one of the sample rotation angles and $\lambda = 1.5406$ Å. The RSMs revealed fully strained films on all four substrates and allowed us via formulae derived in section 3.2 to completely describe the unit cell of all the LSMO films. The extracted lattice parameters are summarized in Table 5.2 and plotted in Fig. 5.10 as a function of the epitaxial strain.

Fig. 5.6 shows the RSMs of LSMO deposited on cubic LAO substrate. Four RSMs around (260), (444), (620) and (44-4) Bragg reflections of the LSMO were

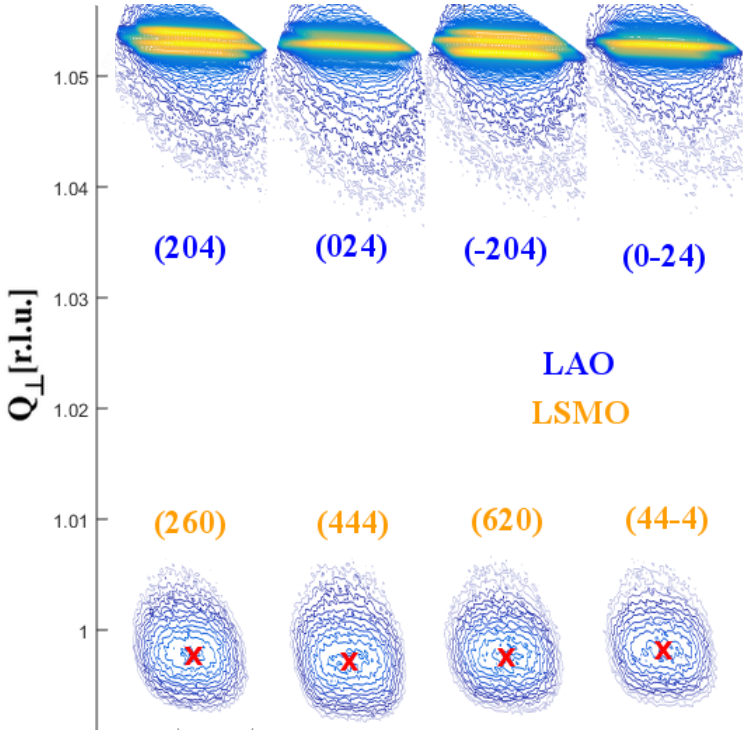

Figure 5.6: RSMs around (260), (444), (620) and (44-4) Bragg reflections of LSMO on cubic LAO substrate, which provides large compressive strain. LSMO peak positions are indicated by red crosses. Colour scale of the diffracted intesity is logarithmic.

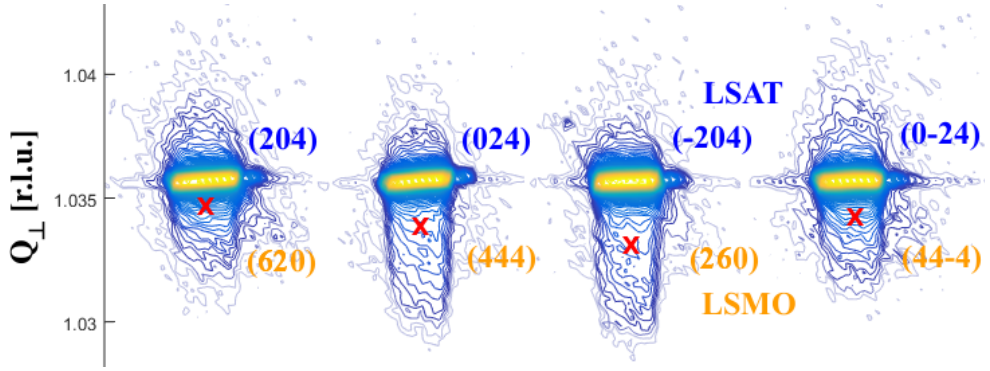

Figure 5.7: RSMs around (260), (444), (620) and (44-4) Bragg reflections of LSMO on cubic LSAT substrate, which provides small compressive strain. LSMO peak positions are indicated by red crosses.

measured for four values of the azimuth angle, $\varphi = 0°, 90°, 180°$ and 270°, respectively. The substrate peaks, especially for (204) and (-204) Bragg reflexion, clearly exhibit multiple maxima, as expected in presence of several crystallographic twins. The same lateral position of layer peak and substrate peak, which is well visible in all four RSMs, indicates fully strained LSMO with no relaxation. The LAO substrate is cubic, all the RSMs are therefore aligned to have the same $Q_\perp$ coordinate of the substrate peak. The $Q_\perp$ coordinate of the LSMO peak varies only a little for different azimuths, which justifies possible pseudocubic description of the LSMO unit cell. However we do not use it and as introduced in section 1.3 we describe the unit cell rigorously as monoclinic in further analysis. We can also note that the substrate peaks are elongated in horizontal direction, which is related to low resolution settings of the XRD experiment that were chosen in order to enhance visibility of the weak LSMO peaks.

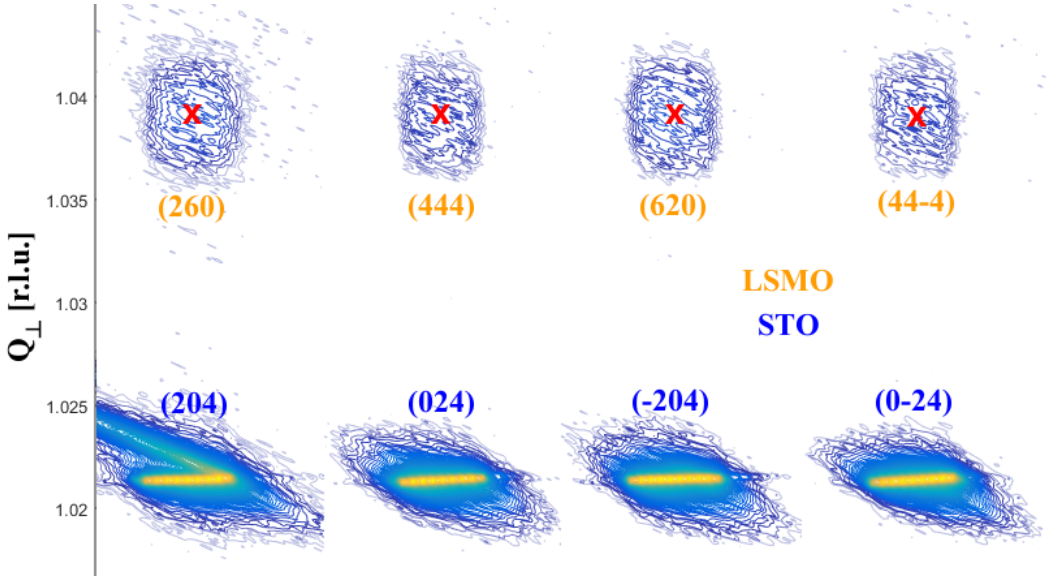

Figure 5.8: RSMs around (260), (444), (620) and (44-4) Bragg reflections of LSMO on cubic STO substrate, which provides small tensile strain. LSMO peak positions are indicated by red crosses.

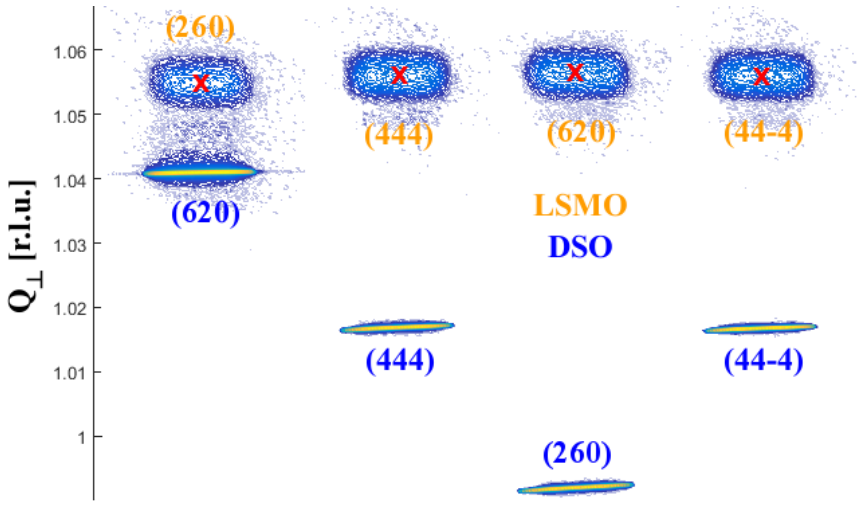

Figure 5.9: RSMs around (260), (444), (620) and (44-4) Bragg reflections of LSMO on orthorhombic DSO substrate, which provides large tensile strain. LSMO peak positions are indicated by red crosses.

Fig. 5.7 shows the RSMs of LSMO deposited on cubic LSAT substrate, measured for four azimuths analogically to the previous sample. Due to the very small compressive strain (0.21 % mismatch), the LSMO peak is partially merged with the substrate peak, similarly to the preliminary $\theta-2\theta$ scan (see. Fig 5.3(a)). Precise position of the peaks was determined using MATLAB software, which was also used to create the RSM plots. Same lateral position of substrate and layer peaks indicates once again fully strained films.

Fig. 5.8 shows the RSMs of LSMO deposited on cubic STO substrate, measured analogically to previous samples. The LSMO peaks are now displayed above the substrate peaks, with larger $Q_\perp$ values, corresponding to smaller out-of-plane lattice parameters resulting from the tensile strain.

Fig. 5.9 shows the RSMs of LSMO deposited on orthorhombic DSO substrate, in four azimuths analogically to previous samples. As for all investigated samples, the LSMO is clearly fully strained. The $Q_\perp$ values of substrate peak vary due to the orthorhombic structure of the substrate.

Lattice parameters extracted from the RSMs are summarized in Table 5.2 and Fig. 5.10. General behaviour of the lattice parameters with strain is in agreement with previously published structural investigations of thin LSMO layers [23]. Distance $(ab) = \sqrt{a_m^2 + b_m^2 - 2a_m b_m \cos\gamma_m}$ represents lateral periodicity in the $[1-10]_m$ monoclinic direction. In Table 5.2 we can see that values of the ab distance and c_m lattice parameter are almost identical for all samples, confirm-

Substrate	a_m [Å]	b_m [Å]	c_m [Å]	ab [Å]	γ_m [deg]
LAO	5.510	5.512	7.582	7.581	86.92
LSAT	5.475	5.481	7.743	7.743	89.94
STO	5.474	5.475	7.807	7.808	90.97
DSO	5.474	5.475	7.891	7.890	92.24

Table 5.2: Lattice parameters of LSMO films grown on four different substrates. Calculated from RSMs measured by XRD.

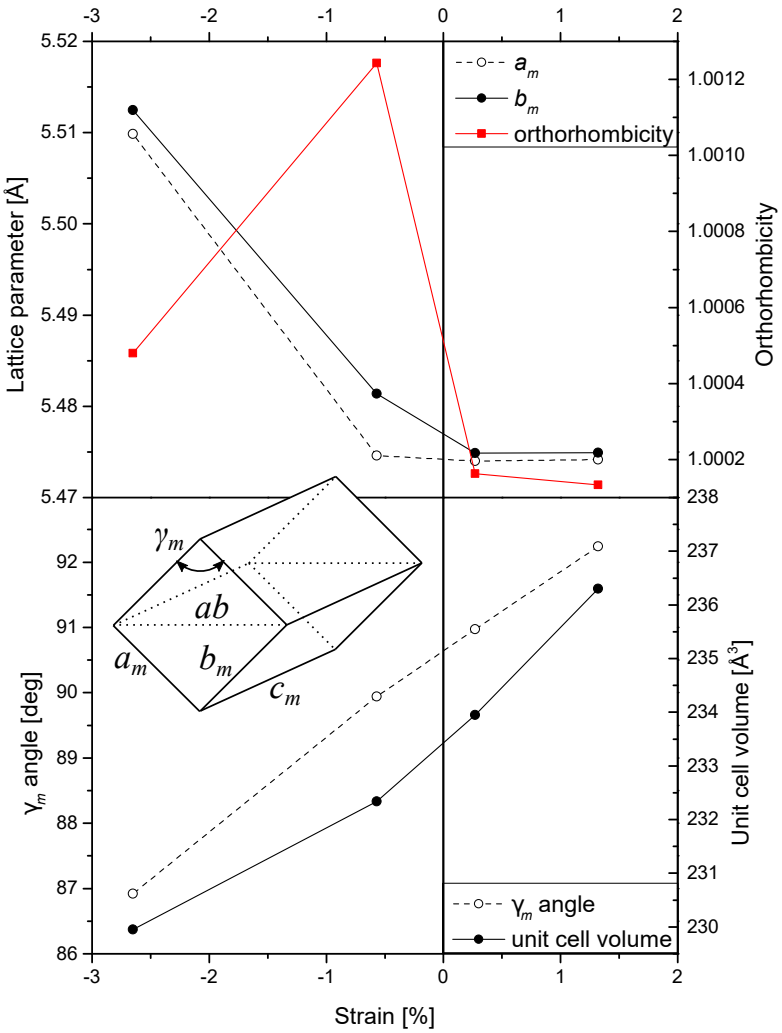

Figure 5.10: Structural parameters of LSMO films as functions of epitaxial strain along $[1\text{-}10]_m$ direction: a_m and b_m lattice parameters and orthorhombicity defined as b_m/a_m (top panel), γ_m angle and unit cell volume (bottom panel). Lines represent guides to the eye. The inset shows monoclinic unit cell, in which the lattice parameters are defined. The in-plane strain along $[1\text{-}10]_m$ direction was calculated from bulk value of LSMO ab distance $(ab)_{bulk} = 7.787$ Å [23] and measured ab values in Tab. 5.2 as $(ab - (ab)_{bulk})/(ab)_{bulk}$.

ing that the LSMO is coherently strained in both monoclinic in-plane directions $[1\text{-}10]_m$ and $[001]_m$. Figure 5.10 shows the a_m and b_m lattice parameters together with so called orthorhombicity factor defined as a ratio b_m/a_m. In agreement with Vailionis *et al.* [23] we observe that films under compressive strain exhibit unit cell with $a_m < b_m$ and $\gamma_m < 90°$, while in films under tensile strain $a_m = b_m$ and $\gamma_m > 90°$. In the $[001]_m$ in-plane direction, both the compressive and tensile strain are accommodated by change of the c_m lattice parameter, that is strained accordingly to the respective substrate. In the $[1\text{-}10]_m$ direction, the orthorhombicity value, that is very close to unity for samples grown on STO and DSO, shows that accommodation of the tensile strain is reached only by increment of the γ_m angle. On the other hand, the compressive strain accommodates by both the decrease of the γ_m angle and by relative change of the a_m and b_m lattice param-

eters, which can be also seen as increment of the orthorhombicity. However the orthorhombicity does not change proportionaly to the strain in contrast to the γ_m angle and unit cell volume, which both increase almost linearly from the largest compressive to the largest tensile strain.

As the epitaxial strain changes crystal structure of LSMO, it also consequently changes the OOR pattern. It can be shown [23] that such distinction of structural properties of films grown under compressive and tensile strain, as described in this section and shown in Fig. 5.10, leads to different OOR behaviour. LSMO films under compressive strain can be described by tilt system #9 ($a^+a^-c^-$), while under tensile strain the OOR corresponds to tilt system #18 ($a^+a^-c^0$). Both systems include in phase rotations around the $[100]_c$ pseudocubic axis and out of phase rotations around the $[010]_c$ pseudocubic axis. Difference arises from the in-plane elongation under tensile strain. It results in suppression of rotations around the $[001]_c$ pseudocubic axis, that are initially present in both bulk LSMO and films under compressive strain.

5.1.3 Magnetic characterization

Magnetic properties of the samples were investigated by means of SQUID magnetometry. The LAO, LSAT and STO substrates are diamagnetic. Magnetic moment of LSMO films deposited on these substrates can be easily measured by purely magnetic methods, such as SQUID, as the magnetic signal of the substrate is significantly lower than that of the LSMO film and the resulting signal can be corrected to the substrate diamagnetic contribution. However the DSO substrate is paramagnetic with strong magnetic anisotropy [100], which makes characterization of magnetic properties of films grown upon its surface by purely magnetic methods nearly impossible. That is why we infer for magnetic properties of the LSMO film on DSO indirectly from results of MOKE spectroscopy presented in one of the following sections 5.1.5.

Fig. 5.11(a) shows temperature dependence of magnetic moment of LSMO on LAO measured by SQUID. The sample was first demagnetized at 10 K with oscillating field and then the magnetic moment was measured at magnetic field of 20 mT applied parallel to the $[110]_{LAO}$ in-plane direction while heating the sample up to 370 K. The results are in agreement with previously published investigations of magnetic properties of thin LSMO layers [50]. Tsui *et al.* [50] investigated 25 nm thick LSMO grown on (001) oriented LAO substrate, which showed almost identical temperature dependence of magnetization. The striking feature occurs around 200 K. This peak is associated with spin reorientation transition, at which the magnetic anisotropy of the sample is changed. The in-plane anisotropy, which is typical for LSMO, changes into out-of-plane anisotropy below the temperature of 200 K. This behaviour is demonstrated in Fig. 5.11(b) which shows hysteresis loops of magnetization measured along the $[110]_{LAO}$ direction at 10 K and 300 K. The low temperature hysteresis loop apparently saturates at higher value of the applied magnetic field than the room temperature loop, which is nearly squared and saturates around 0.5 T.

Curie temperature and magnetic moment in saturation at low temperatures are $T_C \sim 370$ K [2] and $M_S \sim 3.7\,\mu_B$/Mn [101] in case of bulk LSMO. From Fig. 5.11(a) we determined $T_C \sim 308$ K for the sample deposited on LAO and

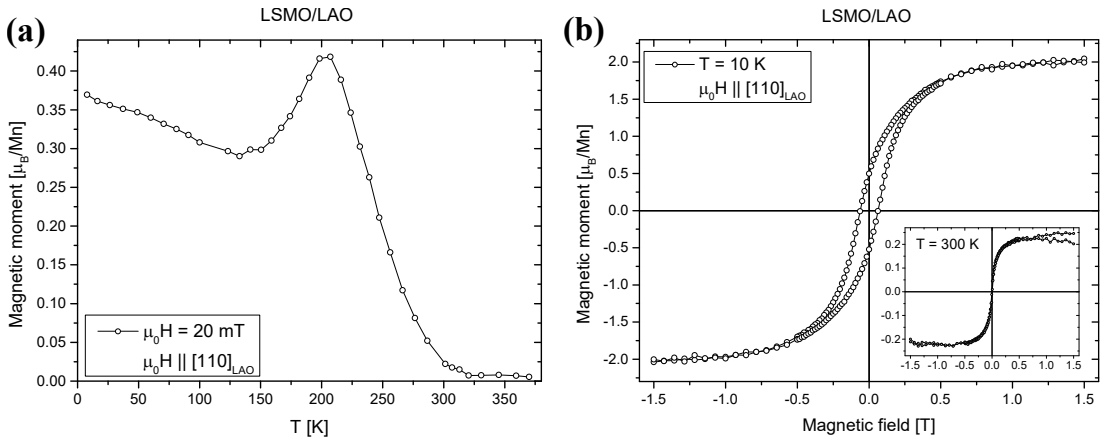

Figure 5.11: SQUID magnetometry results of the LSMO film deposited on LAO substrate. All data are corrected to the LAO diamagnetic contribution. (a) Temperature dependence of magnetic moment measured at magnetic field of 20 mT applied along the $[110]_{LAO}$ direction, measured from low temperatures while heating the sample. (b) Low temperature hysteresis loop along $[110]_{LAO}$ direction. The inset shows room temperature hysteresis loop along the same direction.

from Fig. 5.11(b) we get the low temperature magnetic moment $M_S \sim 2.0\mu_B$/Mn. The observed suppression of ferromagnetic ordering in this sample is caused by the large value of lattice mismatch and therefore large epitaxial strain. Two mechanisms are responsible for this behaviour. First, the strain leads to distortion of the LSMO unit cell, which increasingly deviates from the bulk structure with optimized magnetic properties. Second, it has been previously shown that at the LSMO/substrate interface the DE interaction is suppressed as a result of preferential orbital ordering under epitaxial strain. This consequently leads to antiferromagnetic ordering near the interface, which is known as magnetically inert layer [39, 45, 46]. Combination of these effects further results in T_C decrease and lower magnetic moment of the film.

Fig. 5.12(a) shows temperature dependence of magnetic moment of LSMO on LSAT. The measurement was carried out at magnetic field of 0.2 T applied parallel to the $[100]_{LSAT}$ in-plane direction while heating the sample from 10 K to 370 K. The easy axis of magnetization was reported [50] in-plane, approximately 20° from $[100]_{LSAT}$ direction towards the $[110]_{LSAT}$ direction at high temperatures. This angle changes to 30° below $\sim$ 50 K. From Fig. 5.12(a) we determined T_C of the sample on LSAT as $T_C \sim 361$ K, which is very close to the bulk value of 370 K. It demonstrates high quality of the LSMO film on LSAT substrate, which corresponds to the smallest lattice mismatch among substrates used in this study.

Fig. 5.12(b) shows hysteresis loops of magnetization measured along the in-plane $[100]_{LSAT}$ direction at 10 K and 300 K. They confirm the slight deviation of magnetization easy axis at low temperatures, as the loop at 10 K is almost nearly squared, while the room temperature loop is apparently perfectly squared. From the loop at 10 K we also determined the low temperature magnetic moment in saturation $M_S \sim 3.7\,\mu_B$/Mn, which is basically the same value as that of bulk LSMO, confirming high quality of the films prepared on the nearly lattice matched LSAT substrate.

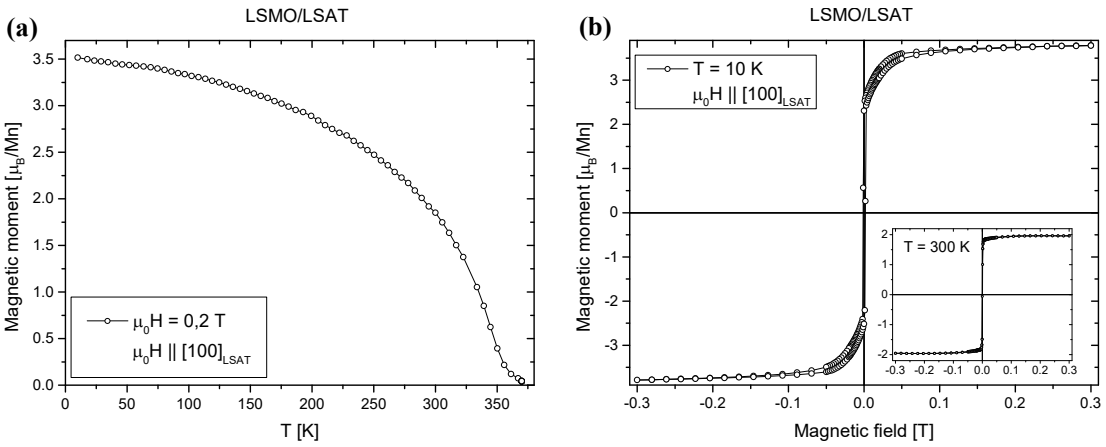

Figure 5.12: SQUID magnetometry results of the LSMO film deposited on LSAT substrate. All data are corrected to the LSAT diamagnetic contribution. (a) Temperature dependence of magnetic moment measured at magnetic field of 0.2 T applied along $[100]_{LSAT}$ direction, measured from low temperatures while heating the sample. (b) Low temperature hysteresis loop along $[100]_{LSAT}$ direction. The inset shows room temperature hysteresis loop along the same direction.

Fig. 5.13(a) shows temperature dependence of magnetic moment of LSMO on STO. The measurement was carried out at 0.2 T applied along the $[100]_{STO}$ in-plane direction while heating the sample from 10 K to 370 K. For this substrate, both $[100]_{STO}$ and $[110]_{STO}$ in-plane directions are equivalent easy axes of magnetization between T_C and 250 K, while at low temperatures the $[110]_{STO}$ direction becomes magnetically easier [50, 21]. This behaviour is in agreement with hysteresis loops of magnetization presented in Fig. 5.13(b), measured at different temperatures along the $[100]_{STO}$ direction. While at room temperature the hysteresis loop is perfectly squared, it slightly deviates from the square shape

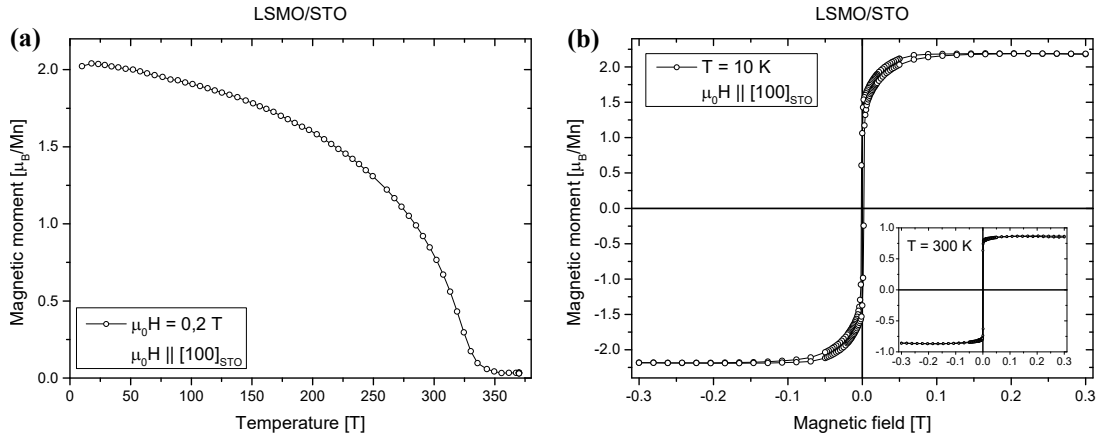

Figure 5.13: SQUID magnetometry results of the LSMO film deposited on STO substrate. All data are corrected to the STO diamagnetic contribution. (a) Temperature dependence of magnetic moment measured at magnetic field of 0.2 T applied along $[100]_{STO}$ direction, measured from low temperatures while heating the sample. (b) Low temperature hysteresis loop along $[100]_{STO}$ direction. The inset shows room temperature hysteresis loop along the same direction.

at 10 K. From Fig. 5.13(a) we determined Curie temperature of the sample deposited on STO as $T_C \sim 340$ K and from Fig. 5.13(b) we determined the low temperature magnetic moment in saturation as $M_S \sim 2.2\ \mu_B$/Mn. These values are lower than those of bulk LSMO due to higher lattice mismatch, compared to films grown on nearly lattice matched LSAT. Curie temperatures and magnetic moments in saturation for all samples are summarized in Table 5.3.

Substrate	$\mu_0 H \parallel$	T_C [K]	M_S [μ_B/Mn]
LAO	$[110]_{LAO}$	308	2.0
LSAT	$[100]_{LSAT}$	361	3.7
STO	$[100]_{STO}$	340	2.2

Table 5.3: Curie temperature T_C and magnetic moment in saturation M_S at low temperature (10 K) for LSMO samples grown on three different substrates, measured by SQUID magnetometry. Direction of the external magnetic field $\mu_0 H$ is indicated.

Figs. 5.14 and 5.15 show temperature dependence of magnetic moment of bare DSO substrate, measured for three different crystallographic directions. The DSO substrate is orthorhombic, in the notation corresponding to orthorhombic unit cell the chosen directions are $[110]_{DSO}$ in-plane (Fig. 5.14(a)), $[\text{-}110]_{DSO}$ out-of-plane (Fig. 5.14(b)) and $[001]_{DSO}$ in-plane direction (Fig. 5.15). The $[110]_{DSO}$ in-plane and $[\text{-}110]_{DSO}$ out-of-plane directions exhibit similar behaviour with same order of magnitude of the magnetic moment at the same value of external magnetic field. However the $[001]_{DSO}$ in-plane direction shows different behaviour with an order of magnitude lower magnetic moment in comparison to the other two directions. It suggests that the DSO substrate exhibits magnetic anisotropy with the $[\text{-}110]_{DSO}$ direction being the magnetization hard axis. These results are in agreement with previous findings of Ke *et al.* [100], who reported on DSO paramagnetism with strong magnetic anisotropy. They performed more detailed measurements, including also the $[100]_{DSO}$ and $[010]_{DSO}$ crystallographic directions, and they found that the easy axis of magnetization lies in the $[100]_{DSO}$

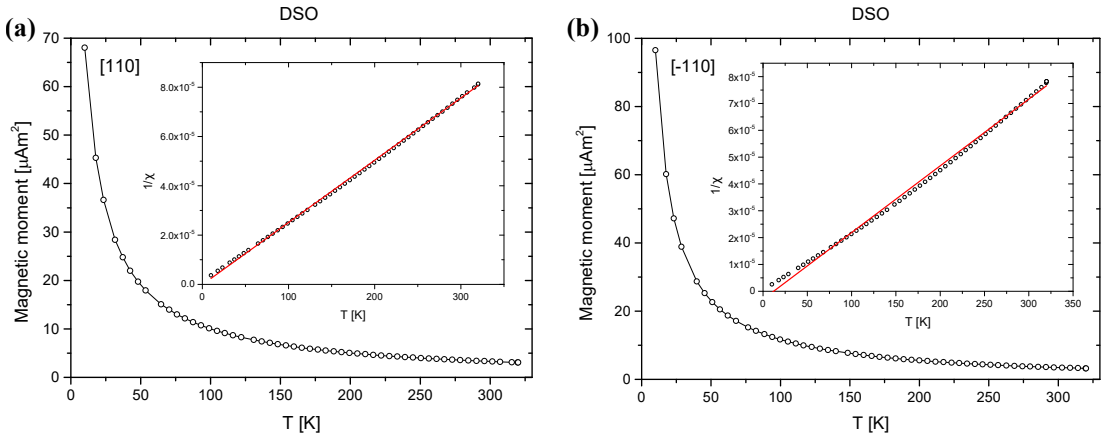

Figure 5.14: SQUID magnetometry results of bare DSO substrate. Temperature dependence of magnetic moment measured at magnetic field of 20 mT along the orthorhombic (a) $[110]_{DSO}$ direction and (b) $[\text{-}110]_{DSO}$ direction. The insets show temperature dependence of inverse susceptibility with a fit according to eq. (5.2).

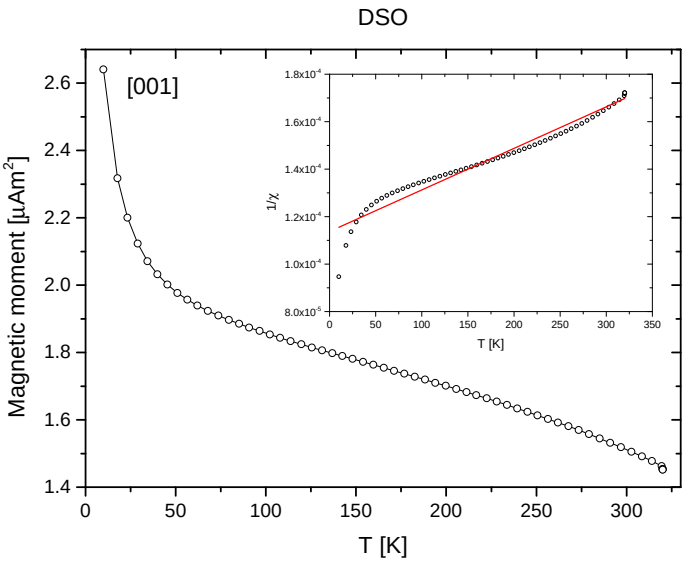

Figure 5.15: SQUID magnetometry results of bare DSO substrate. Temperature dependence of magnetic moment measured at magnetic field of 20 mT along the orthorhombic $[001]_{DSO}$ direction. The inset shows temperature dependence of inverse susceptibility with a fit according to eq. (5.2).

direction, i.e. the direction of orthorhombic a axis.

The temperature dependences in Figs. 5.14 and 5.15 were further fitted according to Curie-Weiss law

$$\chi = \frac{C}{T - \theta_W}, \tag{5.2}$$

where $\chi = M/H$ is magnetic susceptibility, C is a constant and θ_W is the Weiss temperature. The fits were performed as linear fits of temperature dependence of the inverse value of magnetic susceptibility $1/\chi$, as shown in the insets of respective Figures. Obtained values of the Weiss temperature θ_W are in principal agreement with values provided by Ke *et al.* [100], as shown in Tab. 5.4.

It was therefore not possible to characterize magnetic properties of LSMO grown on DSO by means of SQUID magnetometry due to the strong paramagnetic contribution of the substrate. The magnetic anisotropy of DSO makes it extremely difficult or essentially impossible to correct the overall magnetic signal to the substrate contribution and extract the extremely weak magnetic signal of the LSMO film. We therefore demonstrate the room temperature ferromagnetism of LSMO on DSO by means of MOKE spectroscopy, which will be presented later in section 5.1.5.

Crystallographic direction	θ_W [K]	θ_W [K] (Ke *et al.* [100])
[110]	11.9	13.1
[−110]	0.5	10.2
[001]	-649	-850

Table 5.4: Weiss temperatures θ_W of DSO substrate for different crystallographic directions, compared to values reported by Ke *et al.* [100].

5.1.4 Optical characterization

Optical properties of the samples were characterized by means of spectroscopic ellipsometry. The measurements were carried out on a high precision Woollam VASE ellipsometer for three different angles of incidence (60°, 65° and 70°). Both bare substrates and samples with deposited LSMO films were characterized in a spectral range from 0.7 to 6.4 eV.

Measured spectra of ellipsometric angles were fitted in order to determine the diagonal elements ε_1 of permittivity tensor. The data were analyzed assuming a model structure of a homogeneous single layer on the corresponding substrate, using optical properties of the substrates extracted from measurements on the bare commercially provided substrates. This analysis was performed using the CompleteEASE software and it yielded the diagonal elements of permittivity tensor of the LSMO films and their thicknesses. The values of thicknesses were in principal agreement with results obtained by XRD, confirming that films on all four

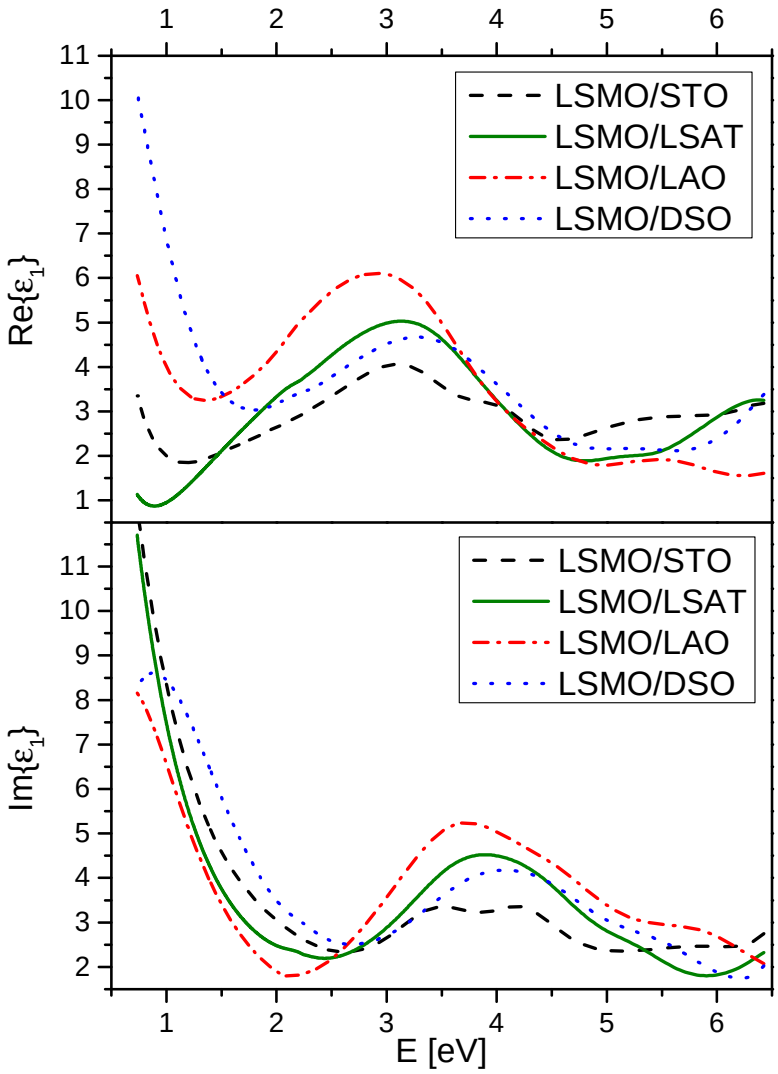

Figure 5.16: Spectra of real and imaginary part of the diagonal elements of permittivity tensor of LSMO films on four different substrates. The spectra were extracted from SE measurements.

substrates are of similar thicknesses of approximately 20 nm. The spectra of diagonal elements were parametrized as a sum of five damped Lorentz oscillators and one damped Cody-Lorentz oscillator, which served to determine energy of the pseudo bandgap E_g^*. The Lorentz oscillator is described by the basic eq. (2.45) introduced in section 2.4.1, here we use it in a slightly different form, which can be found in the CompleteEASE Manual [102]. Cody-Lorentz dispersion function was initially developed to describe optical response of amorphous materials [103]. It allows us to calculate the pseudo band gap energy E_g^*. We use it in the form [102]

$$\varepsilon_{1C-L}(E) = \varepsilon_{1C-L}^{'} + i\varepsilon_{1C-L}^{''}, \tag{5.3}$$

where the real part $\varepsilon_{1C-L}^{'}$ is determined by Kramers-Kronig relations from the imaginary part $\varepsilon_{1C-L}^{''}$ described as

$$\varepsilon_{1C-L}^{''}(E) = \begin{cases} \frac{(E_g^*+E_t)G(E_g^*+E_t)\varepsilon_{1L}^{''}(E_g^*+E_t)}{E}\exp\left(\frac{E-E_g^*-E_t}{E_u}\right) & \text{for } 0 < E < E_g^* + E_t \\ G(E)\varepsilon_{1L}^{''}(E) & \text{for } E > E_g^* + E_t. \end{cases} \tag{5.4}$$

In eq. (5.4) we use energy dependent functions $G(E)$ and $\varepsilon_{1L}^{''}(E)$; $\varepsilon_{1L}^{''}(E)$ is imaginary part of Lorentz oscillator function, $G(E)$ is near-bandgap function defined as

$$G(E) = \frac{(E - E_g^*)^2}{(E - E_g^*)^2 + E_p^2}. \tag{5.5}$$

In eqs. (5.4) and (5.5) we introduced parameters E_p, E_t and E_u; E_p denotes energy, at which Lorentzian behaviour described by $\varepsilon_{1L}^{''}(E)$ transitions to Cody behaviour described by $G(E)$, E_t then denotes energy, at which the absorption behaviour changes from Cody to Urbach, and E_u is the slope of Urbach tail.

Amplitude A_n, energy E_n and broadening Γ_n of each oscillator ($n = 1, \ldots, 6$) as well as the nondispersive term $\varepsilon_{1\infty}$ and pseudo bangap energy E_g^* were adjusted by least square method. The obtained parameters are displayed in Tab. 5.5 and

Substrate	A_1	E_1 [eV]	Γ_1 [eV]	A_2	E_2 [eV]	Γ_2 [eV]	A_3	E_3 [eV]	Γ_3 [eV]	E_g^* [eV]
LAO	6.9	0.9	1.6	0.2	2.2	0.4	8.7	3.7	2.0	2.0
LSAT	14.1	0.6	1.4	0.2	2.2	0.4	5.2	3.8	1.8	1.7
STO	14.1	0.6	1.7	0.5	2.0	1.4	2.4	3.5	1.2	1.4
DSO	7.3	1.2	2.0	0.1	2.3	0.4	4.6	3.8	1.8	1.7
Substrate	A_4	E_4 [eV]	Γ_4 [eV]	A_5	E_5 [eV]	Γ_5 [eV]	A_6	E_6 [eV]	Γ_6 [eV]	$\varepsilon_{1\infty}$
LAO	1.3	4.6	1.5	1.7	5.9	1.8	0.9	7.3	0.9	1.5
LSAT	1.8	4.4	1.6	0.6	5.3	1.0	2.0	6.7	1.2	1.4
STO	1.4	4.3	1.0	2.0	6.1	3.1	1.1	6.6	0.4	1.5
DSO	1.8	4.5	1.7	1.2	5.6	1.5	2.5	6.7	0.4	1.3

Table 5.5: Parameters of the six electron transitions used to describe the optical response of LSMO films on four different substrates; A_n, E_n and Γ_n for $n = 1, ..., 6$ stand for the amplitude, energy and broadening of the oscillators, $\varepsilon_{1\infty}$ is the nondispersive term and E_g^* is energy of the pseudo bandgap determined from the third (Cody-Lorentz) oscillator.

the corresponding spectra of the diagonal elements of permittivity tensor are shown in Fig. 5.16 for all films.

The fits revealed six electronic transitions centered around approximately 0.8, 2.2, 3.7, 4.4, 5.6 and 6.8 eV. Main spectral features are the two transitions around 3.7 and 4.4 eV. They have already been reported in bulk LSMO [104] and polycrystalline films on silicon [105], as well as in single crystalline thin films grown on STO [106] and LAO [107, 108] substrates. They are however most often described as one transition centered around 4 eV. Such description is common in both optical [108] and magneto-optical [104, 106] studies and the transition is assumed to be a charge transfer between O $2p$ and Mn $3d$ energy levels. One magneto-optical study of LSMO on LAO [107] also supports presence of two transitions at approximately 3.6 and 4.1 eV and our theoretical approach using two transitions around the critical energy of 4 eV shows better agreement with experimental ellipsometric data as well. In spectra of films deposited on STO and LAO, the two transitions can be clearly distinguished. This model is further supported by our magneto-optical investigation, which is presented in the next section.

In order to facilitate visualisation of contributions of the individual transitions we present Fig. 5.17. It shows a spectrum of imaginary part of the diagonal elements of permittivity tensor ε_1 for the LSMO sample deposited on LSAT substrate. It is an example of the convolution of individual contributions to the overall spectrum, where each of the transitions is easily visible.

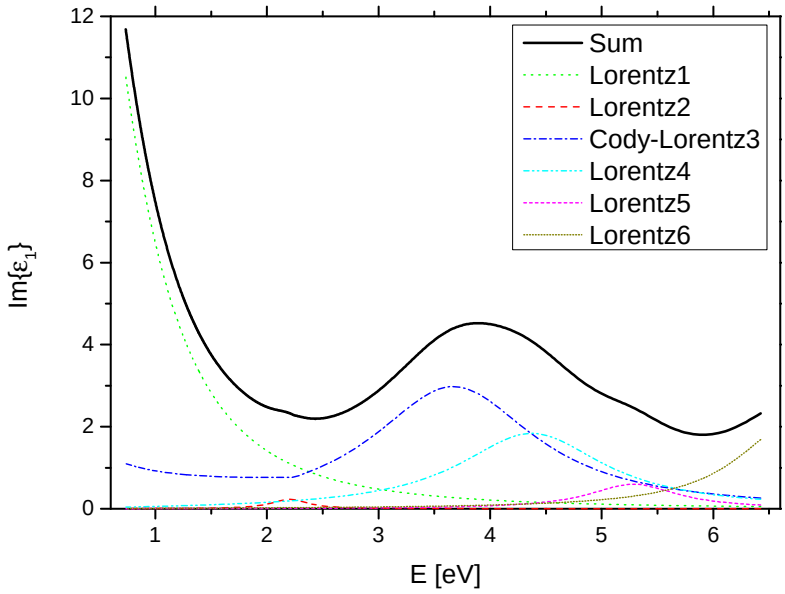

Figure 5.17: Spectrum of imaginary part of the diagonal elements of permittivity tensor ε_1 of LSMO film grown on LSAT substrate, depicted as a sum of the individual transitions.

5.1.5 Magneto-optical spectroscopy

Magneto-optical Kerr effect spectroscopy was used to determine the off-diagonal elements of permittivity tensor ε_2. Room temperature MOKE measurements were carried out using generalized magneto-optical ellipsometry with rotating analyzer

on a homemade MO spectrometer. The data were recorded in polar configuration at 1 T of applied magnetic field, in spectral range from 1.5 to 5.0 eV. The applied magnetic field was verified to be sufficient for complete saturation of the films.

Obtained spectra of Kerr rotation and Kerr ellipticity are displayed in Fig. 5.18. For clarity, spectra of the films deposited on LAO and DSO substrates are magnified by ten. The strong suppression of ferromagnetic ordering in these two films results in lower amplitude of the MOKE signal and it is caused by the large value of lattice mismatch and therefore large epitaxial strain, as already discussed in section 5.1.3. It was impossible to characterize the magnetic properties of LSMO on DSO by SQUID magnetometry, but we can make several conclusions about its magnetic properties based on the present MOKE spectra. The clear MO signal at room temperature unambiguously demonstrates room temperature ferromagnetism of this sample. Furthermore the lowest magnitude of the MOKE in comparison to other films indicates that T_C of LSMO on DSO is close to room temperature. The MOKE amplitude of the other three films is in agreement with

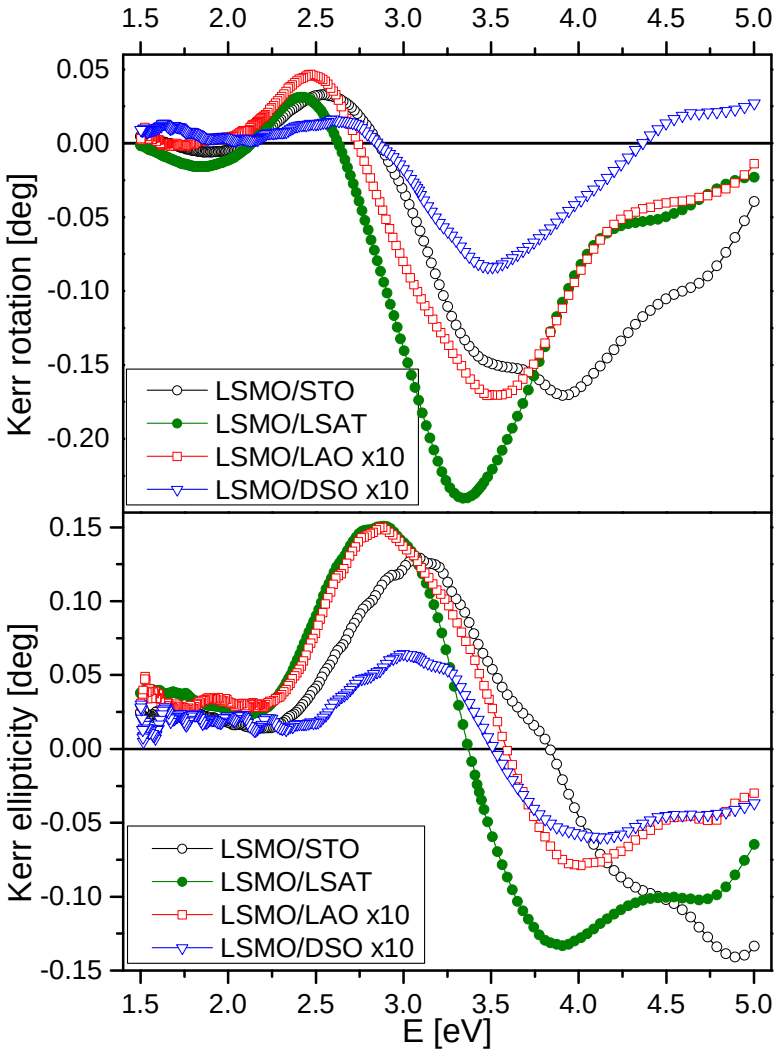

Figure 5.18: Spectra of Kerr rotation and Kerr ellipticity of LSMO films on four different substrates. For clarity, the spectra of films deposited on LAO and DSO substrates are magnified by ten.

the SQUID measurements presented in section 5.1.3. The largest MOKE amplitude is observed in case of LSMO grown on LSAT, followed by LSMO on STO. A strong suppression of MOKE signal is apparent in case of LSMO on LAO, corresponding to T_C near room temperature as revealed by SQUID ($T_C \sim 308$ K).

The off-diagonal elements of permittivity tensor of the LSMO films were calculated from MOKE spectra presented in Fig. 5.18 and from spectra of the diagonal elements of permittivity tensor presented in Fig. 5.16 and Tab. 5.5. The calculations were based on transfer matrix formalism introduced in section 2.5. Line shapes and parameters of diamagnetic and paramagnetic transitions were described in section 2.4.2. Maximum amplitude $(\varepsilon_2^{'})_{max}$ or $(\varepsilon_2^{''})_{max}$, respectively, resonant frequency ω_0 and broadening Γ of employed oscillators were adjusted by least square method. The spectra were initially modeled as a sum of two electronic transitions, whose presence has already ben reported in LSMO films before. The most prominent spectral feature, which can be observed as a pro-

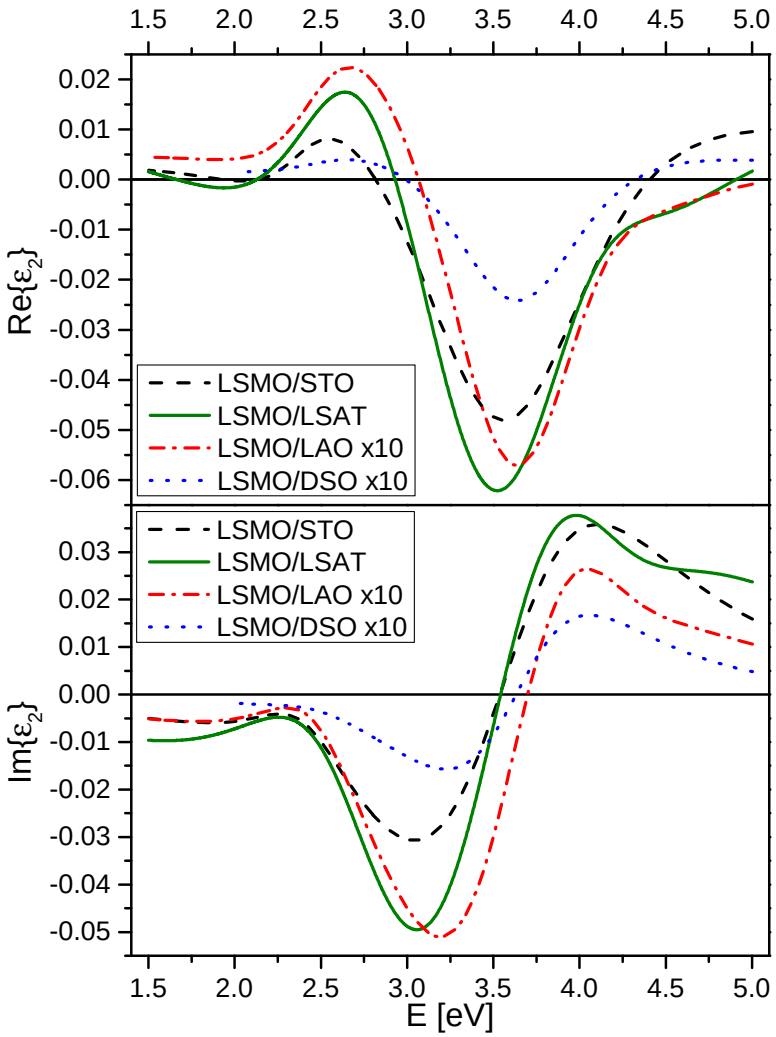

Figure 5.19: Spectra of real (top panel) and imaginary (bottom panel) part of the off-diagonal elements of permittivity tensor of LSMO films on four different substrates. They are calculated from diagonal permittivity tensor elements and MOKE spectra. For clarity, the spectra of films deposited on LAO and DSO substrates are magnified by ten.

nounced minimum around 3.6 eV in the Kerr rotation spectra (see top panel of Fig. 5.18), has already been reported in bulk LSMO [104], polycrystalline films on silicon [105], as well as in single crystalline thin films grown on STO [74] and LAO [107] substrates. It is related to charge transfer diamagnetic transition from O $2p$ into Mn t_{2g} states in the minority spin channel. The second most prominent spectral feature, visible as a maximum around 2.4 eV in the Kerr rotation spectra, is represented by crystal field paramagnetic transition from Mn t_{2g} into Mn e_g states in the majority spin channel. It has already been observed in LSMO grown on silicon [105], STO [74] and LAO [107] substrates as well. These two transitions were sufficient to describe spectra of the off-diagonal elements of films grown on STO and DSO substrates, i.e. grown under tensile strain. However, presence of a third electronic transition was revealed around 4.3 eV in spectra of LSMO deposited on LAO and LSAT substrates, i.e. grown under compressive strain.

To identify presence of this transition in Kerr rotation spectra is rather difficult because the MOKE signal also contains optical response of the whole structure, including substrate. As amplitude of this transition is relatively small, its contribution to the Kerr rotation spectra is not so evident. Concerning the film grown on DSO, the Kerr rotation spectrum crosses the zero line at around 4.3 eV (see Fig. 5.18). In spectra of the films grown on LAO and LSAT substrates, presence of the additional transition decreases spectral amplitude so that the zero crossing at 4.3 eV is not visible. However, spectrum of the sample grown on STO markedly differes from the others due to above mentioned complexity of MOKE signal. In this spectral region, a combination of high penetration depth of LSMO and high reflectivity change of the STO substrate results in strong optical contribution of the substrate to the overall MOKE signal. This effect has already been described by previous research [109]. In order to correctly interpret MOKE spec-

Substrate	LAO	LSAT	STO	DSO
Transition 1	Crystal field transition Mn $t_{2g} \rightarrow e_g$			
$(\varepsilon_2^{''})_{max}$	0.010	0.472	0.069	0.001
ω_0 [eV]	2.45	2.50	2.38	2.49
Γ [eV]	0.43	0.66	0.38	0.42
Transition 2	Charge transfer transition O $2p \rightarrow$ Mn t_{2g}			
$(\varepsilon_2^{'})_{max}$	0.04	1.16	0.36	0.01
ω_0 [eV]	3.63	3.51	3.55	3.64
Γ [eV]	0.87	1.14	0.97	0.73
Transition 3	Crystal field transition Mn $t_{2g} \rightarrow e_g$			
$(\varepsilon_2^{''})_{max}$	-0.03	-0.69	No such	
ω_0 [eV]	4.26	4.25	transition under	
Γ [eV]	0.56	0.67	tensile strain	

Table 5.6: Parameters of the three electron transitions used to describe the magneto-optical response of LSMO films on four different substrates; $(\varepsilon_2^{'})_{max}$ or $(\varepsilon_2^{''})_{max}$, ω_0 and Γ stand for the maximum amplitude, resonant frequency and broadening of the oscillators. The parameters were fitted from MOKE spectra presented in Fig. 5.18 with use of the diagonal permittivity tensor elements presented in Table 5.5 and Fig. 5.16.

tra in terms of individual transitions, it is therefore necessary to perform a careful analysis of spectra of the off-diagonal elements of permittivity tensor, which are directly related to the electronic structure. We present them in Fig. 5.19. Here the optical contribution of the STO substrate is separated, and the differences between compressively and tensilely strained films become clearer. Parameters of the transitions are given in Tab. 5.6.

The differences between compressively and tensilely strained films can be understood even better with help of Figs. 5.20 and 5.21. They show spectra of imaginary part of the off-diagonal elements of permittivity tensor of all the investigated samples. The spectra are illustrated as a sum of contributions from the individual transitions. All the spectra are dominated by the main contribution from the diamagnetic transition, which is represented by the typical dispersive "S" shape centered around 3.6 eV. The weaker paramagnetic transitions further modify this dominant contribution. For the tensilely strained films (see Fig. 5.20), the resulting spectrum is only slightly altered by the first transition around 2.4 eV, and the global maximum and minimum, given by the diamagnetic transition, remain of approximately the same amplitude, i.e. when compared to each other. On the other hand, spectra of compressively strained films (see Fig. 5.21) are clearly affected by the presence of the additional paramagnetic transition around 4.3 eV, consequently exhibiting amplitude of the global maximum markedly lower in comparison to the global minimum.

The exact origin of the third electronic transition around 4.3 eV has not been satisfactorily explained so far. The transition was observed by Liu *et al.* [107] in LSMO films grown on (001) LAO substrates, i.e. grown under compressive strain, which is in agreement with our observations. According to Liu *et al.*, this transition occurs around 4.1 eV and it is associated with a charge transfer diamagnetic transition from O $2p$ into Mn t_{2g} states in the minority spin channel. This classification seems unlikely given the temperature dependent MOKE spectroscopy investigations performed by Rauer *et al.* [110]. They studied LSMO grown on (100) STO substrate, i.e. grown under tensile strain. They presented off-diagonal elements of permittivity tensor in temperature range from 75 K to 330 K. The spectra measured at room temperature are in full agreement

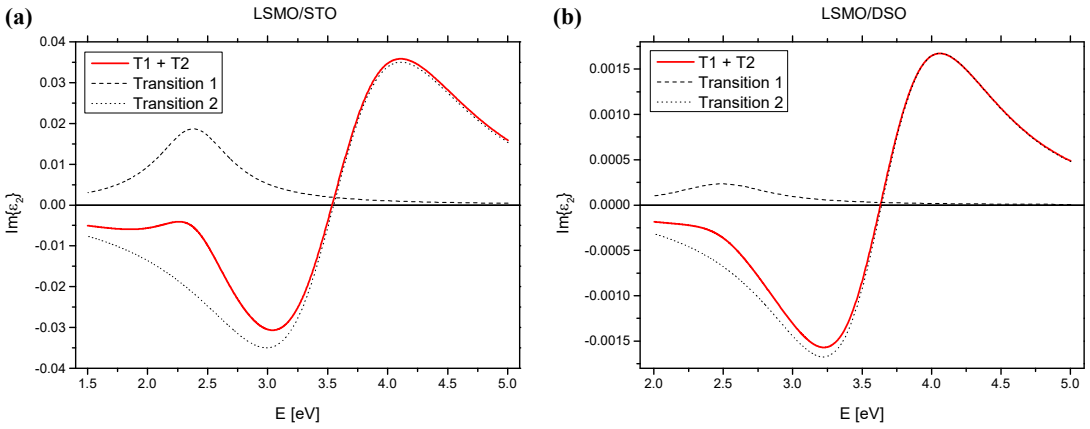

Figure 5.20: Spectra of imaginary part of the off-diagonal elements of permittivity tensor of LSMO films grown on (a) STO and (b) DSO substrates, i.e. under tensile strain. The spectra are depicted as a sum of the individual transitions.

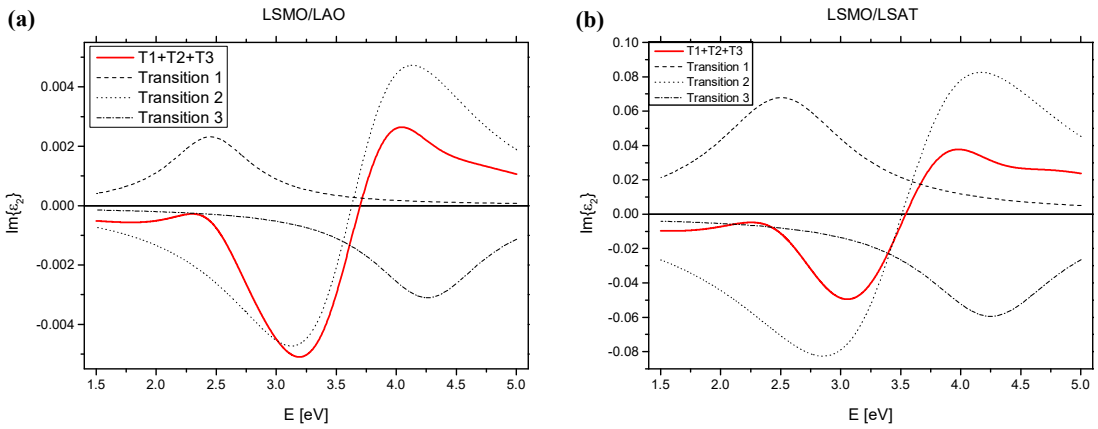

Figure 5.21: Spectra of imaginary part of the off-diagonal elements of permittivity tensor of LSMO films grown on (a) LAO and (b) LSAT substrates, i.e. under compressive strain. The spectra are depicted as a sum of the individual contributions.

with our results, exhibiting two prominent spectral features around the same respective energies of 2.3 and 3.6 eV. With decreasing temperature, not only expected overall amplitude increment of the spectra is observed, but a clear signature of another spectroscopic feature is revealed around energy of 4.3 eV. The shape and energy position of this transition is in agreement with the fits of our spectra measured on compressively strained LSMO, revealing this transition as paramagnetic. The temperature dependence of this transition also supports its classification as paramagnetic, in contradiction to the suggestion of Liu *et al.* We therefore assume that this paramagnetic transition originates in Mn t_{2g} levels in the majority spin channel. Occupation of these states can be influenced by both temperature or epitaxial strain, resulting in partial of full suppression of the observed electronic transition in MOKE spectra.

The work of Rauer *et al.* also allows us to make an important conclusion concerning OOR influence on resulting MO properties. We have shown that LSMO films exhibit different OOR behaviour when grown under compressive and tensile strain. The presence of the third electron transition in low temperature spectra of films grown under tensile strain [110] therefore suggests that OOR are not the key parameter. The temperature change does not induce structural changes large enough to alter the octahedra tilt system. As the OOR remain the same with temperature while the third transition is induced, it indicates that OOR do not have a significant influence on MO properties of LSMO.

The proposed classification of the third electron transition can be further supported in view of a study on electronic structure of LSMO presented by Uba *et al.* [111]. Although their results about the exact electronic structure remained inconclusive in case of LSMO, they reported an optical interband Mn $t_{2g} \rightarrow e_g$ transition around 4.5 eV in case of the LSMO parent compound $LaMnO_3$. Even though they did not find sufficient experimental evidence for this transition in their MOKE spectra measured on LSMO, they did find presence of the corresponding manganese orbitals at energies allowing this transition in spectra of density of states (DOS) of LSMO obtained by *ab initio* calculations. Other previously reported DOS calculations of LSMO would support occurance of this transition

as well [107, 112].

Last arguments in favour of the suggested electronic model consider magnitudes of the observed transitions and their optical activity. While the charge transfer diamagnetic O $2p \rightarrow$ Mn t_{2g} transition is the most prominent feature in observed MOKE spectra, both paramagnetic transitions exhibit significantly smaller amplitude, which supports their classification as Mn $d - d$ transitions. Next, the fact that we observed the third transition (around 4.3 eV) in optical response of all LSMO films, see Tab. 5.5, Fig. 5.16 and Fig. 5.17, regardless their strain state, indicates that MO activity of this transition is governed via occupation of the spin-orbit split Mn t_{2g} ground states. The occupation can be influenced by both temperature and epitaxial strain, leading either to enhancement or suppression of its MO activity. The first paramagnetic transition (around 2.4 eV) originating in the same ground state exhibits similar behaviour regarding both the temperature dependence [110] and the overall amplitude decrease under tensile strain (see Tab. 5.6). Although it is not fully suppressed under tensile strain, the amplitude is significantly diminished. The suppression is especially pronounced in the film grown on DSO substrate, i.e. under the largest tensile strain, which indicates strong sensitivity of the Mn t_{2g} levels on the epitaxial strain.

5.1.6 *Ab initio* density of states calculations

In order to further investigate the influence of oxygen octahedra rotations and distortions on electronic structure of LSMO we employed *ab initio* calculations. They were performed using the Vienna Ab initio Simulation Package [113, 114]. The LSMO unit cell used in the calculations was different from real unit cell described in sections 1.1 and 5.1.2 in case of bulk LSMO and thin films, respectively, and they should not be confused. Here the bulk LSMO was decribed by a unit cell with 15 atoms, which can be schematically represented as a [001]-ordered $(SrMnO_3)_1(LaMnO_3)_2$ superlattice, similar to previous works [112, 115]. In order to simulate epitaxial films, the pseudocubic in-plane lattice parameters a of bulk unit cell were chosen according to LAO and DSO bulk values and pseudocubic c parameters were relaxed using the external optimizer GADGET developed by Bučko *et al.* [116]. To study the effect of OOR a $2 \times 2 \times 2$ supercell with 120 atoms was used. The calculated total density of states (TDOS) spectra are displayed in Fig. 5.22.

Bottom panel of Fig. 5.22 shows a comparison of TDOS calculated for bulk LSMO with rigid tilt system #23 ($a^0a^0a^0$) and bulk LSMO with tilt system ($a^-a^-c^-$). This theoretical tilt system only slightly deviates from the real rhombohedral tilt system #14 ($a^-a^-c^-$), regarding the tilt amplitude around $[001]_{pc}$ axis, as a result of simplified layered structure of LSMO used in the calculations. There are almost no visible changes in the TDOS spectral behaviour except for the highest energy band located around 3 eV above Fermi level. This band is associated with La $4f$ states, which are not involved in observed MO transitions and therefore it will be omitted in further discussion. This negligible change of TDOS spectra suggests that MO transitions are not influenced by OOR. As shown previously in section 1.4.3, several studies have pointed out that OOR engineering can be a successful way for tuning transport and magnetic properties of thin LSMO

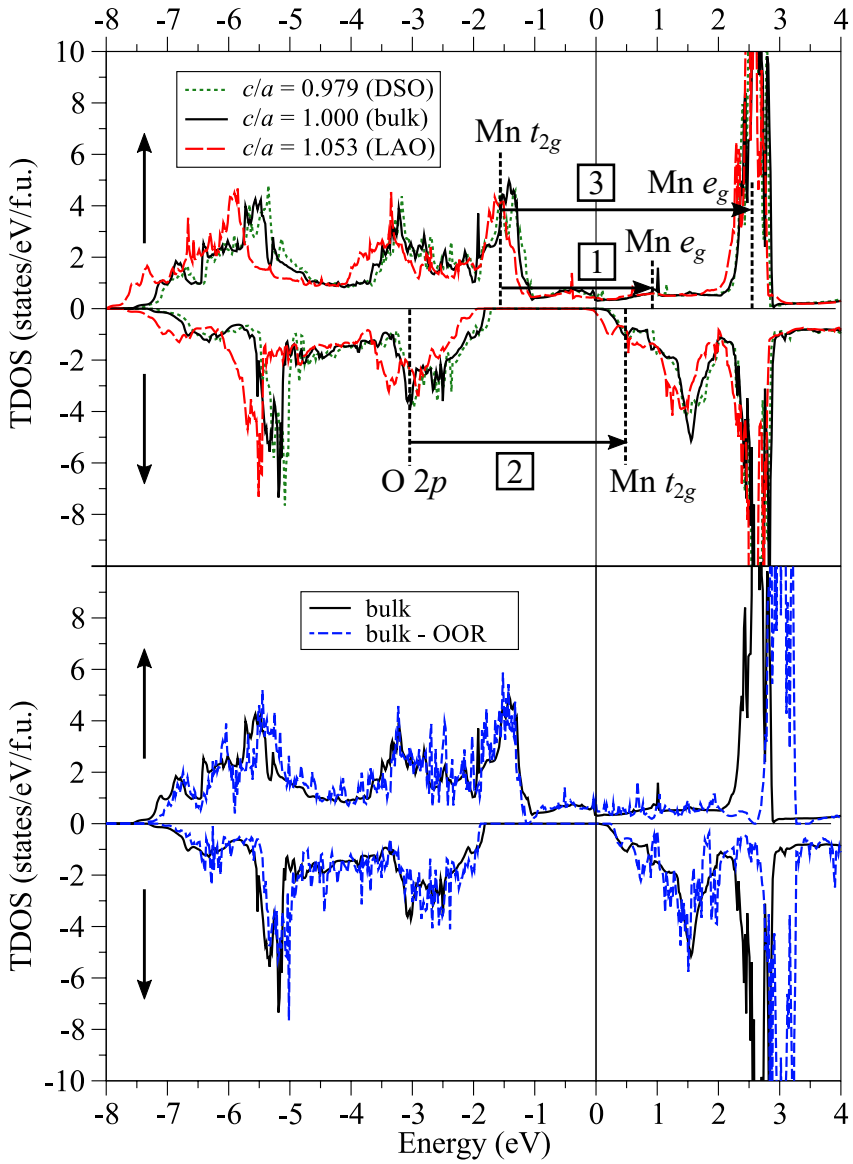

Figure 5.22: TDOS spectra obtained by *ab initio* calculations. Top panel shows unstrained bulk LSMO and strained LSMO corresponding to growth on LAO and DSO substrates. Bottom panel shows bulk LSMO with no rotations of oxygen octahedra and bulk LSMO with quasi-real tilt system ($a^-a^-c^-$). Up and down arrows indicate majority and minority spin channel, respectively. The horizontal arrows represent observed MO transitions labelled by numbers according to Tab. 5.6.

layers [57, 59, 61]. Liao *et al.* [60] even presented tuning of magnetic anisotropy by means of OOR and Kan *et al.* [58] achieved similar effect in SRO thin films. Despite this clear evidence in favour of importance of OOR engineering, especially with respect to transport and magnetic properties of LSMO thin films, on the other hand our *ab initio* calculations imply that influence of OOR on TDOS spectra is negligible. This does not indicate an important role of OOR in influencing the MO properties, in agreement with previous observations following from the experimental results of Rauer *et al.*

Based on the minor influence of OOR on TDOS spectra, the effect of strain

was further studied in rigid oxygen octahedra system with no tilts. Top panel of Fig. 5.22 shows TDOS of bulk LSMO compared to two cases of LSMO strained in such a way that the pseudocubic c/a ratio corresponds to growth on LAO and DSO substrates. The results are in pricipal agreement with previous findings of Ma *et al.* [112], i.e. there is no significant change in spectral shape, however there is a visible shift of the whole spectrum to higher energies when going from compressive to tensile strain. Such shift itself would be insufficient to explain appearance of the third electronic transition in MOKE spectra of compressively strained LSMO. As we have shown previously in section 1.4.1, it is nonetheless well known that compressive or tensile strain leads via consequent octahedra distortions to different preferential orbital ordering in LSMO thin films [39, 40, 42, 43]. Although it is typically described as an interface effect explaining the DE suppression in LSMO near the substrate, it clearly demonstrates the sensitivity of Mn $3d$ levels to octahedra distortions. We therefore assume that the mechanism responsible for appearance of the third electronic transition in MOKE spectra of compressively strained LSMO is related to Mn $3d$ states. As Mn t_{2g} states in majority spin channel are the closest occupied states near the Fermi level, which are therefore most likely to be influenced by temperature, we expect that the observed transition originates from these energy levels.

Such findings are in agreement with arguments provided in previous section 5.1.5. The presented *ab initio* calculations therefore further supports the suggested electronic model. They showed that the Mn t_{2g} levels are most likely the ground states of the third electronic transition. Moreover they confirmed previous findings of other groups, which showed that location of Mn e_g bands is such that an interband Mn $t_{2g} \rightarrow e_g$ transition in the majority spin channel is possible around energy of approximately 4.3 eV. We did not present the element resolved DOS, however the position of Mn e_g band is indicated in the top panel of Fig. 5.22. The Mn e_g band partially overlaps with the La $4f$ band, but unlike the lanthanum band the manganese band is not affected by OOR. Therefore we show that the observed paramagnetic transitions can unlikely be influenced by OOR engineering, but they can be suppressed or enhanced by changes in occupation of the Mn t_{2g} states in the majority spin channel. These changes can be induced by temperature, or strain induced octahedra distortions.

Last argument that gives a strong support for the suggested electronic model follows from a direct comparison of experimental spectra of the off-diagonal elements of permittivity tensor presented in Fig. 5.19 with spectra of ε_2 obtained by *ab initio* calculations. These spectra were calculated from joint density of states, and they are shown together with the experimental values in Fig. 5.23 for two cases of the LAO and DSO substrates, which provide extreme values of the epitaxial strain.

A very good spectral agreement is clearly visible for both samples, demonstrating validity of the approximations made in description of LSMO unit cell in the *ab initio* calculations. All the three discussed transitions can be recognized in the theoretical spectra at energies corresponding to their experimental values. The only larher difference can be seen at lower energies in spectra of LSMO on LAO. This is the region governed mainly by the first paramagnetic transition, which is therefore likely to be influenced by temperature. As the experimental spectra were obtained at room temperature, while the *ab initio* calculations were

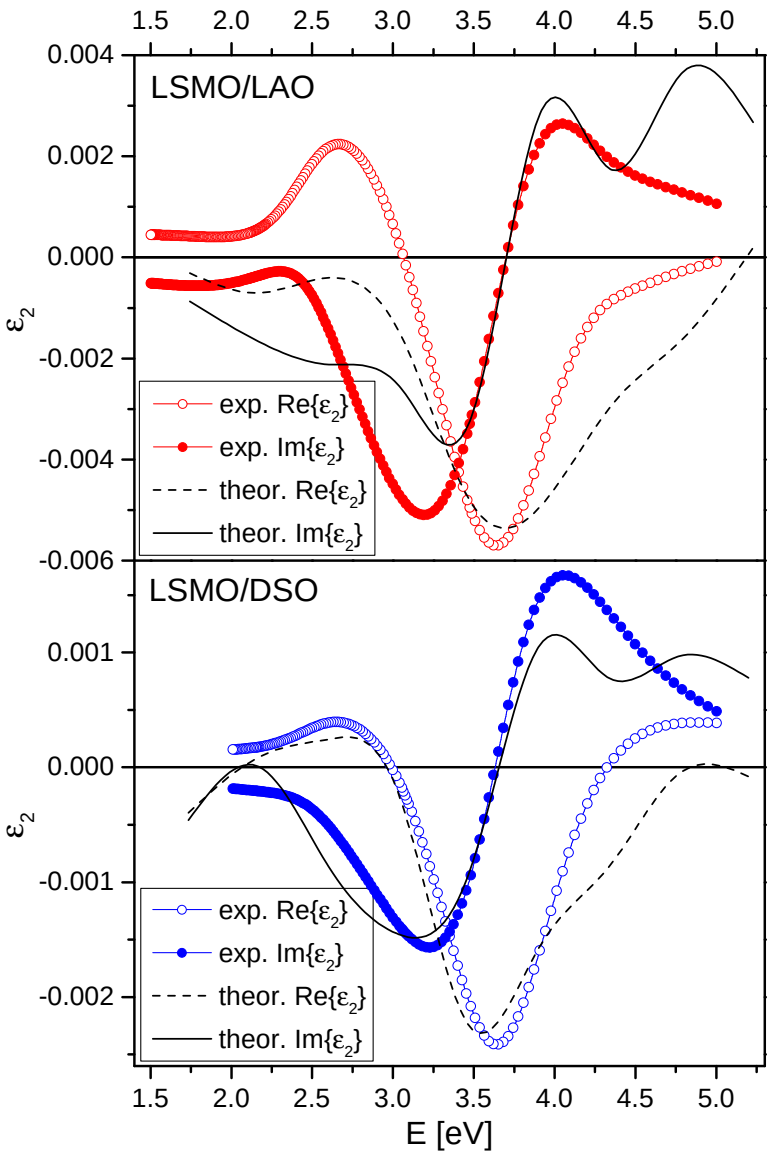

Figure 5.23: Spectra of real and imaginary part of the off-diagonal elements of permittivity tensor of LSMO films deposited on LAO (top panel) and DSO (bottom panel) substrates. Spectra obtained experimentally by means of spectroscopic ellipsometry and MOKE spectroscopy are compared to spectra obtained theoretically by *ab initio* calculations. The theoretical spectra were multiplied by factors of 0.065 (LAO) and 0.020 (DSO) in order to compensate for the temperature induced decrease of magnetization. The decrease is different for both samples, for which the factors also differ.

performed at zero Kelvin, such disagreement could be expected. Region of the most prominent diamagnetic transition, which is not influenced by temperature, shows an excellent agreement with experimental spectra. It is easily seen on the main minimum in the real part, and on the zero crossing near 3.6 eV in the imaginary part. High energies are governed by the third paramagnetic transition, which is again influenced by temperature. While in the experimental spectra the transition is visible only in LSMO/LAO (see suppressed amplitude of imaginary part maximum, no zero crossing near 4.3 eV in real part), in the theoretical

spectra it is apparent for LSMO on both the LAO and DSO substrates. This clearly demonstrates that temperature is a key parameter for appearance of the third electron transition. In agreement with experimental observations of Rauer *et al.*, our calculations show that the transition is visible at low temperatures even in MOKE spectra of tensilely strained LSMO films.

On the other hand, as OOR were left out in these calculations, our results in Fig. 5.23 demonstrate that the parameter of OOR is not necessary to be considered for description of MO response of LSMO. Its influence is likely to be minor compared to the major role of octahedra distortions. Such conclusion can be expected given the rotational symmetry of MnO_6 octahedron with respect to the manganese atoms. As can be seen from the TDOS spectra presented in Fig. 5.22, the energy positions of Mn levels in DOS spectra do not change under OOR. On the contrary, position of, for example, the La $4f$ states significantly changes as the OOR are not symmetrical with respect to the lanthanum atoms. As the observed MO transitions are governed by crystal field of the Mn atoms, which experience the rotational symmetry, it is then natural to expect no significant change of MO properties under OOR, leaving the octahedra distortions as substantially more important parameter. The theoretical spectra of the off-diagonal elements of permittivity tensor presented in Fig. 5.23 then fully justify this expectations, confirming key role of temperature and oxygen octahedra distortions in controlling MO properties of LSMO.

5.2 Dynamic application of strain

The second part of this chapter deals with the dynamic way of strain application to LSMO. It begins with evaluation of the device quality by basic measurements of XRD, AFM and characterization of its electrical properties. After demonstrating that the device is fully functional, we characterize its optical and magneto-optical propeties. The experimentally measured optical properties are used to calculate the MO response based on transfer matrix (Yeh) formalism. The MO response measured under dynamic application of strain is then compared and interpreted with use of the theoretical spectra. We find relatively small influence on the MO response when the voltage is applied. Such a little amplitude of the effect can be explained by factors other than the strain induced by the piezoeletric layer, which shows that the strain transfer from PZT into the LSMO layer requires further improvements.

5.2.1 Structural, morphological and electrical characterization

The crystallinity and surface morphology of the LSMO/PZT heterostructure was verified before patterning by means of XRD and AFM, using the same experimental equipment as described in section 5.1.1. Fig. 5.24 shows a symmetric $\theta - 2\theta$ scan and surface AFM image of the as grown multilayer. The $\theta - 2\theta$ scan in Fig.5.24(a) also contains a fit of the LSMO peak according to eq. (5.1), which yielded the film thickness $t = 20.0$ nm and pseudocubic lattice parameter $c = 3.847$ Å. Such value confirms expected in-plane tensile distortion of the LSMO, based on pseudocubic lattice parameters of bulk LSMO $a_{LSMO} = 3.876$ Å [94] and PZT $a_{PZT} = 4.036$ Å [117]. Fig. 5.24(b) shows a homogeneous surface of the sample with $R_{RMS} = 1.2$ nm, confirming a good quality of the deposited LSMO layer.

In order to check the ferroelectric properties of PZT, the capacitance versus

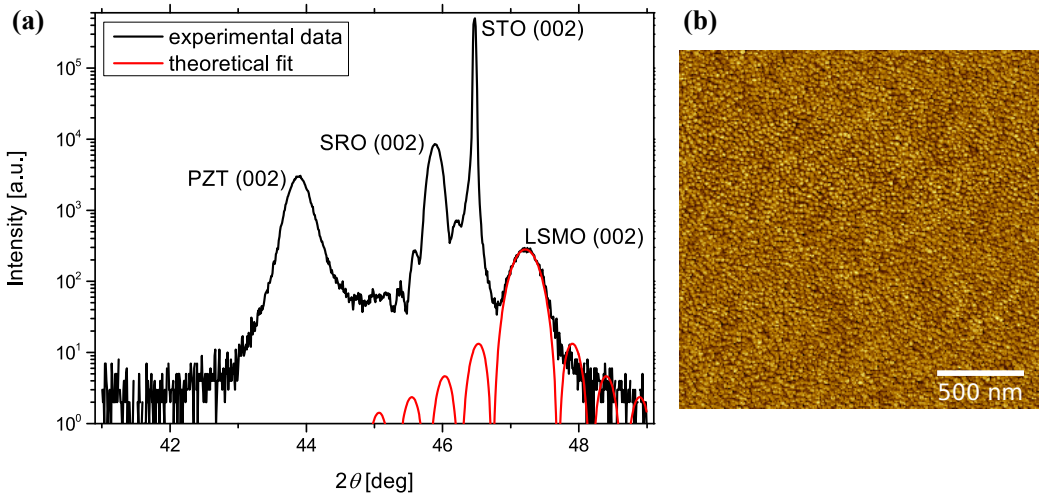

Figure 5.24: (a) Symmetric $\theta - 2\theta$ XRD scan and (b) surface AFM image ($2 \times 2\ \mu m^2$) of the LSMO/PZT/SRO heterostructure on STO substrate before lithography processing.

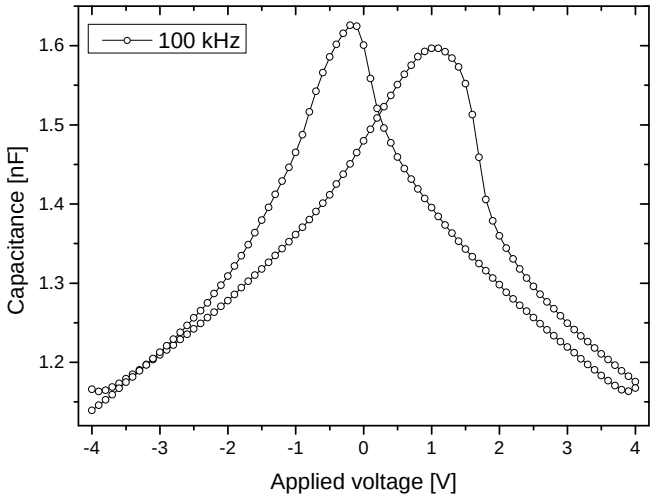

Figure 5.25: Capacitance versus voltage ($C-V$) characteristics of the PZT layer measured at a frequency of 100 kHz.

voltage ($C - V$) characteristics of the PZT layer after lithography processing was measured between two LSMO electrodes as shown in Fig. 5.25. The $C - V$ curve exhibits expected buttefly shape with hysteretic behaviour typical for ferroelectric films. When sweeping the voltage from -4 V to +4 V and vice versa, the polarization switching occurs at coercive voltage $V_C^+ = 1.1$ V and $V_C^- = -0.2$ V, respectively, where the capacitance curve exhibits its maxima. At these points the strain is minimal, and then it increases with increasing voltage. The maximum value of the capacitance at V_C^- is $C_{max} = 1.6$ nF, giving a value of the relative dielectric constant of the PZT layer ~ 800 at 100 kHz. This is in typical range for PZT films [118, 119], confirming good quality of the deposited heterostructure and full functionality of the device.

5.2.2 Optical and magneto-optical investigation

Optical properties of the heterostructure were studied by means of SE, using the same experimental setup as described in section 5.1.4. The measurements were carried out in spectral range from 0.7 to 6.4 eV. In order to characterize optical properties of the PZT and SRO layers, we used additional reference samples of single SRO and PZT layers on STO substrate and LSMO/PZT bilayer on STO substrate. The SE data were used to determine the diagonal elements of permittivity tensor ε_1. When modelling the optical response of PZT, the spectra were parametrized by a sum of three Lorentz oscillators, for SRO the spectra were parametrized by three Lorentz oscillators and a Drude contribution of free electrons. The resulting parameters were obtained from a combined fit of ellipsometric measurements on one PZT single layer, two SRO single layers, one LSMO/PZT bilayer and one LSMO/PZT/SRO trilayer, all on STO substrate.

Fig. 5.26(a) shows the spectra of real and imaginary part of diagonal elements of permittivity tensor of PZT calculated from SE measurements. The spectra are compared to results of Czekaj *et al.* [120], who grew PZT films on various substrates, including Si, stainless steel and glass. The spectra shown in Fig. 5.26(a) were obtained on the sample deposited on glass. Although the substrate used

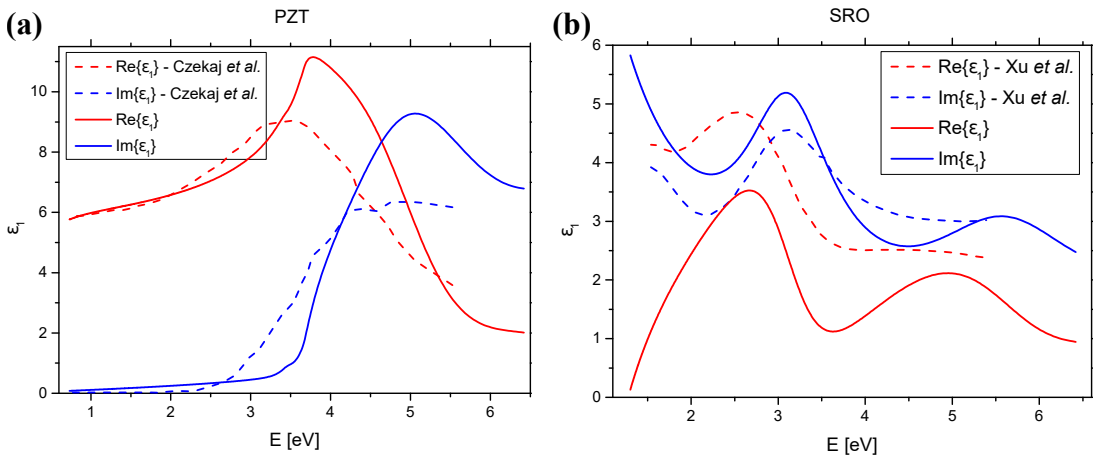

Figure 5.26: Spectra of diagonal elements of permittivity tensor ε_1 calculated from SE data in case of (a) PZT, compared to results of Czekaj *et al.* [120], (b) SRO, compared to results of Xu *et al.* [121].

in our study was different, the principal agreement between results of Czekaj *et al.* and our results confirms validity of our theoretical model used for description of the PZT optical response. The spectral behaviour corresponds very well, while there are some differences in the amplitude. Such small discrepancies of the optical properties can be expected when growing a material on different substrates. However, the overall agreement further confirms good quality of the deposited PZT layer.

Fig. 5.26(b) shows the spectra of real and imaginary part of diagonal elements of permittivity tensor of SRO calculated from SE measurements. The spectra are compared to results of Xu *et al.* [121], who presented optical properties of SRO layer on STO substrate, corresponding properly to our case. Both the spectral behaviour and amplitude agrees well with our results. Small differences can be visible in the infrared part, where Xu *et al.* described the spectra using a Lorentz oscillator, while we used the Drude model as SRO exhibits very good conducting properties. The principal agreement, however, confirms validity of our theoretical model as well as good quality of the SRO layer.

MO properties of the sample were first characterized before lithography processing on the as grown LSMO/PZT/SRO/STO heterostructure. The measurement was carried out using the same experimental setup as described in section 5.1.5. Kerr rotation was measured in polar configuration at nearly normal light incidence under the applied magnetic field of 1 T, which is sufficient for sample saturation. The spectrum of Kerr rotation is shown in Fig. 5.27. It is similar to the spectra of LSMO single layers presented in Fig. 5.18, there is the prominent spectral minimum around 3.5 eV preceded by the main spectral maximum. The peaks are however remarkably narrower and the maximum is located at higher energy ($\sim$ 3.2 eV) compared to 2.4 eV in case of the single layers. There are also additional spectral features, which were not present in spectra of the single layers. As demonstrated by theoretical calculations, these features in MOKE spectra originate from optical interference in the PZT layer.

Fig. 5.27 shows theoretical model of Kerr rotation calculated by transfer matrix formalism using optical properties of PZT and SRO presented in Fig. 5.26

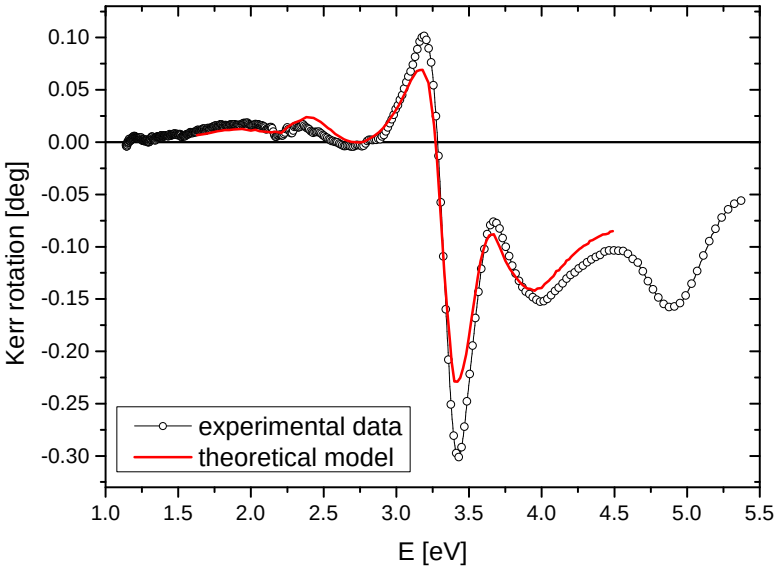

Figure 5.27: Kerr rotation spectrum measured on LSMO/PZT/SRO/STO heterostructure before lithography processing and theoretical Kerr rotation spectrum calculated using spectra of ε_1 of PZT and SRO presented in Fig. 5.26 and spectra of ε_1 and ε_2 of bulk-like LSMO taken from [106].

and both optical and MO properties of bulk-like LSMO taken from [106]. As will be shown later, the resulting Kerr rotation spectrum exhibits strong dependence on the PZT layer thickness, therefore it is possible to tune the value of the unknown PZT thickness to describe properly the measured MOKE spectrum. Using this approach we were able to refine the thickness of PZT layer to $t = 130$ nm. The model curve presented in Fig. 5.27 shows an excellent agreement with the experimental data, confirming properly calculated optical properties of the PZT and SRO layer as well as high quality of the LSMO layer.

MO investigation of the device after lithography processing was carried out using focusing optics which allowed us to reduce the beam diameter to $\sim 200\,\mu$m, therefore all reflected and detected signal comes from one $300 \times 300\,\mu\text{m}^2$ LSMO pad (see Fig. 4.2). Use of the focusing optics required measurement in polar configuration at 60° angle of incidence. The applied magnetic field was 0.5 T, which is typically a sufficient field for full saturation of LSMO at room temperature, even along its hard axis of magnetization [51]. Fig. 5.28 shows Kerr rotation spectrum in the ultraviolet region, without and with applied voltage of 4 V across the PZT layer.

Several observations can be made. First, the spectral behaviour is slightly different compared to Fig. 5.27, which is due to different angle of incidence. While all the previous measurements were carried out under nearly normal light incidence, here the experiment was performed under the angle of incidence $\sim 60°$ due to the focusing optics. We can also notice that the overall spectrum is shifted to higher values of Kerr rotation, now exhibiting several zero crossings and much larger value of the global maximum, compared to diminished value of the global minimum. This is likely to be caused by contribution of Faraday effect of the focusing optics to the overall MO signal. As we are here interested in differential MO effect, we did not correct resulting signal for this parasitic contribution. The

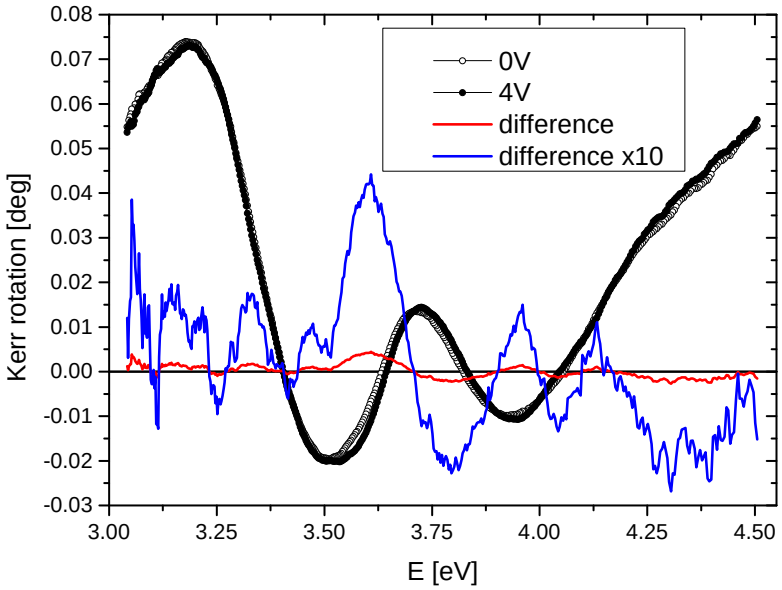

Figure 5.28: Kerr rotation spectrum on the LSMO/PZT device with no voltage applied and with 4 V of voltage applied across the PZT layer, measured in polar configuration at 60° angle of incidence. Difference of both measurements is also shown. At 4 V of applied voltage, the strain induced in LSMO layer is estimated to be lower than 0.1 % [6].

difference of both measured spectra is also shown in Fig. 5.28, in most of the spectrum the amplitude of the difference is smaller than the noise level, it only exceeds the noise level between 3.5 to 3.8 eV. Even though the observed difference may be related to strain induced changes of the MO properties of LSMO, the amplitude is very small and there is an alternative explanation of the effect, which seems to be more plausible.

As mentioned earlier, when modelling the KR spectrum of the as grown heterostructure, we investigated influence of the thicknesses of individual layers on resulting MO response of the sample. Amplitude of the thickness change was purposedly exaggerated to magnify the effect. Note that the calculations were made for normal light incidence.

Top panel of Fig. 5.29 shows calculated KR signal in case of LSMO thickness varying from 15 to 35 nm while keeping thicknesses of other layers constant. As expected, with increasing LSMO thickness the overall MO signal also increases. A shift of the whole spectrum to lower energies is also visible, it is however too small to support explanation of the voltage induced changes in KR spectrum via strain induced changes in the LSMO layer. At 4 V of applied voltage, the estimated strain induced in LSMO layer is lower than 0.1 % (cf. Tab. 4.1), which gives a theoretical estimate of the KR difference around $4 \cdot 10^{-5}$ degree. As we can see in Fig. 5.28, such value is two orders of magnitude lower than the measured difference.

Bottom panel of Fig. 5.29 shows KR in case of SRO thickness varying from 20 to 40 nm, having almost negligible influence on the resulting KR spectrum. There is almost no spectral change and only very small increment of the KR signal with increasing SRO thickness. These changes are even smaller than in the previous

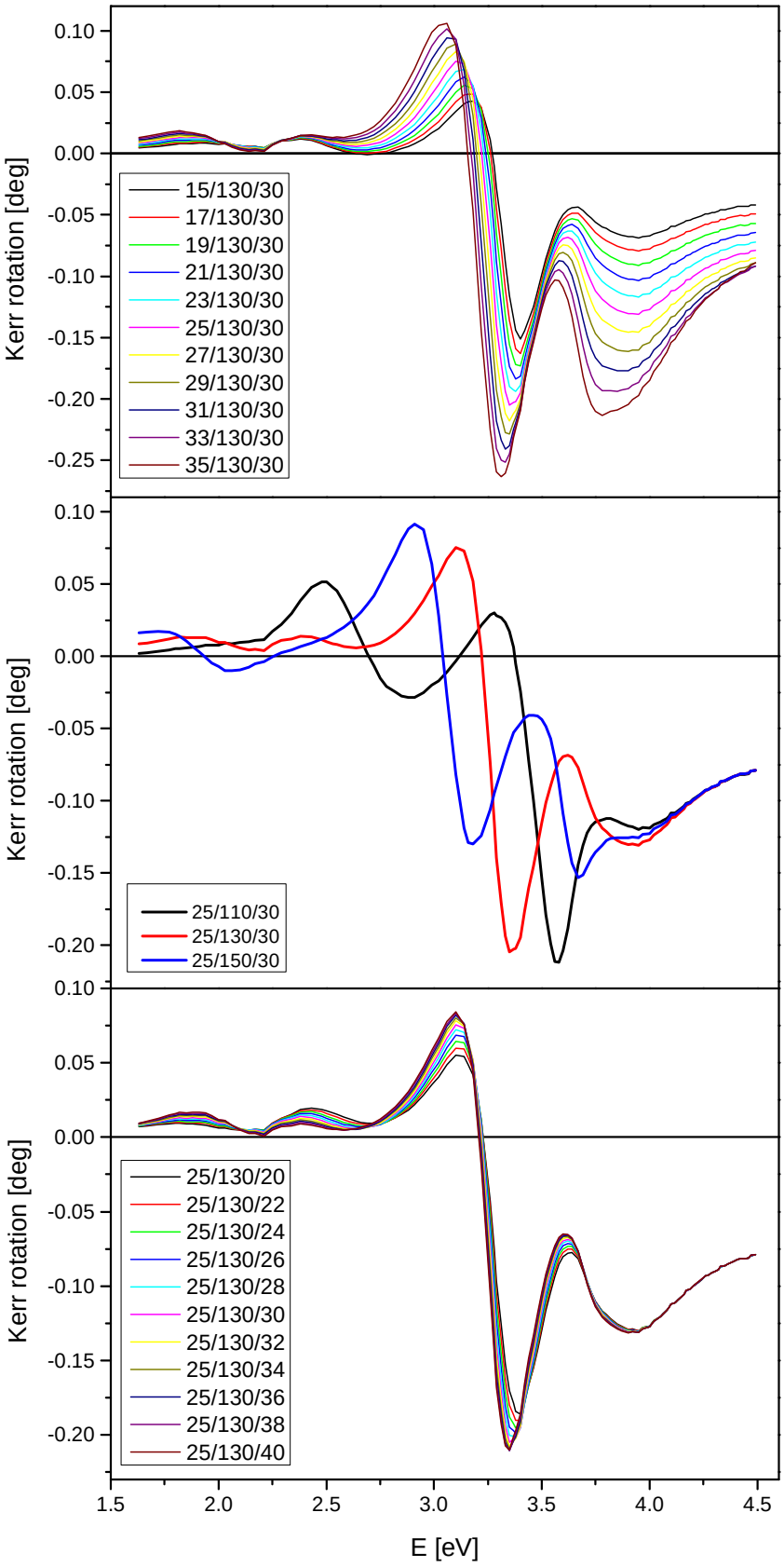

Figure 5.29: Theoretical models of MO response of LSMO/PZT/SRO heterostructure on STO substrate with varying thicknesses of individual layers: LSMO (top panel), PZT (middle panel) and SRO (bottom panel). The numbers in each legend indicate thicknesses [nm] of the LSMO/PZT/SRO layers, respectively.

case, where the LSMO thickness was altered, therefore the influence of SRO layer can be safely ruled out.

Middle panel of Fig. 5.29 shows KR for three different thicknesses of the PZT layer (110, 130 and 150 nm), demonstrating a significant influence of the PZT thickness on resulting MO response. Amplitude of the spectrum does not change considerably, but there is a remarkable shift of the spectral features to lower energies with increasing thickness. That is clearly a result of optical interference in the PZT layer. At 4 V of applied voltage, the thickness change of the PZT layer can be estimated up to 1 nm, which gives a theoretical estimate of the KR difference around $2 \cdot 10^{-2}$ degree. Such value is three orders of magnitude higher than the estimated influence of LSMO layer thickness variation, and it shows a principal agreement with the measured KR difference (see Fig. 5.28). Therefore even though we did not calculate the KR for corresponding angle of incidence (the calculations were made for normal light incidence), from the general behaviour of the MO signal we can deduce that the observed voltage induced change in KR spectrum presented in Fig. 5.28 is most likely caused by voltage induced thickness change of the piezolectric PZT layer. As we have demonstrated in first part of this chapter, static strain can have significant influence on resulting MO properties of LSMO. However, the typical amplitude of static epitaxial strain was approximately one order of magnitude higher (see Tab. 4.1) compared to 0.1 % achieved dynamically with use of the PZT underlayer. In order to increase magnitude of the voltage induced control of MO response, we need to find a way how to transfer strain from PZT into LSMO more effectively.

6. Influence of substrate miscut on magnetization of $SrRuO_3$

The sixth chapter presents all the results achieved during investigation of the SRO samples, whose physical properties were studied with respect to different substrate miscut angles (see section 4.3). The chapter begins with structural characterization of the samples, where the basic differences in their crystallographic properties can be seen. The magnetization dynamics is then studied by SQUID magnetometry and MFM. Magneto-optical Kerr microscopy is used as well in order to provide additional information about magnetic domains. We reveal several differences in the magnetization reversal process, and we attribute these differences to the structural changes induced by the different substrates.

6.1 Crystallographic properties and morphology

Proper crystallinity and surface morphology of the SRO films was investigated by means of XRD and AFM, respectively. The XRD measurements were carried out using PANanalytical X'Pert PRO diffractometer. The AFM images were taken at room temperature by Bruker Dimension Edge AFM microscope.

Fig. 6.1(a) shows a symmetric $\theta - 2\theta$ scan of the SRO1 sample (vicinal STO substrate). The measured intensity was fitted by formula (5.1), which yielded the SRO film thickness $t = 27.7$ nm and pseudocubic out-of-plane lattice parameter $c_c = 3.949$ Å. Fig. 6.1(b) shows surface AFM image of the sample, clearly revealing atomic steps with small step width as expected in case of the vicinal substrate. The surface roughness is $R_{RMS} = 1.6$ nm, confirming good quality of the deposited SRO layer. However the roughness is slightly higher compared

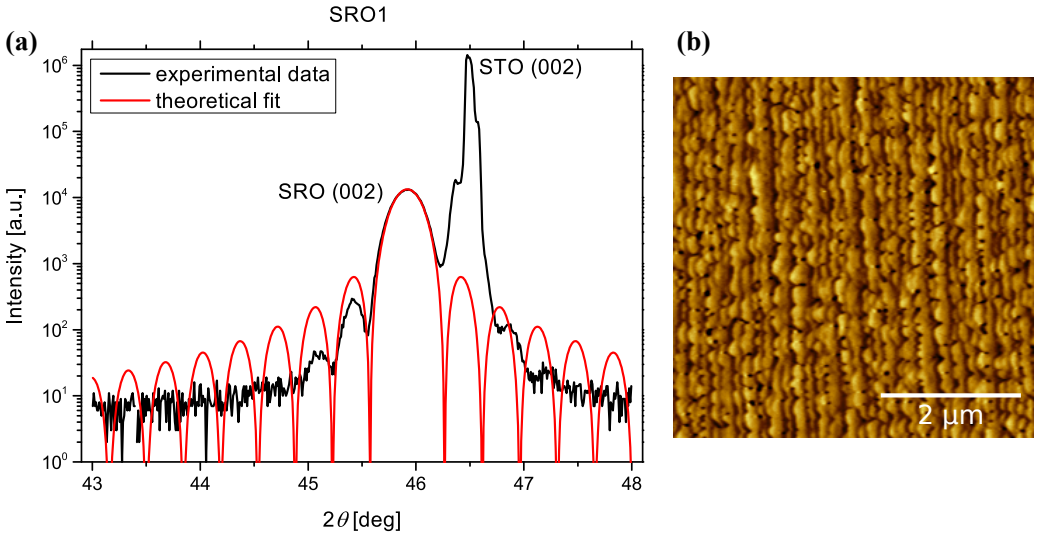

Figure 6.1: (a) Symmetric $\theta-2\theta$ XRD scan and (b) surface AFM image ($5\times5\mu m^2$) of SRO film deposited on vicinal STO substrate.

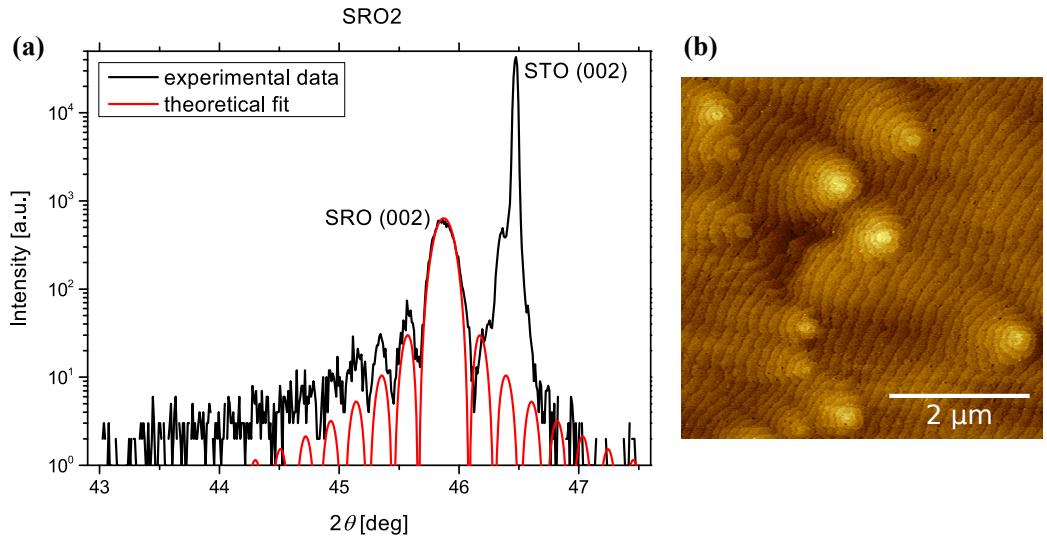

Figure 6.2: (a) Symmetric $\theta-2\theta$ XRD scan and (b) surface AFM image ($5\times5\mu m^2$) of SRO film deposited on STO substrate of low miscut angle ($\sim 0.1°$).

to SRO2 (cf. Tab. 6.1) due to the high miscut angle and step bunching during SRO growth [122].

Fig. 6.2(a) shows $\theta - 2\theta$ scan of the SRO2 sample (substrate of low miscut angle). The fit according to eq. (5.1) gives film thickness $t = 45.5$ nm and c_c lattice parameter $c_c = 3.953$ Å. Fig. 6.2(b) shows AFM image of the surface with clear signature of the atomic steps. As expected the step width is larger as the miscut angle is smaller compared to SRO1. Several island-like features are clearly visible

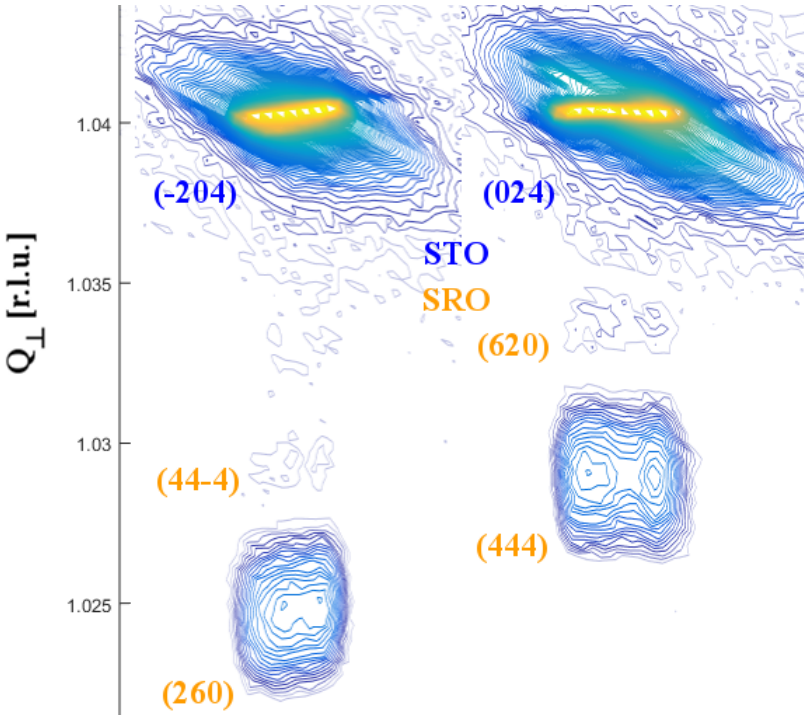

Figure 6.3: RSMs around (-204) and (024) STO Bragg reflections measured on SRO film deposited on vicinal STO substrate.

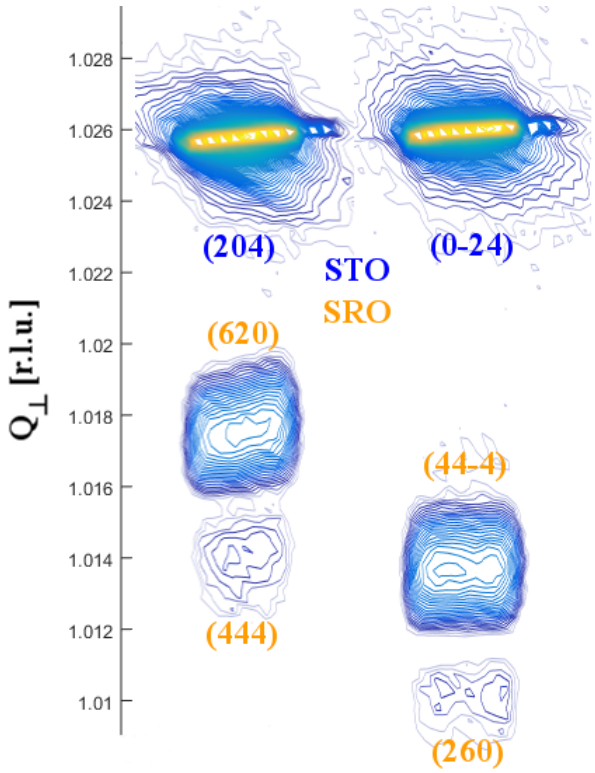

Figure 6.4: RSMs around (204) and (0-24) STO Bragg reflections measured on SRO film deposited on STO substrate of low miscut angle ($\sim 0.1°$).

and indicate 3D growth at higher thicknesses of deposited SRO layer. Due to the smaller miscut angle the surface roughness is also smaller compared to SRO1, in this case it is $R_{RMS} = 0.3$ nm, confirming high quality of the SRO layer.

In order to investigate crystallinity of the samples in detail, we measured RSMs around (204) family of STO Bragg reflections (cf. Fig. 4.3(b)). The measurements were carried out at two azimuths for each sample. The results are shown in Figs. 6.3 and 6.4, respectively.

Fig. 6.3 shows the RSMs of SRO1. The same lateral position of both STO and SRO peaks indicates that the films remain fully strained. Although we expected a growth of only one crystallographic variant on vicinal STO substrate, the RSMs show presence of a second SRO variant in this case as well. Above the main SRO peak a blurred side peak is visible. From intensity maxima the ratio of SRO peaks was roughly estimated as 1:9.

Fig. 6.4 shows the RSMs of SRO2. They reveal fully strained SRO even at higher thickness of the deposited layer. A growth of the second crystallographic

Sample	α [deg]	t [nm]	c_c [Å]	R_{RMS} [nm]	2^{nd} variant [%]
SRO1	1.0	27.7	3.949	1.6	10
SRO2	0.1	45.5	3.953	0.3	30

Table 6.1: Structural parameters of SRO films grown on STO substrates of two different miscut angles α. Film thickness t, pseudocubic out-of-plane lattice parameter c_c, surface roughness R_{RMS} and estimated fraction of the second crystallographic variant are listed.

variant was expected in this case and indeed the SRO side peaks are clearly visible. The volume of the second variant is significantly higher, the ratio of SRO peaks was estimated to approximately 1:2. This means that the second crystallographic variant represents around 30% in case of SRO2 while it represents only 10% in case of SRO1. The structural parameters of both samples are summarized in Tab. 6.1.

6.2 Magnetic properties

The magnetization process was studied by SQUID magnetometer (Quantum design, MPMS7 XL, RSO option). Fig. 6.5(a) shows hysteresis loop of SRO1 sample measured at temperature $T = 20$ K with external magnetic field applied perpendicular to the sample surface. The field was ramped at 68 µT/s. At this fast rate the coercive field was determined as $\mu_0 H_{C1,fast} = 145$ mT. The measurement temperature of 20 K was chosen as optimal value with respect to the Curie temperature $T_{C,bulk} = 160$ K [7] as well as with respect to the temperature dependence curve of the SRO magnetic moment [12]. Magnetic moment of SRO in saturation at low temperature is 1.6 μ_B/Ru [123]. Saturation magnetization determined from Fig. 6.5(a) reaches 1.5 μ_B/Ru, demonstrating high quality of the deposited SRO layer.

Fig. 6.5(b) shows a difference in the magnetization process when ramping the magnetic field at different rates. A zoomed part of the loop presented in Fig. 6.5(a) is compared to a loop measured at a slower average rate of 1.1 µT/s in a region around the coercive field. In case of the slow loop a lower value of the coercive field was found $\mu_0 H_{C1,slow} = 140$ mT, clearly demonstrating a difference in the dynamics of magnetization reversal process. In Fig. 6.5(b) in case of the slow field ramping, multiple data points for each field value are visible. That is because in the vicinity of coercive field we kept the magnetic field at a constant value for 27 minutes while measuring a set of one hundred data points. Therefore for each value of the magnetic field time evolution of magnetization is clearly visible. Lines in the figure are guides to the eye, connecting the data points

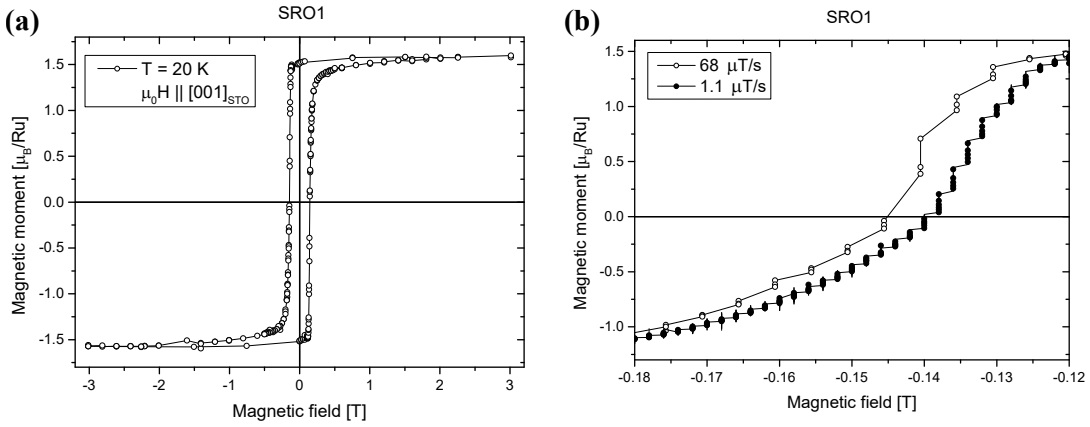

Figure 6.5: (a) Hysteresis loop of magnetization of SRO film deposited on vicinal STO substrate, measured by SQUID magnetometry at 20 K with magnetic field applied perpendicular to the sample surface. (b) Zoom of hysteresis loops of magnetization near coercive field measured at two different rates of 68 and 1.1 µT/s.

in chronological order of recording. The average ramping rate is then calculated across the whole region around coercive field.

Fig. 6.6(a) shows hysteresis loop of SRO2 sample measured at 20 K with magnetic field applied perpendicular to the sample surface. The field was ramped at 258 µT/s, coercive field at this rate was found $\mu_0 H_{C2,fast} = 185$ mT. Similarly to Fig. 6.5(a), the loop exhibits square-like behaviour with one noticeable difference. Around ±0.5 T a small but clearly remarkable drop of magnetization can be observed. This shape of the hysteresis loop indicates two different contributions to the magnetic moment coming from the two different crystallographic variants. Here it is visible due to higher representation of the second SRO variant, but the magnetization drop becomes indistinct in case of SRO1, where volume of the second variant is almost negligible. The low temperature saturation moment determined from Fig. 6.6(a) is 1.2 μ_B/Ru. This value is slightly lower than in case of SRO1, which might be due to the presence of two SRO variants and therefore lower crystalline quality of the sample. Presence of multiple crystallographic variants leads to intermediate areas among them, where the crystalline structure is not exactly defined. However, we assume that the effect would be very small as no significant additional broadening is visible in the XRD measurements. Unfortunately we are not aware of any previous research investigating influence of presence/absence of multiple crystallographic variants on magnetic properties of SRO more in detail.

Fig. 6.6(b) shows the difference in the magnetization process when ramping the magnetic field at different rates. Here the initial loop is compared to a loop measured at a slower average rate of 2.6 µT/s around the coercive field. In case of the slow loop the coercive field was found lower $\mu_0 H_{C2,slow} = 180$ mT, exhibiting similar behaviour in comparison to SRO1. Each set of data points at one value of the magnetic field was recorded during 1 hour, clearly demonstrating evolution of magnetization on the timescale of tens of minutes, similarly to the case of SRO1. We will further compare this dynamic behaviour with the MFM measurements presented in the following section.

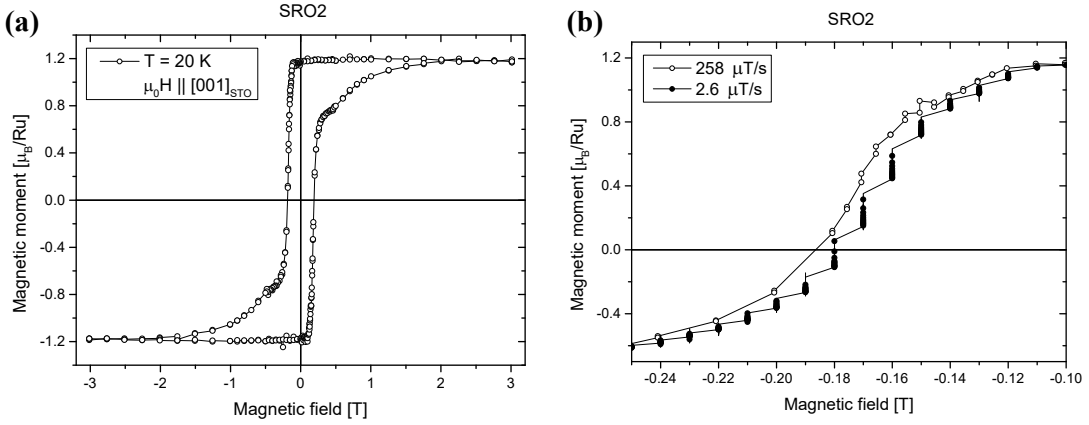

Figure 6.6: (a) Hysteresis loop of magnetization of SRO film deposited on STO substrate of low miscut angle ($\sim 0.1°$), measured by SQUID magnetometry at 20 K with magnetic field applied perpendicular to the sample surface. (b) Zoom of hysteresis loops of magnetization near coercive field measured at two different rates of 258 and 2.6 µT/s.

6.3 Magnetic domains imaging

6.3.1 Magnetic force microscopy

In order to visualize the magnetic domains we employed low temperature atomic force microscope attoAFM/MFM Ixs, which was inserted in PPMS 14 (cryostat). The PPMS 14 does not allow a real zero-field cooling due to residual field of the superconducting coil, so we only focused on the magnetization process from fully magnetized state. The samples were magnetized at magnetic field of +3 T or higher (a control MFM scan was performed back at zero field for each sample). After that two measurement modes were chosen: (i) small negative field was applied and kept during the MFM measurement, (ii) small negative field was applied, and the MFM measurement was then performed at zero field to avoid further magnetization reversal process. MFM data were analyzed and plotted using Gwyddion software [97].

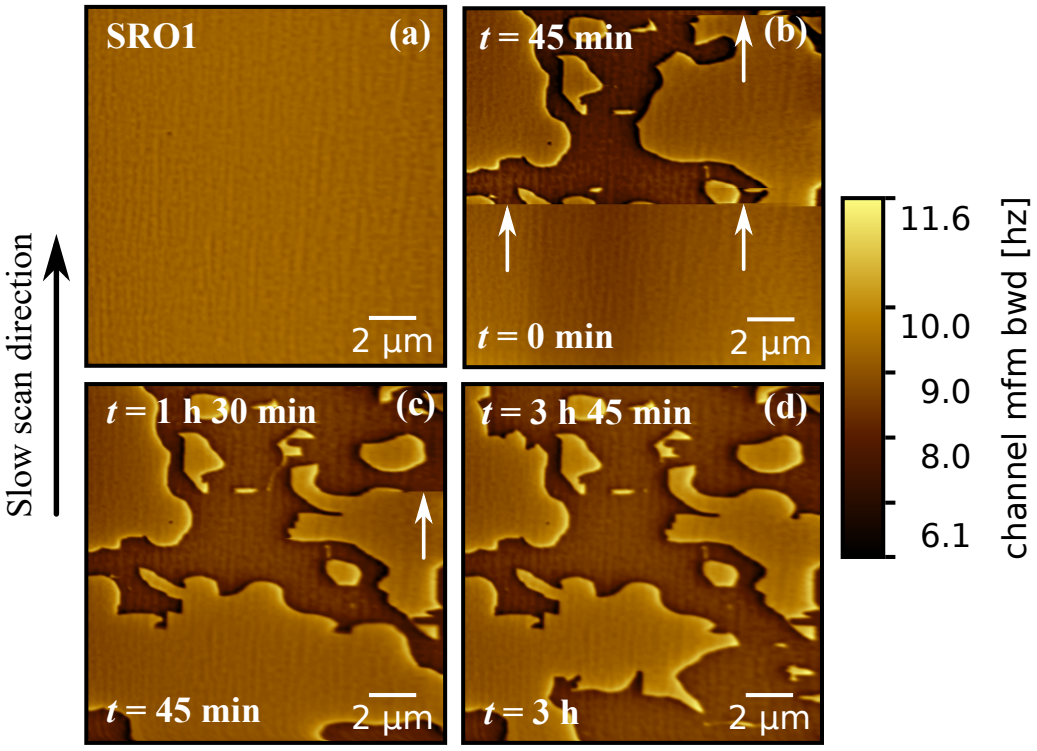

Figure 6.7: MFM images ($15 \times 15\ \mu m^2$) of magnetization reversal in SRO film deposited on vicinal STO substrate, measured at 20 K with field applied perpendicular to sample surface. Slow scan direction was vertical, proceeding upwards, as indicated by the black arrow. (a) Fully saturated state measured at +3 T, (b) first scan at -119 mT, where beginning of the switching process can be seen, (c) second scan at -119 mT measured right after the first scan, (d) last scan at -119 mT after nearly 4 hours, where further magnetization switching is still visible. White arrows in (b) and (c) point out horizontal division lines between bright (initial) and dark (reversed) areas, that are just being switched during the scan. Areas below these lines appear switched in following image. The time after field application is indicated for the beginning (bottom) and the end (top) of each scan.

A typical series of MFM scans of SRO1, taken at 20 K, is shown in Fig. 6.7. Duration of each scan was approximately 45 minutes. The slow scan direction is indicated by a black arrow in the figure. The first scan (shown in Fig. 6.7(a)) was taken after saturating the sample at +3 T. We can see a homogeneously magnetized area of the sample with a signature of the atomic steps, coming from the crosstalk of topography (cf. Fig. 6.1(b)). Then we applied small negative field of -119 mT, that was kept during the measurement. The beginning of magnetization reversal process is shown in Fig. 6.7(b). Bright areas represent the initial magnetization while the dark areas are reversed. The homogeneous bottom half of the image is still fully saturated. After approximately 20 minutes the large bright area abruptly ends as the first switching event is covered by the horizontal movement of the scanner. As expected from the SQUID magnetization measurements, the magnetization reversal process further continues in time as shown in Fig. 6.7(c) taken right after the first scan while keeping the same field of -119 mT. Further increase of the reversed (dark) area can be still observed after nearly 4 hours at the same magnetic field as demonstrated in Fig. 6.7(d). Such slow time evolution of the magnetic domain pattern is in agreement with the magnetization relaxation observed by SQUID (cf. Fig. 6.5(b)).

Fig. 6.8 shows a series of MFM scans taken at 20 K in case of SRO2. Duration of each scan was 45 minutes. Fig. 6.8(a) shows the remanent state after saturating the sample at +5 T. We can see a homogeneously magnetized area with signature of 3D islands in the top left corner, coming from the crosstalk on topography (cf. Fig. 6.2(b)). Other bubble-like features with non regular shape can be visible across the image. They clearly exhibit magnetic signal that cannot be erased with magnetic fields up to 14 T, which was the largest field in our experimental setup. Origin of these features will be discussed later. Fig. 6.8(b) shows the first scan taken after application of small negative field of -151 mT, that was further kept during the measurement. The reversed parts of the image increase with time as shown in Fig. 6.8(c), taken after more than 2 hours from the initial field application. As demonstrated in Fig. 6.8(d), the magnetization pattern still evolves after nearly 4 hours, exhibiting similar timescale of several hours as in case of the magnetization relaxation in SRO1. The only apparent difference of the magnetization reversal process then remains in the size of the magnetic domains, that are notably smaller in case of SRO2. This observation suggests that the density of pinning centers is higher in SRO2, leading to more indented domain pattern.

The exact nature of the bubble-like features persisting in high magnetic fields was not unambiguously clarified, but we assume that they are related to crystallographic defects, such as anti-phase boundaries (APB) [124], arising in the multivariant growth. Such defects may consequently lead to creation of small areas with antiferromagnetic ordering, whose magnetic signal can persist up to high magnetic fields, as reported for example in magnetite [125]. Crystallographic defects can also act as domain nucleation centers, which indeed was observed by means of MFM.

Fig. 6.9 shows a series of MFM scans taken at 20 K in case of SRO2, where the domain nucleation process is captured. Duration of each scan was approximately 13 minutes. Fig. 6.9(a) shows saturated state measured in remanence after application of +3 T. Weak dark shadow spots, coming from the crosstalk

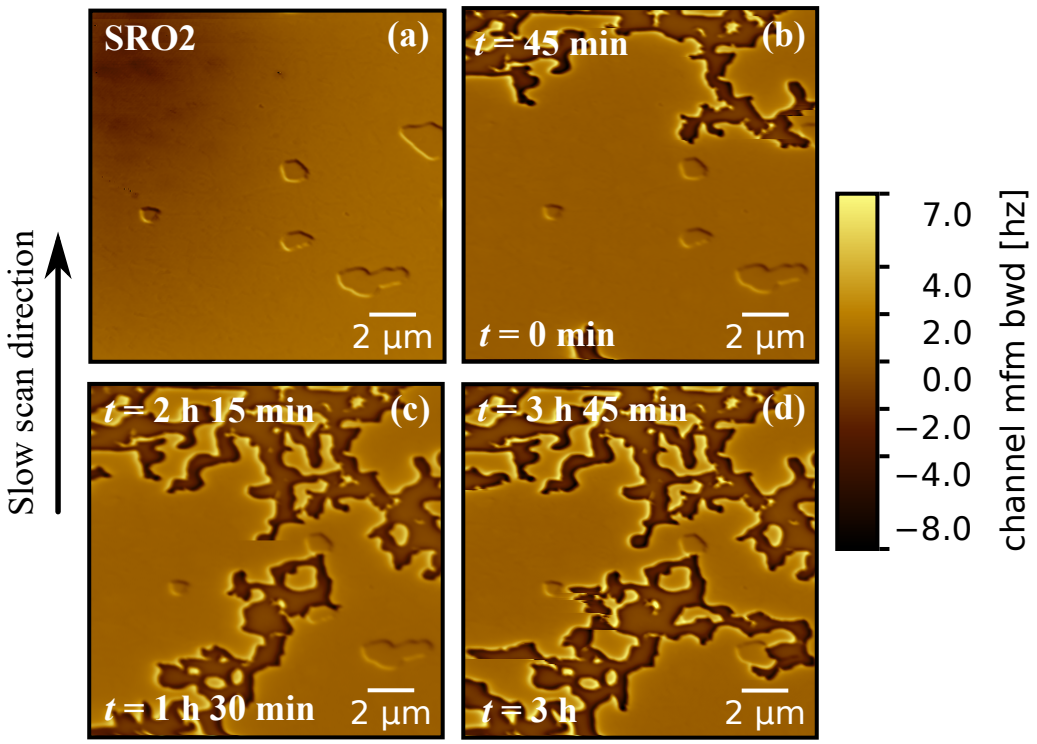

Figure 6.8: MFM images ($15 \times 15\,\mu m^2$) of magnetization reversal in SRO film deposited on STO substrate with low miscut angle ($\sim 0.1°$), measured at 20 K with field applied perpendicular to sample surface. Slow scan direction is indicated by the black arrow. Bright areas represent initial magnetization, dark areas are reversed. (a) Remanent state after saturation at +5 T, (b) first scan at -151 mT, (c) one of the following scans at -151 mT measured after more than 2 hours, (d) last scan at -151 mT after nearly 4 hours, where further magnetization switching is still visible. The time after field application is indicated for the beginning (bottom) and the end (top) of each scan

of topography (cf. Fig. 6.2(b)), are visible all over the investigated area. Several bubble-like features, that were not erased by the saturation field of +3 T, can be observed as well. Two of them indicated by arrows become domain nucleation centers as demonstrated in Fig. 6.9(b) after application of small negative field of -140 mT. The dark magnetic domains are clearly originating in the persistent features. Next scan in Fig. 6.9(c) taken after 52 minutes shows again the evolution of magnetization with time, which now however is not so extensive due to lower value of the applied magnetic field. Nonetheless timescale of the magnetization relaxation process is always in order of hours as demonstrated in Fig. 6.9(d), taken after 2 hours from the initial field application, where further magnetization evolution is still visible.

Fig. 6.10 shows a single scan of SRO2 taken at a higher negative field of $-180\,mT$. The scan was measured right after the field application, but here we do not want to discuss the dynamics. We want to point out that more than a half of the area is already reversed, which means that the overall magnetic moment of the sample should be negative. However this scan was taken at a field value determined as coercive field according to the SQUID magnetometry. This disagreement between MFM and SQUID points out the local character of the

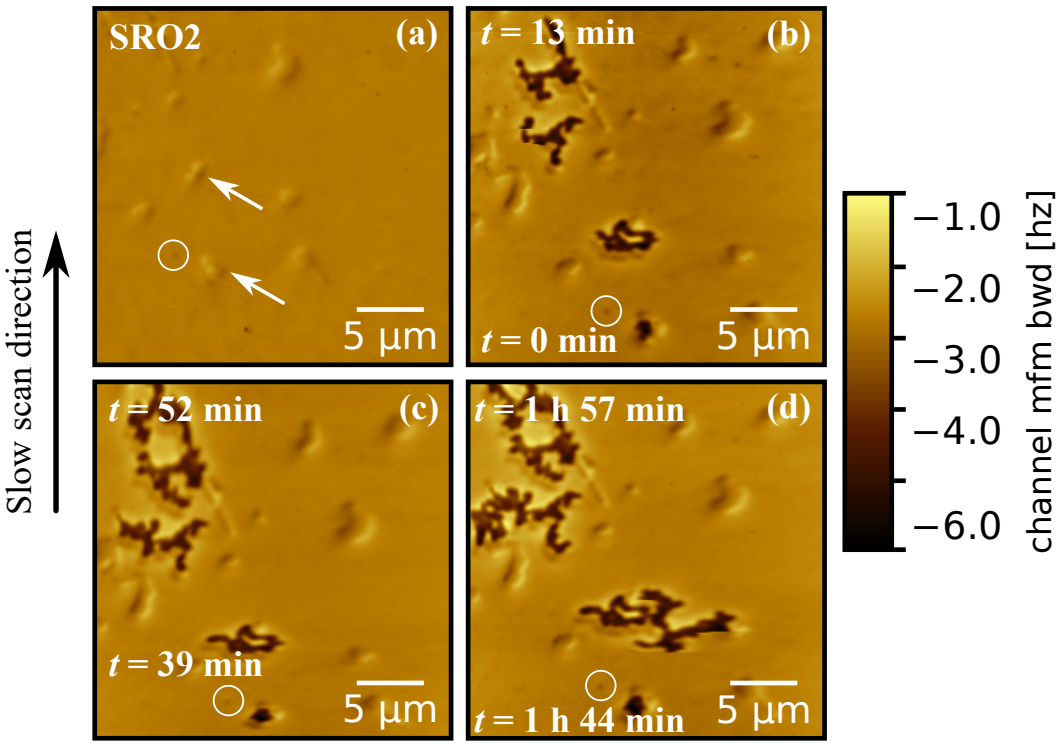

Figure 6.9: MFM images ($26 \times 26\ \mu m^2$) of magnetization reversal in SRO film deposited on STO substrate with low miscut angle ($\sim 0.1°$), measured at 20 K with field applied perpendicular to sample surface. Slow scan direction is indicated by the black arrow. Bright areas represent initial magnetization, dark areas are reversed. (a) Fully magnetized state measured in remanence after saturation in +3 T, (b) first scan at -140 mT where domain nucleation is captured, (c) one of the following scans at -140 mT measured after 52 minutes, (d) last scan at -140 mT after nearly 2 hours. White circle in all images highlights a dirt particle that serves as a marker. White arrows in (a) indicate bubble-like features acting as domain nucleation centers. The time after field application is indicated for the beginning (bottom) and the end (top) of each scan.

MFM measurement, as only a small area of the sample can be measured during the scan. Nevertheless, despite the quantitative inaccuracy of the MFM, conclusions on behaviour of magnetic domains remain unequivocal.

As demonstrated in Fig. 6.9, in case of SRO2 we were able to observe the domain nucleation process, which enabled determination of the nucleation centers. On the other hand this was not possible in case of SRO1, where we did not succeed in capturing the exact location of the nucleation centers. As already presented earlier, in Fig. 6.7(b) we captured the very beginning of the switching process, yet a clearly demarcated area indicating a nucleation center is not visible. The reversed (dark) area is missing borders on the left and top edge of the image, suggesting that the domain nucleated outside of the observed area. In order to locate the domain nucleation centers, we tried to find one clearly demarcated reversed domain by observing a larger area of the sample. We first measured a single MFM scan at a small negative field of -117 mT where a switching event appeared. Then we turned off the magnetic field to prevent further propagation

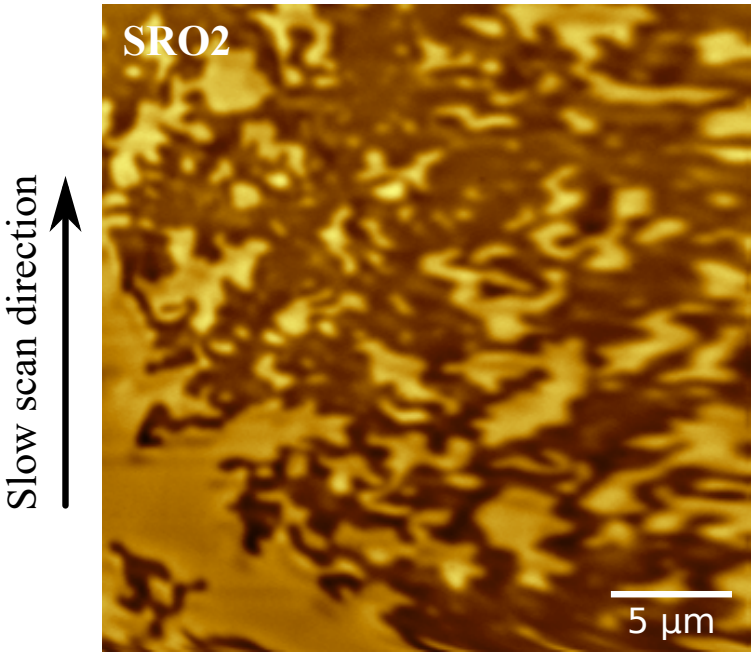

Figure 6.10: MFM image ($26 \times 26\,\mu m^2$) of SRO film deposited on STO substrate with low miscut angle ($\sim 0.1°$), measured at 20 K with field of -180 mT applied perpendicular to sample surface.

of magnetic domains and we moved with the scanner around the area of the sample to find borders of the initially observed reversed domain. This way we investigated area of 90×90 squared micrometers as shown in Fig. 6.11. However, we were not able to find borders of the reversed region, i.e. we did not locate the domain nucleation centers.

We should mention that one can also made an alternative explanation for the process depicted in Fig. 6.7. If we assume that the domain nucleated in the very center of Fig. 6.7(b), and that the reversal process then occured very quickly, it would be possible that the DWs propagated from the center beyond the image borderds before the scan was finished. In order to test this hypothesis we performed several control measurements in a following sequence. Firstly, we saturated the sample in a high positive field, and we applied small negative field (e.g. -120 mT) to initiate the nucleation process, after which we captured a first image. Secondly, we saturated the sample in a high positive field again, and then we applied a small negative field of lower amplitude compared to the first measurement (e.g. -115 mT). Now we captured a second image and compared the domain pattern with the first image. As the second image was recorded at lower field, the reversed area should be smaller compared to the first image, allowing us to determine the direction of DW propagation, as well as the position of the nucleation center. If the nucleation center were located in the middle of the observed area, the DWs would propagate from the middle, and the reversed area would be diminished at the borders. However, the measurements revealed the exact opposite, i.e. the reversed area was significantly diminished in the middle, suggesting that the DW propagation was proceeding from outside into the investigated area. This leaves the alternative hypothesis highly unlikely. The domain nucleation center always appeared to be located outside the observed area. To-

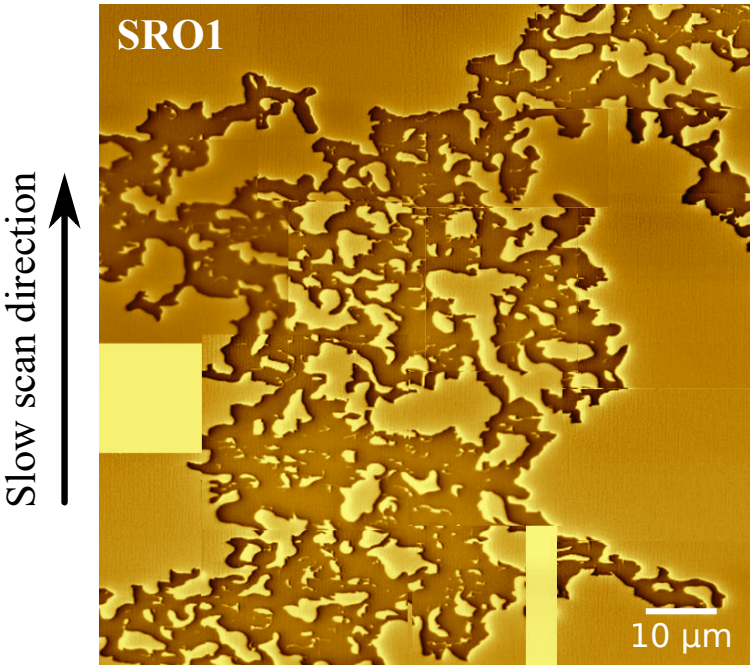

Figure 6.11: MFM image ($90 \times 90\ \mu m^2$) of SRO film deposited on vicinal STO substrate, composed of several $26 \times 26\ \mu m^2$ scans taken at 20 K, at remanence after initiation of the switching process with field of -117 mT perpendicular to the sample surface. The two bright rectangles are missing parts.

gether with the findings from Fig. 6.11, it leaves us unable to determine the exact position of domain nucleation centers.

Not being able to capture the domain nucleation in SRO1 indicates significantly lower density of the nucleation centers in SRO prepared on vicinal STO substrate. Properties of the magnetic domains are also different between the two films. SRO1 exhibits larger magnetic domains and smaller coercive field, which both indicate lower density of pinning centers in SRO on vicinal substrate. The lower density of both the pinning and the nucleation centers is likely to be related to density of crystallographic defects. Presence of the defects is apparently suppressed in SRO on vicinal substrate via suppression of the multi-variant growth. Even though we did not achieve growth of purely single-variant SRO film, the representation of second crystallographic variant in case of SRO1 is so low that the magnetic properties are notably improved. Absence of the bubble-like features in MFM measurements on SRO1 further support their relation to crystallographic defects, such as APB, which are typically reported in SRO thin films [126, 127, 128]. APB can lead to antiferromagnetic ordering inducing magnetic signal that can persist up to high magnetic fields [125]. Even though there are no MFM reports on similar behaviour in SRO films, a recent study reported almost identical MFM features arising near APB in bulk Ni-Mn-Ga [129]. We can therefore conclude that growth of SRO on vicinal STO substrate leads to reduced density of crystallographic defects acting as domain nucleation centers, such as APB, and consequently to significantly improved magnetic properties of the films.

6.3.2 Magneto-optical Kerr microscopy

In order to confirm validity of our MFM results we performed several spatially resolved measurements on SRO1 magnetization by means of MOKE microscopy. We used a homemade Kerr microscope with an orange diode as a light source. As we were not able to apply magnetic field higher than $\sim$ 20 mT, the measurements were carried out at higher temperature, where the coercive field was sufficiently reduced to allow the magnetization reversal.

Fig. 6.12 shows Kerr microscopy image of SRO1 taken at 135 K and 20 mT of magnetic field applied perpendicular to the sample surface. Circular and oval spots are visible all over the image area. These are only dust particles on the CCD detector and do not carry any important information. The magnetic domain pattern can be clearly observed and the domain size and shape are in full agreement with the domain parameters observed by MFM (cf. Fig. 6.11), which verifies the qualitative results of the MFM measurements.

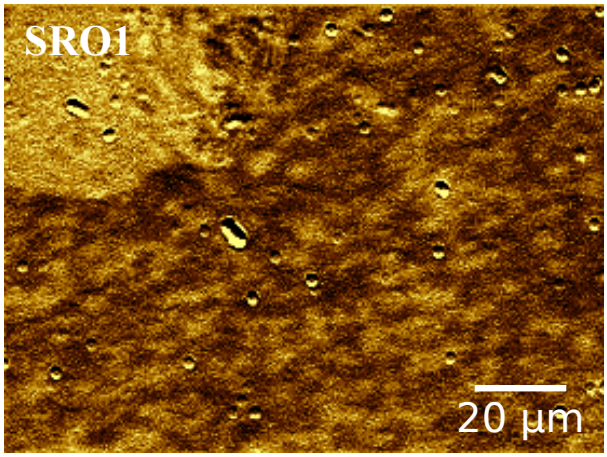

Figure 6.12: MOKE microscopy image (128×96 μm^2) of SRO film deposited on vicinal STO substrate, measured at 135 K and 20 mT of magnetic field applied perpendicular to the sample surface.

Conclusion

Due to the high importance for applications in oxide electronics, two groups of magnetic oxides were investigated in this work.

Firstly, we presented a systematic study of the influence of epitaxial strain on magnetic and magneto-optical properties of LSMO ultrathin films. To begin with, we applied the strain statically by use of several substrates with different lattice mismatch. Both SQUID magnetometry and MOKE spectroscopy confirmed deterioration of magnetic properties with increasing epitaxial strain, which can be explained by both the increasing unit cell distortion of the films and the magnetically inert layer. By combination of spectroscopic ellipsometry and MOKE spectroscopy we determined the diagonal and off-diagonal elements of permittivity tensor. The spectra of the off-diagonal elements confirmed presence of previously reported electronic transitions around 2.4 and 3.6 eV. A third electronic transition was observed around 4.3 eV only in spectra of films grown under compressive strain. We proposed classification of this transition as crystal field paramagnetic transition from Mn t_{2g} to Mn e_g levels. We further performed *ab initio* calculations that justified this classification and manifested a minor influence of OOR in comparison to major role of octahedra distortions in determining magneto-optical properties of LSMO. We therefore demonstrated sensitivity of Mn $3d$ levels to oxygen octahedra distortions, which leads to potential ways of tuning the magneto-optical properties of ultrathin LSMO films in future applications.

We further tried to apply the strain dynamically by use of piezoelectric underlayer. Even though structural and optical characterization confirmed proper physical properties of the fabricated device, the magneto-optical measurements revealed very small influence of applied voltage on resulting spectral behaviour of Kerr rotation. We showed that such a small effect can be more likely explained by change of the PZT layer thickness due to the applied voltage. Therefore the results remain inconclusive and we need to find a way how to transfer the strain from PZT layer in LSMO more effectively.

The second part of the work dealt with the influence of substrate miscut on magnetic domains in ultrathin films of SRO. As expected, structural investigation showed that multi-variant growth can be successfully suppressed by use of vicinal STO substrate, i.e. by substrate of high miscut angle. Even though we did not achieve growth of purely single-variant film, the second SRO variant was represented by negligible fraction in case of the vicinal substrate, compared to 30% in case of the substrate with low miscut angle. By means of SQUID magnetometry and MFM microscopy we investigated the magnetization dynamics and behaviour of the magnetic domains. We found that magnetization relaxation takes place in both films and it is observable on similar timescale of several hours. We further found that the film with higher representation of the second SRO variant exhibits higher coercive field and smaller magnetic domains, which is directly related to higher density of pinning centers, i.e. higher density of crystallographic defects. High density of defects was confirmed also by direct observation of the domain nucleation centers, which are likely to originate due to the enhanced multi-variant growth. We believe that some of the defects are

anti-phase boundaries, leading to antiferromagnetic ordering and persistent features in MFM signal up to high magnetic fields. The qualitative MFM results were further confirmed by MOKE microscopy, which revealed essentially identical magnetic domains pattern. Growth of SRO on vicinal STO substrate therefore leads to reduced density of crystallographic defects, i.e. to better overall crystalline quality of the films, and consequenlty to improved magnetic properties of SRO, which is of high importance for further applications.

Résumé en français

Introduction

Dans ce travail, on a systématiquement étudié les propriétés physiques de deux oxydes magnétiques, qui offrent une grande variété d'applications dans l'éléctronique d'oxydes.

Le manganite dopé au strontium $La_{2/3}Sr_{1/3}MnO_3$ (LSMO) est un matériau très connu grâce à sa combinaison unique des propriétés physiques. Il présente l'effet de magnétorésistance colossale [1], presque 100 % polarisation en spin [3] et une haute température de Curie ($T_{C,bulk} \sim 370$ K) [2].

Le ferromagnétisme de LSMO est déterminé par le double échange, qui dépend fortement sur la géométrie de la liaison Mn-O-Mn. Le facteur qui est donc très important à la contrôle des propriétés magnétiques de LSMO est la contrainte épitaxiale.

Dans ce travail, on a effectué l'étude de l'influence de la contrainte, qui a été appliqué dans la façon statique et dynamique. L'utilisation de l'approche dynamique a été motivé par le succès de la contrôle de l'inversion de l'aimentation dans un nanofil de la vanne de spin, réalisé par l'aid d'une sous-couche piézoélectrique [6] comme montré en Fig. 1.

Un autre oxyde magnétique ($T_{C,bulk} \sim 160$ K [7]) très connu est le ruthénate de strontium $SrRuO_3$ (SRO). Une combinaison de la grande conductivité électrique et presque idéale croissance épitaxiale est la raison pour la popularité de SRO à la fabrication d'électrodes dans les hétérostructures d'oxydes [8].

Malgré plusiers décennies des études, il y a toujours des questions concernant l'anisotropie magnétique de SRO [8]. Mais la connaissance exacte du comportement magnétique est très important grâce aux nouvelles applications de SRO dans le domaine de spintronique [14, 15, 16, 17, 18].

La croissance de SRO sur le substrat de $SrTiO_3$ (STO) est possible dans six divers orientations cristallographiques, soi-disant variants [19, 20]. La croissance de plusiers variants peut être supprimée par la désorientation du substrat, ce qui mène aux couches minces de SRO de haute qualité. Dans ce travail, on a étudié l'influence de la désorientation du substrat par rapport à la dynamique de

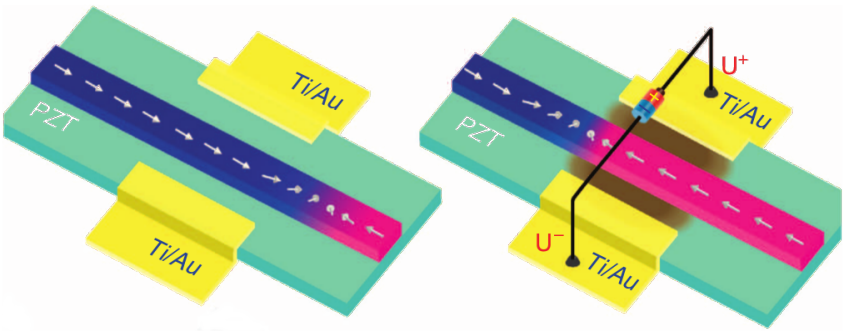

Figure 1: Schéma de l'inversion de l'aimentation dans un nanofil de la vanne de spin, contrôlée dynamiquement par la contrainte à l'aide de tension externe sur une sous-couche piézoélectrique (extrait de [6]).

l'aimantation dans le SRO.

1 Propriétés structurales et magnétiques des couches ultraminces des oxydes

La structure cristalline d'oxydes magnétiques est la structure pérovskite cubique - ABO_3, comme presenté en Fig. 2. Les atomes B sont entourés de six atomes d'oxygène formant ainsi un octaèdre BO_6, qui est un élément structural très important dans les matériaux pérovskites. Les rotations et distorsions d'octaèdres d'oxygène sont deux mécanismes qui peuvent influencer les propriétés physiques de ces matériaux. Les rotations d'octaèdres sont caractérisées par la modification de l'angle de la liaison Mn-O-Mn, tandis que les distorsions sont décrit par la variation de la longeur de Mn-O.

Ces deux méchanisms influencent directement la configuration orbitale [21, 37, 38], ce qui mène aux effects sur les propriétés magnétiques et de transfert [57, 58, 59, 60, 63].

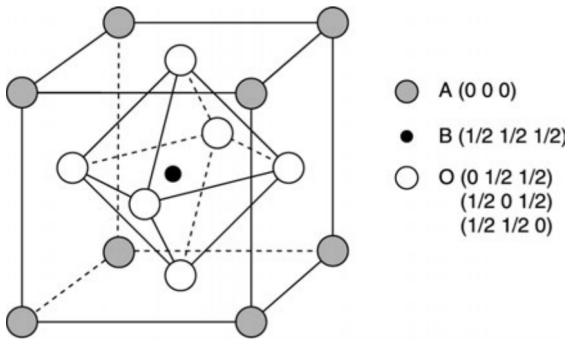

Figure 2: Schéma d'une maille pérovskite idéale ABO_3 (extrait de [21]). Les six atomes autour du cation B représentent un octaèdre BO_6.

2 La théorie élémentaire de la polarisation et des éffets magnéto-optiques

La lumière est une onde électromagnétique. On peut décrire ses propriétés par l'évolution temporelle du vecteur du champ électrique. Ayant la lumière dans la forme d'une onde plane monochromatique, on peut exprimer le vecteur du champ électrique comme

$$\boldsymbol{E} = E_x\boldsymbol{x} + E_y\boldsymbol{y} + E_z\boldsymbol{z}, \qquad E_i = A_{0i}\cos(\omega t + \delta_i), \qquad i = x, y, z, \tag{6.1}$$

où les vecteurs unitaires $\boldsymbol{x}, \boldsymbol{y}$ et $\boldsymbol{z}$ forment la base de système de coordonnées cartésienne. Les grandeurs A_{0i} et δ_i représentent l'amplitude et la phase des oscillations harmoniques selon l'axe correspondant, ω est la fréquence angulaire de l'onde. On peut montrer [69] que le vecteur du champ électrique trace une ellipse, autrement dit le cas le plus général de la polarisation de la lumière est la polarisation elliptique.

L'effet Kerr magnéto-optique (MO) étudie le changement de l'état de polarisation en réflexion d'un échantillon magnétiquement ordonné et optiquement anisotrope. On peut caractériser ce changement par le ratio des coefficients de réflexion. L'angle complex de l'effet Kerr en incidence normale est défini comme

$$\Phi_K = -\frac{r_{ps}}{r_{ss}} \approx \theta_K - i\epsilon_K, \tag{6.2}$$

où r_{ps} et r_{ss} sont les coefficients de réflexion du p-polarisé et du s-polarisé composant de l'onde incidente et reflété, θ_K et ϵ_K représentent les angles magnéto-optiques de la rotation et l'ellipticité Kerr.

Le tenseur de permittivité est un moyen qui nous permet d'introduire la réalité physique à la definition élémentaire de l'angle Kerr. Le tenseur contient des informations sur les propriétés matérielles du système étudié. La connaissance complete du tenseur de permittivité mène à la solution d'équation des ondes, et donc aux coefficients de réflexion qui servent au calcul de l'angle MO par l'éq. (6.2). Le tenseur de permittivité $\boldsymbol{\varepsilon}$ dans la configuration polaire (le champ magnétique est perpendiculaire à la surface de l'échantillon) et presque normale incidence de la lumière peut être exprimé comme

$$\boldsymbol{\varepsilon} \approx \begin{bmatrix} \varepsilon_1 & -i\varepsilon_2 & 0 \\ i\varepsilon_2 & \varepsilon_1 & 0 \\ 0 & 0 & \varepsilon_1 \end{bmatrix}, \tag{6.3}$$

donc le tenseur a seulement deux éléments complexes independents: l'élément diagonal ε_1 et l'élément non-diagonal ε_2.

Dans la théorie semi-classique, les effects MO proviennent de la séparation des niveaux d'énergie qui participent à ces transitions optiques. Cette séparation vient de l'interaction spin-orbite. Les transitions optiques qui forment la dépendance spectrale des éléments non-diagonaux du tenseur de permittivité (et donc

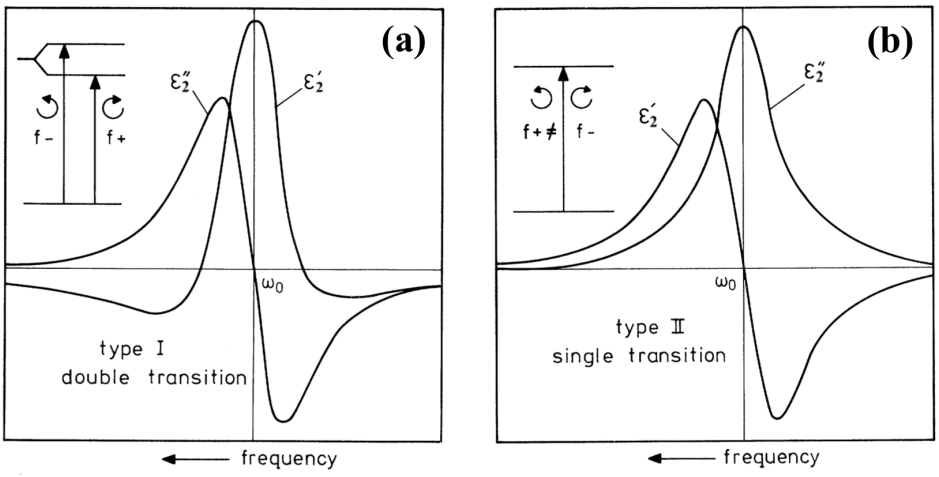

Figure 3: Les formes des raies spectrales de deux types des transitions magnéto-optiques; ω_0 est la fréquence de résonance, $\varepsilon_1^{'}$ et $\varepsilon_2^{''}$ sont les parties réelle et imaginaire de ε_2. (a) Type I, une double ou diamagnétique transition. L'encart montre la séparation spin-orbite des états excités. (b) Type II, une single ou paramagnétique transition. L'encart montre les divers forces f_+ et f_- de l'oscillateur (extrait de [72]).

qui sont magnéto-optiquement actives), peut être triés dans deux catégories, comme presenté en Fig. 3.

La théorie macroscopique du formalisme de Yeh [76] nous permet de faire les calculs de la réponse MO basés sur la connaissance complete du tenseur de permittivité. Ou au contraire, on peut calculer les éléments du tenseur de permittivité si on fait d'abord les mesures expérimentales de la dépendance spectrale de l'effet MO.

3 Dispositifs expérimentaux

Les principaux outils expérimentaux utilisés pendant cette thèse ont été les suivants. Toutes les couches ont été déposées par ablation laser pulsé. La diffraction des rayons X a permis de complètement décrire la cellule unitaire des échantillons étudiés. Les propriétés magnétiques ont été examinées à l'aide de magnétomètre SQUID. Des informations complémentaires sur les propriétés magnétiques ont été fourni par la microscopie à force magnétique (MFM) et la spectroscopie Kerr magnéto-optique. Les propriétés optiques ont été caractérisées par l'aide de l'ellipsométrie spectroscopique. La technique la plus importante a été la spectroscopie magnéto-optique de l'effet Kerr (MOKE).

La spectroscopie Kerr MO est une technique très susceptible pour la caractérisation des propriétés magnétiques des matériaux. Elle peut mesurer les angles MO avec une haute précision ce qui est convenable à étudier des signaux faibles des couches ou multicouches minces. Dans ce travail, on a utilisé un spectromètre MO à l'analyseur tournant, qui est montré en Fig. 4. La lumière émis par la lampe passe d'abord par le polariseur P, qui définit l'état de la polarisation de l'onde lumineuse. Après la réflexion sur la surface de l'échantillon S placé dans un électro-aimant, la lumière passe par le compensateur C et ensuite par l'analyseur tournant A. Enfin elle est enregistrée par le détecteur D. L'intensité de la lumière I varie en fonction de l'angle ξ de l'analyseur tournant selon la formule

$$I = \sin^2 \xi + (\theta_K \cos\delta + \epsilon_K \sin\delta) \sin(2\xi) + I_{\text{dark}}, \tag{6.4}$$

où δ désigne le retard en phase de la lumière induit par le compensateur C, I_{dark}

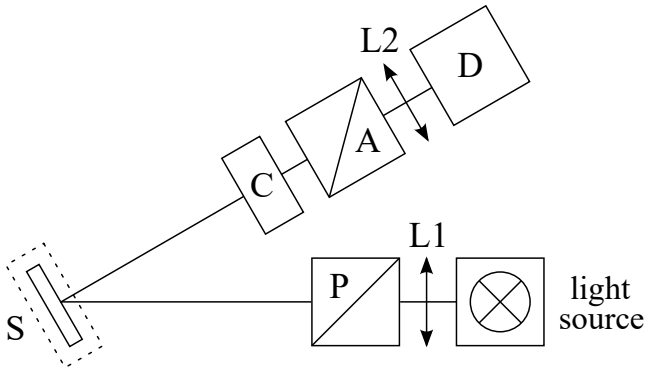

Figure 4: Schéma du spectromètre magnéto-optique basé sur la technique de l'analyseur tournant; A - analyseur tournant, C - compensateur, D - détecteur, L1, L2 - lentilles, P - polariseur, S - échantillon aimanté.

est un terme constant représentant le courant d'obscurité, enfin θ_K et ϵ_K sont les angles MO de la rotation et l'ellipticité Kerr. On peut extraire les angles de la rotation et l'ellipticité Kerr des mesures expérimentaux par l'ajustement de courbe de la dépendence de l'intensité I en fonction de l'angle ξ selon l'éq. (6.4), ayant les angles θ_K et ϵ_K comme les paramètres de l'ajustement.

4 Les échantillons examinés

Tous les échantillons ont été fabriqués au Centre de Nanosciences et de Nanotechnologies à Orsay.

Pour l'application statique de la contrainte, les couches ultraminces de LSMO (avec l'épaisseur environ 20 nm) ont été déposées sur quatre substrats différents - $LaAlO_3$ (LAO), $(LaAlO_3)_{1/3}(Sr_2AlTaO_6)_{2/3}$ (LSAT), STO et $DyScO_3$ (DSO). Ces substrats ont fourni une grande variété des valeurs de la contrainte, allant de la grande contrainte compressive sur LAO à la grande contrainte de traction sur DSO. Les paramètres de maille a et les valuers de la contrainte épitaxiale sont résumés dans le Tableau 1 pour tous les substrats.

Matériel	LAO	LSAT	LSMO	STO	DSO
Paramètre de maille a [Å]	3.790	3.868	3.876	3.905	3.942
Contrainte épitaxiale [%]	2.27	0.21		-0.74	-1.67

Tableau 1: Le sommaire des paramètres de maille a et des valeurs de la contrainte épitaxiale pour tous les substrats utilisés pour le dépôt des couches LSMO.

Pour l'application dynamique de la contrainte, un dispositif a été réalisé par des techniques de microfabrication. Le dispositif a été basé sur une hétérostructure, qui a contenu la couche LSMO au dessus d'une sous-couche piézoélectrique de $PbZr_{0.52}Ti_{0.48}O_3$ (PZT), le schéma du dispositif est presenté en Fig. 5.

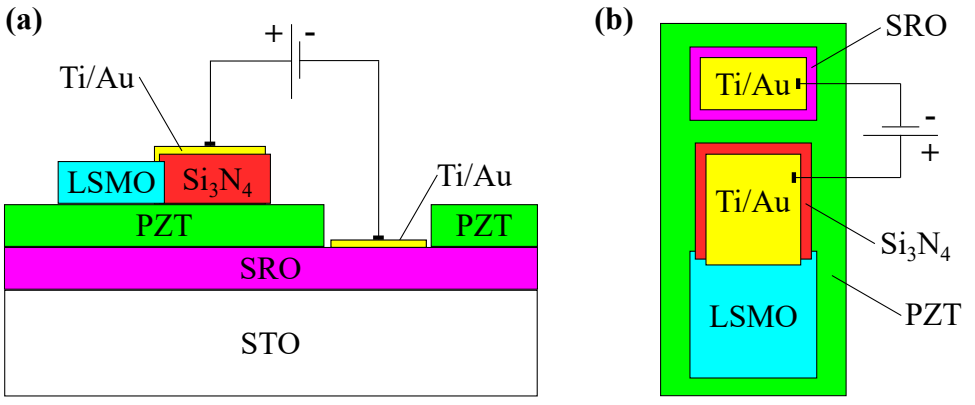

Figure 5: (a) Schéma du profil et (b) de la vue de dessus de l'hétérostructure après microfabrication, utilisées comme le dispositif pour l'application dynamique de la contrainte. La tension éléctrique a été appliquée dans la direction perpendiculaire par rapport à la surface de la multicouche.

Afin d'étudier l'influence de la désorientation du substrat par rapport à la dynamique de l'aimantation de SRO, on a fabriqué deux couches minces sur les

substrats de STO avec les valeurs différents de la désorientation α. Des grandes valeurs de la désoriantation ($\alpha \gtrsim 1°$) mènent à la suppression de la croissance de plusiers variants cristallographiques, on a donc utilisé les substrats avec $\alpha = 0.1°$ afin de réaliser la croissance de plusiers variants sur l'un d'échantillons et $\alpha = 1.0°$ afin de fabriquer un seul variant sur l'autre.

5 L'influence de la contrainte sur la structure électronique de $La_{2/3}Sr_{1/3}MnO_3$

5.1 L'application statique de la contrainte

La qualité des couches minces LSMO déposées par ablation laser pulsé a été vérifiée à l'aide de la microscopie à force atomique et la diffraction des rayons X. La cellule unitaire a été complètement décrite en utilisant la cartographie de l'espace réciproque par diffraction des rayons X. Les propriétés magnétiques ont été caractérisées par la magnétometrie SQUID, les propriétés optiques par l'ellipsométrie spectroscopique. Les résultats principaux ont été obtenus par spectroscopie MOKE.

La spectroscopie MOKE a été utilisée afin de déterminer les éléments non-diagonaux du tenseur de permittivité ε_2. Les mesures MOKE à temperature ambiante ont été effectuées par le spectromètre MO à l'analyseur tournant, qui est présenté en Fig. 4. Les données ont été enregistrées dans la configuration polaire à 1 T du champ magnétique (champ suffisant pour la saturation complète), sur la gamme spectrale de 1.5 à 5.0 eV.

Les spectres MOKE ont été usilisés pour calculer les spectres des éléments non-diagonaux du tenseur de permittivité, qui sont montrés en Fig. 6. Les paramètres

Substrat	LAO	LSAT	STO	DSO
Transition 1	Transition du champ cristallin Mn $t_{2g} \rightarrow e_g$			
$(\varepsilon_2^{''})_{max}$	0.010	0.472	0.069	0.001
ω_0 [eV]	2.45	2.50	2.38	2.49
Γ [eV]	0.43	0.66	0.38	0.42
Transition 2	Transition de transfert de charge O $2p \rightarrow$ Mn t_{2g}			
$(\varepsilon_2^{'})_{max}$	0.04	1.16	0.36	0.01
ω_0 [eV]	3.63	3.51	3.55	3.64
Γ [eV]	0.87	1.14	0.97	0.73
Transition 3	Transition du champ cristallin Mn $t_{2g} \rightarrow e_g$			
$(\varepsilon_2^{''})_{max}$	-0.03	-0.69	Pas de transition	
ω_0 [eV]	4.26	4.25	sur la contrainte	
Γ [eV]	0.56	0.67	de traction	

Tableau 2: Les paramètres de trois transitions électroniques qui ont été utilisées pour décrire la réponse magnéto-optique des couches LSMO sur quatre substrats différents; $(\varepsilon_2^{'})_{max}$ ou $(\varepsilon_2^{''})_{max}$, ω_0 et Γ désignent l'amplitude maximale, la fréquence et la largeur des oscillateurs. Les paramètres ont été obtenus par l'ajustement de courbe des spectres MOKE en utilisant les éléments diagonaux du tenseur de permittivité.

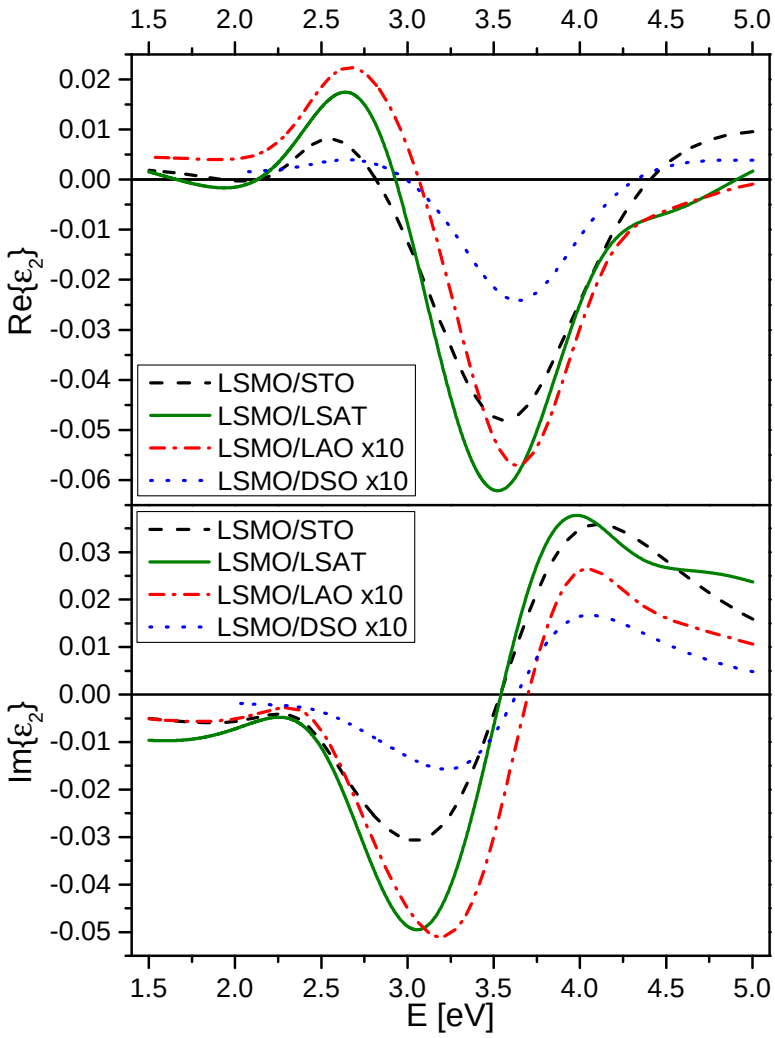

Figure 6: Les spectres des parties réelle (en haut) et imaginaire (en bas) des éléments non-diagonaux du tenseur de permittivité des couches LSMO sur quatre substrats différents. Ils ont été calculés des éléments diagonaux du tenseur de permittivité et des spectres MOKE. Pour plus de clarté, les spectres des couches déposées sur LAO et DSO ont été amplifiés par dix.

des transitions utilisées pour décrire les éléments non-diagonaux sont présentés dans la Tableau 2. Dans les spectres de tous échantillons, on peut voir deux transitions électroniques qui ont été déjà rapportées. Autour de l'énergie de 3.6 eV, il y a le minimum principal qui est associé avec la transition de transfert de charge de O $2p$ à Mn t_{2g} [74, 104, 105, 107]. Autour de 2.4 eV, on peut voir le maximum qui est associé avec la transition du champ cristallin de Mn t_{2g} à Mn e_g [74, 105, 107]. De plus, il y a une autre transition autour de l'énergie de 4.3 eV, mais seulement dans les spectres des échantillons fabriqués avec une contrainte compressive.

Basé sur l'étude de LSMO par la spectroscopie MOKE dépandante de la température [110] on a proposé la classification de cette transition comme une transition paramagnétique du champ cristallin de Mn t_{2g} à Mn e_g. Cette classification conforme aux calculs *ab initio* de densité d'états électroniques rapportés précédemment [107, 111, 112]. Nos calculs de densité d'états électroniques ont

ensuite conforté cette classification. De plus, les calculs ont montré un rôle mineur des rotations d'octaèdres d'oxygène comparé au rôle majeur des distorsions d'octaèdres par rapport à la contrôle des propriétés MO de LSMO.

5.2 L'application dynamique de la contrainte

La qualité du dispositif LSMO/PZT a été verifiée par les mesures des propriétés structurales, ferroélectriques, optiques et magnéto-optiques ainsi que par les calculs théoriques de la réponse MO. Les résultats principaux ont été obtenus par la spectroscopie MO et ils sont presentés en Fig. 7. Il y a deux courbes qui montrent la réponse MO du dispositif mesurée à 0 V et 4 V de la tension éléctrique appliquée à travers de la couche PZT. La différence de ces mesures est montrée et pour plus de clarté elle est amplifiée par dix. Basé sur les calculs théoriques de la réponse MO du dispositif, on a proposé que l'effet du changement de la rotation Kerr est si faible qu'il vient probablement de l'interférence optique du signal MO, venant du changement de l'épaisseur de la couche PZT causée par la tension éléctrique. Donc l'application dynamique de la contrainte est restée peu concluante. Des améliorations ultérieures du dispositif sont nécessaires pour atteindre un meilleur transfert de la contrainte entre les couches LSMO et PZT.

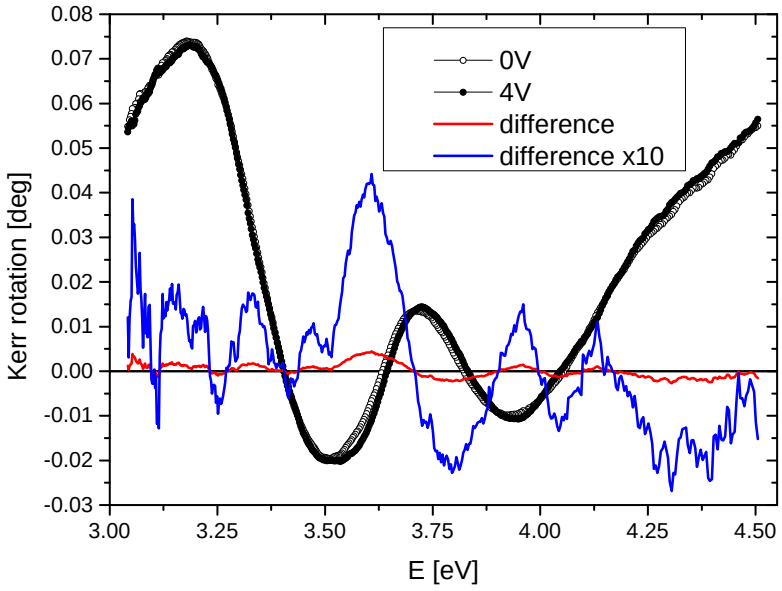

Figure 7: Le spectre de la rotation Kerr du dispositif LSMO/PZT pour 0 V et 4 V de la tension éléctrique appliquée à travers de la couche PZT, mesuré dans la configuration polaire à l'angle d'incidence de 60°. La différence des deux mesures est montrée.

6 L'influence de la désorientation du substrat sur l'aimantation de $SrRuO_3$

Les propriétés structurales des couches SRO ont été caractérisées par la cartographie de l'espace réciproque par diffraction des rayons X. Comme attendu, on a

trouvé que le grand angle de désorientation mène à la suppression de la croissance de plusiers variants, donc on a réalisé une couche SRO avec un seul variant (SRO1) et une couche SRO avec deux types de variant (SRO2).

Les propriétés magnétiques ont été d'abord caractérisées par la magnétometrie SQUID. On a trouvé qu'il y a des différences dans le cycle d'hystérésis des deux échantillons, notamment que dans le SRO1 le champ coercitif est plus petit et l'aimantation de saturation est plus grande que dans le SRO2.

Les résultats principaux ont été obtenus par la microscopie à force magnétique qui a servi à la caractérisation du comportement des domaines magnétiques. La température de Curie de SRO est environ 160 K, donc les mesures de MFM ont été effectuées en basses températures, plus précisément à 20 K. Une série typique des images MFM de SRO1 est presentée en Fig. 8. On peut voir la morphologie des domaines magnétiques ainsi que leur comportement dynamique. De la comparaison des images des deux échantillons, on a trouvé que la présence de plusiers variants mène à l'augmentation de la densité de défauts agissant comme points

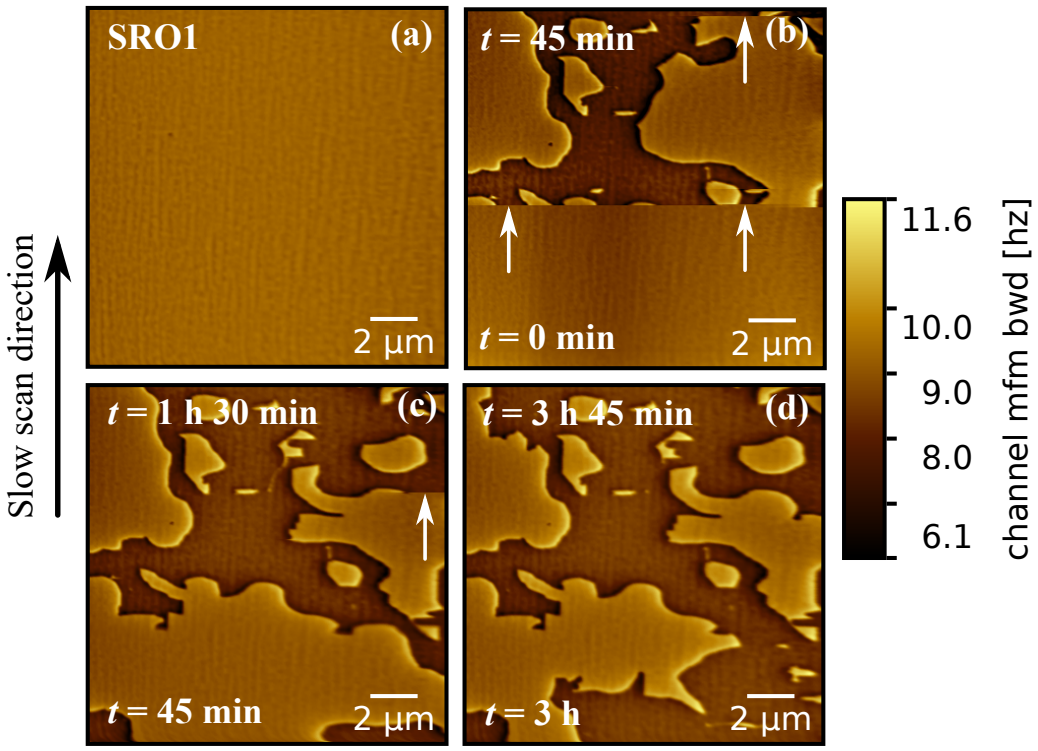

Figure 8: Images MFM ($15 \times 15\ \mu m^2$) de l'inversion de l'aimentation dans la couche SRO déposée sur le substrat STO vicinal ($\alpha = 1.0°$), mesurées à 20 K du champ appliqué dans la direction perpendiculaire à la surface de l'échantillon. La direction du balayage est montrée par la flèche noire. (a) L'état à la saturation totale, mesuré à +3 T, (b) le premier balayage à -119 mT, où on peut voir le début du processus de l'inversion, (c) le deuxième balayage à -119 mT, mesuré juste après le premier, (d) le dernier balayage à -119 mT après presque 4 heures, où on peut toujours voir l'inversion continuante. Les flèches blanches dans (b) et (c) surlignent les lignes horizontales entre les régions claires (initiales) et noires (inversées) qui viennent de l'inverser pendant le balayage. Le temps après l'application du champ est indiqué pour le début (en haut) et la fin (en bas) de chaque balayage.

d'ancrage ou de nucléation pour les domaines magnétiques.

Conclusion

Deux groupes d'oxydes mangétiques ont été étudiés dans ce travail grâce à leur haute importance pour les applications dans l'éléctronique d'oxydes.

En premier lieu, on a presenté une étude systématique de l'influence de la contrainte épitaxiale sur les propriétés magnétiques et magnéto-optiques des couches minces de LSMO. D'abord on a appliqué la contrainte statiquement à l'aide de plusiers substrats différents qui ont fourni une grande variété des valeurs de la contrainte. La magnétometrie SQUID et la spectrocopie MOKE ont confirmé la détérioration des propriétés magnétiques en augmentation de la valeur de la contrainte. La combinaison de l'ellipsométrie spectroscopique et la spectroscopie MOKE a servi à déterminer les spectres des éléments diagonaux et non-diagonaux du tenseur de permittivité. Les spectres non-diagonaux ont confirmé la présence de deux transitions déjà rapportées autour des énergies de 2.4 et 3.6 eV. Une autre transition éléctronique autour de 4.3 eV a été trouvée seulement dans les spectres des couches déposées avec la contrainte compressive. On a proposé la classification de cette transition comme une transition paramagnétique du champ cristallin de Mn t_{2g} à Mn e_g. Les calculs *ab initio* ont conforté cette classification et ils ont révélé le rôle mineur des rotations d'octaèdres d'oxygène comparé au rôle majeur des distorsions d'octaèdres par rapport à la contrôle des propriétés magnéto-optiques de LSMO. L'application dynamique de la contrainte à l'aide d'une sous-couche piézoélectrique a montré un changement faible du spectre de la rotation Kerr, ce qui a donc resté peu concluant, nécessitant des améliorations ultérieures du dispositif LSMO/PZT pour un meilleur transfert de la contrainte entre la sous-couche piézoélectrique et la couche LSMO.

En second lieu, l'influence de la désorientation du substrat a été édutiée par rapport au comportement des domaines magnétiques des couches minces de SRO. Comme attendu, on a montré que l'emploi d'un substrat vicinal (avec un grand angle de la désorientation) mène à la suppression de la croissance de plusiers variants cristallographiques de SRO. La magnétometrie SQUID et la microscopie à force magnétique ont été utilisées à étudier la dynamique de l'aimantation et des domaines magnétiques. On a trouvé que la présence de plusiers variants cristallographiques mène à un champ coercitif plus grand et une aimantation de saturation plus petite, ce qui est directement lié à une densité plus haute des points d'ancrage, c'est à dire la densité plus haute des défauts cristallographiques. On a donc montré que l'emploi d'un substrat vicinal mène à la réduction de la densité de défauts agissant comme points d'ancrage ou de nucléation pour les domaines magnétiques et alors que le substrat vicinal est très important pour la fabrication des couches ultraminces de SRO de haute qualité et d'excellentes propriétés magnétiques.

Bibliography

[1] R. von Helmolt, J. Wecker, B. Holzapfel, L. Schultz, and K. Samwer. Giant negative magnetoresistance in perovskitelike $La_{2/3}Ba_{1/3}MnO_x$ ferromagnetic films. *Physical Review Letters*, 71(14):2331–2333, October 1993.

[2] G. H. Jonker and J. H. Van Santen. Ferromagnetic compounds of manganese with perovskite structure. *Physica*, 16:337–349, March 1950.

[3] M. Bowen, M. Bibes, A. Barthelemy, J.-P. Contour, A. Anane, Y. Lemaitre, and A. Fert. Nearly total spin polarization in $La_{2/3}Sr_{1/3}MnO_3$ from tunneling experiments. *Applied Physics Letters*, 82(2):233–235, 2003.

[4] Clarence Zener. Interaction between the *d*-Shells in the Transition Metals. II. Ferromagnetic Compounds of Manganese with Perovskite Structure. *Physical Review*, 82:403–405, 1951.

[5] James M. Rondinelli, Steven J. May, and John W. Freeland. Control of octahedral connectivity in perovskite oxide heterostructures: An emerging route to multifunctional materials discovery. *MRS Bulletin*, 37(3):261?270, 2012.

[6] Na Lei, Thibaut Devolder, Guillaume Agnus, Pascal Aubert, Laurent Daniel, Joo-Von Kim, Weisheng Zhao, Theodossis Trypiniotis, Russell P. Cowburn, Claude Chappert, Dafine Ravelosona, and Philippe Lecoeur. Strain-controlled magnetic domain wall propagation in hybrid piezoelectric/ferromagnetic structures. *Nature Communications*, 2013.

[7] Akio Kanbayasi. Magnetic properties of $SrRuO_3$ single crystal. *Journal of the Physical Society of Japan*, 41(6):1876–1878, 1976.

[8] Gertjan Koster, Lior Klein, Wolter Siemons, Guus Rijnders, J. Steven Dodge, Chang-Beom Eom, Dave H. A. Blank, and Malcolm R. Beasley. Structure, physical properties, and applications of $SrRuO_3$ thin films. *Rev. Mod. Phys.*, 84:253–298, Mar 2012.

[9] G. Herranz, B. Martinez, J. Fontcuberta, F. Sanchez, M. V. Garcia-Cuenca, C. Ferrater, and M. Varela. $SrRuO_3/SrTiO_3/SrRuO_3$ heterostructures for magnetic tunnel junctions. *Journal of Applied Physics*, 93(10):8035–8037, 2003.

[10] D. C. Worledge and T. H. Geballe. Negative spin-polarization of $SrRuO_3$. *Phys. Rev. Lett.*, 85:5182–5185, Dec 2000.

[11] K. S. Takahashi, A. Sawa, Y. Ishii, H. Akoh, M. Kawasaki, and Y. Tokura. Inverse tunnel magnetoresistance in all-perovskite junctions of $La_{0.7}Sr_{0.3}MnO_3/SrTiO_3/SrRuO_3$. *Phys. Rev. B*, 67:094413, Mar 2003.

[12] G. Kurij. *Magnetic tunnel junctions for ultrasensitive all-oxide hybrid sensors for medical applications*. PhD thesis, University Paris-Saclay, 2016.

[13] Michael Feigenson, James W. Reiner, and Lior Klein. Current-induced magnetic instability in $SrRuO_3$. *Journal of Applied Physics*, 103(7):07E741, 2008.

[14] Michael Feigenson, James W. Reiner, and Lior Klein. Efficient Current-Induced Domain-Wall Displacement in $SrRuO_3$. *Phys. Rev. Lett.*, 98:247204, Jun 2007.

[15] Babusona Sarkar, Biswajit Dalal, and S. K. De. Temperature induced magnetization reversal in $SrRuO_3$. *Applied Physics Letters*, 103(25):252403, 2013.

[16] Yishai Shperber, Daniel Bedau, James W. Reiner, and Lior Klein. Current-induced magnetization reversal in $SrRuO_3$. *Phys. Rev. B*, 86:085102, Aug 2012.

[17] Yishai Shperber, Omer Sinwani, Netanel Naftalis, Daniel Bedau, James W. Reiner, and Lior Klein. Thermally assisted current-induced magnetization reversal in $SrRuO_3$. *Phys. Rev. B*, 87:115118, Mar 2013.

[18] W. P. Zhou, Q. Li, Y. Q. Xiong, Q. M. Zhang, D. H. Wang, Q. Q. Cao, L. Y. Lv, and Y. W. Du. Electric field manipulation of magnetic and transport properties in $SrRuO_3$/$Pb(Mg_{1/3}Nb_{2/3})O_3$-$PbTiO_3$ heterostructure. *Scientific Reports*, 2014.

[19] J. C. Jiang, W. Tian, X. Q. Pan, Q. Gan, and C. B. Eom. Domain structure of epitaxial $SrRuO_3$ thin films on miscut (001) $SrTiO_3$ substrates. *Applied Physics Letters*, 72(23):2963–2965, 1998.

[20] J.C. Jiang, W. Tian, X. Pan, Q. Gan, and C.B. Eom. Effects of miscut of the $SrTiO_3$ substrate on microstructures of the epitaxial $SrRuO_3$ thin films. *Materials Science and Engineering: B*, 56(2):152 – 157, 1998.

[21] A.-M. Haghiri-Gosnet and J.-P. Renard. CMR manganites: physics, thin films and devices. *Journal of Physics D: Applied Physics*, 36:R127–R150, April 2003.

[22] Svatopluk Krupicka. *Fyzika feritu a pribuznych magnetickych kyslicniku.* Academia, Praha, 1. edition, 1969.

[23] A. Vailionis, H. Boschker, W. Siemons, E. P. Houwman, D. H. A. Blank, G. Rijnders, and G. Koster. Misfit strain accommodation in epitaxial ABO_3 perovskites: Lattice rotations and lattice modulations. *Phys. Rev. B*, 83:064101, Feb 2011.

[24] Warren E. Pickett and David J. Singh. Electronic structure and half-metallic transport in the $La_{1-x}Ca_xMnO_3$ system. *Physical Review B*, 53(3):1146–1160, January 1996.

[25] Q. Gan, R. A. Rao, C. B. Eom, L. Wu, and F. Tsui. Lattice distortion and uniaxial magnetic anisotropy in single domain epitaxial (110) films of $SrRuO_3$. *Journal of Applied Physics*, 85(8):5297–5299, 1999.

[26] John B. Goodenough. Theory of the role of covalence in the perovskite-type manganites [La, M(II)]MnO_3. *Physical Review*, 100(2):564–573, October 1955.

[27] A. Khapikov, L. Uspenskaya, I. Bdikin, Ya. Mukovskii, S. Karabashev, D. Shulyaev, and A. Arsenov. Magnetic domains and twin structure of the $La_{0.7}Sr_{0.3}MnO_3$ single crystal. *Applied Physics Letters*, 77(15):2376–2378, 2000.

[28] M. Konoto, T. Kohashi, K. Koike, T. Arima, Y. Kaneko, Y. Tomioka, and Y. Tokura. Magnetic domain structure of a $La_{0.7}Sr_{0.3}MnO_3$ (001) surface observed by a spin-polarized scanning electron microscope. *Applied Physics Letters*, 84(13):2361–2363, 2004.

[29] S. N. Ruddlesden and P. Popper. The compound $Sr_3Ti_2O_7$ and its structure. *Acta Crystallographica*, 11(1):54–55, Jan 1958.

[30] C. W. Jones, P. D. Battle, P. Lightfoot, and W. T. A. Harrison. The structure of $SrRuO_3$ by time-of-flight neutron powder diffraction. *Acta Crystallographica Section C*, 45(3):365–367, Mar 1989.

[31] Y. Maeno, H. Hashimoto, K. Yoshida, S. Nishizaki, T. Fujita, J. G. Bednorz, and F. Lichtenberg. Superconductivity in a layered perovskite without copper. *Nature*, December 1994.

[32] Hugh Simons, John Daniels, Wook Jo, Robert Dittmer, Andrew Studer, Maxim Avdeev, Jurgen Rodel, and Mark Hoffman. Electric-field-induced strain mechanisms in lead-free 94%$(Bi_{1/2}Na_{1/2})TiO_3$-6%$BaTiO_3$. *Applied Physics Letters*, 98(8):082901, 2011.

[33] A. M. Glazer. The classification of tilted octahedra in perovskites. *Acta Crystallographica Section B*, 28(11):3384–3392, Nov 1972.

[34] P. M. Woodward. Octahedral Tilting in Perovskites. I. Geometrical Considerations. *Acta Crystallographica Section B*, 53(1):32–43, Feb 1997.

[35] P. M. Woodward. Octahedral Tilting in Perovskites. II. Structure Stabilizing Forces. *Acta Crystallographica Section B*, 53(1):44–66, Feb 1997.

[36] Arturas Vailionis, Hans Boschker, Evert Houwman, Gertjan Koster, Guus Rijnders, and Dave H. A. Blank. Anisotropic stress relief mechanism in epitaxial $La_{0.67}Sr_{0.33}MnO_3$ films. *Applied Physics Letters*, 95(15):152508, 2009.

[37] C. Aruta, G. Ghiringhelli, A. Tebano, N. G. Boggio, N. B. Brookes, P. G. Medaglia, and G. Balestrino. Strain induced x-ray absorption linear dichroism in $La_{0.7}Sr_{0.3}MnO_3$ thin films. *Phys. Rev. B*, 73:235121, Jun 2006.

[38] C. Aruta, G. Balestrino, A. Tebano, G. Ghiringhelli, and N. B. Brookes. Cooperative enhancement of in-plane orbital ordering by oxygen deficiency and in-plane tensile strain in $La_{0.7}Sr_{0.3}MnO_{3-\delta}$ thin films. *EPL (Europhysics Letters)*, 80(3):37003, 2007.

[39] A. Tebano, C. Aruta, S. Sanna, P. G. Medaglia, G. Balestrino, A. A. Sidorenko, R. De Renzi, G. Ghiringhelli, L. Braicovich, V. Bisogni, and N. B. Brookes. Evidence of Orbital Reconstruction at Interfaces in Ultrathin $La_{0.67}Sr_{0.33}MnO_3$ Films. *Physical Review Letters*, 100(13):137401, April 2008.

[40] A. Tebano, A. Orsini, P. G. Medaglia, D. Di Castro, G. Balestrino, B. Freelon, A. Bostwick, Young Jun Chang, G. Gaines, E. Rotenberg, and N. L. Saini. Preferential occupation of interface bands in $La_{2/3}Sr_{1/3}MnO_3$ films as seen via angle-resolved photoemission. *Physical Review B*, 82(21):214407, December 2010.

[41] M. Huijben, L. W. Martin, Y.-H. Chu, M. B. Holcomb, P. Yu, G. Rijnders, D. H. A. Blank, and R. Ramesh. Critical thickness and orbital ordering in ultrathin $La_{0.7}Sr_{0.3}MnO_3$ films. *Physical Review B*, 78(9):094413, September 2008.

[42] D. Pesquera, G. Herranz, A. Barla, E. Pellegrin, F. Bondino, E. Magnano, F. Sanchez, and J. Fontcuberta. Surface symmetry-breaking and strain effects on orbital occupancy in transition metal perovskite epitaxial films. *Nature Communications*, 2012.

[43] D. Pesquera, A. Barla, M. Wojcik, E. Jedryka, F. Bondino, E. Magnano, S. Nappini, D. Gutiérrez, G. Radaelli, G. Herranz, F. Sánchez, and J. Fontcuberta. Strain-driven orbital and magnetic orders and phase separation in epitaxial half-doped manganite films for tunneling devices. *Phys. Rev. Applied*, 6:034004, Sep 2016.

[44] Yoshinori Konishi, Zhong Fang, Makoto Izumi, Takashi Manako, Masahiro Kasai, Hideki Kuwahara, Masashi Kawasaki, Kiyoyuki Terakura, and Yoshinori Tokura. Orbital-state-mediated phase-control of manganites. *Journal of the Physical Society of Japan*, 68(12):3790–3793, 1999.

[45] Marie-Bernadette Lepetit, Bernard Mercey, and Charles Simon. Interface effects in perovskite thin films. *Physical Review Letters*, 108(8):087202, February 2012.

[46] M. Veis, M. Zahradnik, R. Antos, S. Visnovsky, Ph. Lecoeur, D. Esteve, S. Autier-Laurent, J.-P. Renard, and P. Beauvillain. Interface effects and the evolution of ferromagnetism in $La_{2/3}Sr_{1/3}MnO_3$ ultrathin films. *Science and Technology of Advanced Materials*, 15(1):015001, February 2014.

[47] A. Tebano, C. Aruta, P. G. Medaglia, F. Tozzi, G. Balestrino, A. A. Sidorenko, G. Allodi, R. De Renzi, G. Ghiringhelli, C. Dallera, L. Braicovich, and N. B. Brookes. Strain-induced phase separation in $La_{0.7}Sr_{0.3}MnO_3$ thin films. *Phys. Rev. B*, 74:245116, Dec 2006.

[48] Y. Suzuki, H. Y. Hwang, S-W. Cheong, T. Siegrist, R. B. van Dover, A. Asamitsu, and Y. Tokura. Magnetic anisotropy of doped manganite thin films and crystals. *Journal of Applied Physics*, 83(11):7064–7066, 1998.

[49] A. M. Haghiri-Gosnet, J. Wolfman, B. Mercey, Ch. Simon, P. Lecoeur, M. Korzenski, M. Hervieu, R. Desfeux, and G. Baldinozzi. Microstructure and magnetic properties of strained $La_{0.7}Sr_{0.3}MnO_3$ thin films. *Journal of Applied Physics*, 88(7):4257–4264, 2000.

[50] F. Tsui, M. C. Smoak, T. K. Nath, and C. B. Eom. Strain-dependent magnetic phase diagram of epitaxial $La_{0.67}Sr_{0.33}MnO_3$ thin films. *Applied Physics Letters*, 76(17):2421–2423, 2000.

[51] M. Koubaa, A. M. Haghiri-Gosnet, R. Desfeux, Ph. Lecoeur, W. Prellier, and B. Mercey. Crystallinity, surface morphology, and magnetic properties of $La_{0.7}Sr_{0.3}MnO_3$ thin films: An approach based on the laser ablation plume range models. *Journal of Applied Physics*, 93(9):5227–5235, 2003.

[52] A. F. Marshall, L. Klein, J. S. Dodge, C. H. Ahn, J. W. Reiner, L. Mieville, L. Antagonazza, A. Kapitulnik, T. H. Geballe, and M. R. Beasley. Lorentz transmission electron microscope study of ferromagnetic domain walls in $SrRuO_3$: Statics, dynamics, and crystal structure correlation. *Journal of Applied Physics*, 85(8):4131–4140, 1999.

[53] Yevgeny Kats, Isaschar Genish, Lior Klein, James W. Reiner, and M. R. Beasley. Large anisotropy in the paramagnetic susceptibility of $SrRuO_3$ films. *Phys. Rev. B*, 71:100403, Mar 2005.

[54] L. Klein, J. S. Dodge, C. H. Ahn, J. W. Reiner, L. Mieville, T. H. Geballe, M. R. Beasley, and A. Kapitulnik. Transport and magnetization in the badly metallic itinerant ferromagnet $SrRuO_3$. *Journal of Physics: Condensed Matter*, 8(48):10111, 1996.

[55] A. Vailionis, H. Boschker, Z. Liao, J. R. A. Smit, G. Rijnders, M. Huijben, and G. Koster. Symmetry and lattice mismatch induced strain accommodation near and away from correlated perovskite interfaces. *Applied Physics Letters*, 105(13):131906, 2014.

[56] Jun He, Albina Borisevich, Sergei V. Kalinin, Stephen J. Pennycook, and Sokrates T. Pantelides. Control of octahedral tilts and magnetic properties of perovskite oxide heterostructures by substrate symmetry. *Phys. Rev. Lett.*, 105:227203, Nov 2010.

[57] Zhipeng Li, Dongsheng Song, Rong Yu, Binghui Ge, Zhenyu Liao, Yueliang Li, Shuai Dong, and Jing Zhu. Competing interfacial reconstruction mechanisms in $La_{0.7}Sr_{0.3}MnO_3/SrTiO_3$ heterostructures. *ACS Applied Materials & Interfaces*, 8(36):24192–24197, 2016. PMID: 27551951.

[58] Daisuke Kan, Ryotaro Aso, Riko Sato, Mitsutaka Haruta, Hiroki Kurata, and Yuichi Shimakawa. Tuning magnetic anisotropy by interfacially engineering the oxygen coordination environment in a transition metal oxide. *Nature Materials*, 2016.

[59] Xiaoyan Li, Ionela Lindfors-Vrejoiu, Michael Ziese, Alexandre Gloter, and Peter A. van Aken. Impact of interfacial coupling of oxygen octahedra on

ferromagnetic order in $La_{0.7}Sr_{0.3}MnO_3/SrTiO_3$ heterostructures. *Scientific reports*, 2017.

[60] Z. Liao, M. Huijben, Z. Zhong, N. Gauquelin, S. Macke, R. J. Green, S. Van Aert, J. Verbeeck, G. Van Tendeloo, K. Held, G. A. Sawatzky, G. Koster, and G. Rijnders. Controlled lateral anisotropy in correlated manganite heterostructures by interface-engineered oxygen octahedral coupling. *Nature Materials*, 2016.

[61] E. J. Moon, P. V. Balachandran, B. J. Kirby, D. J. Keavney, R. J. Sichel-Tissot, C. M. Schleputz, E. Karapetrova, X. M. Cheng, J. M. Rondinelli, and S. J. May. Effect of interfacial octahedral behavior in ultrathin manganite films. *Nano Letters*, 14(5):2509–2514, 2014. PMID: 24697503.

[62] S. Thomas, B. Kuiper, J. Hu, J. Smit, Z. Liao, Z. Zhong, G. Rijnders, A. Vailionis, R. Wu, G. Koster, and J. Xia. Localized control of curie temperature in perovskite oxide film by capping-layer-induced octahedral distortion. *Phys. Rev. Lett.*, 119:177203, Oct 2017.

[63] Narcizo M. Souza-Neto, Aline Y. Ramos, Hélio C. N. Tolentino, Emmanuel Favre-Nicolin, and Laurent Ranno. Local tetragonal distortion in $La_{0.7}Sr_{0.3}MnO_3$ strained thin films probed by x-ray absorption spectroscopy. *Phys. Rev. B*, 70:174451, Nov 2004.

[64] Heinrich Barkhausen. Zwei mit hilfe der neuen verstärker entdeckte erscheinungen. *Phys. Z*, 20:401, 1919.

[65] J. Pommier, P. Meyer, G. Pénissard, J. Ferré, P. Bruno, and D. Renard. Magnetization reversal in ultrathin ferromagnetic films with perpendicular anistropy: Domain observations. *Phys. Rev. Lett.*, 65:2054–2057, Oct 1990.

[66] Alexander Schwarz, Marcus Liebmann, Uwe Kaiser, Roland Wiesendanger, Tae Won Noh, and Dong Wook Kim. Visualization of the barkhausen effect by magnetic force microscopy. *Phys. Rev. Lett.*, 92:077206, Feb 2004.

[67] T. J. Yang, Venkatraman Gopalan, P. J. Swart, and U. Mohideen. Direct observation of pinning and bowing of a single ferroelectric domain wall. *Phys. Rev. Lett.*, 82:4106–4109, May 1999.

[68] Mirza Khurram Baig, Hassan Soleimani, and Noorhana Yahya. Domain wall motion and barkhausen effect in magnetic nanoparticles for EOR applications. *AIP Conference Proceedings*, 1787(1):050015, 2016.

[69] R. M. A. Azzam and N. M. Bashara. *Ellipsometry and Polarized Light*. North-Holland Publishing Company, 1977.

[70] Martin Zahradnik. Magnetooptical spectroscopy of $La_{2/3}Sr_{1/3}MnO_3$ ultrathin films, 2012.

[71] Miroslav Nyvlt. *Optical interactions in ultrathin magnetic film structures*. PhD thesis, Charles University, Prague, August 1996.

[72] S. Wittekoek, T. J. A. Popma, J. M. Robertson, and P. F. Bongers. Magneto-optic spectra and the dielectric tensor elements of bismuth-substituted iron garnets at photon energies between 2.2-5.2 eV. *Phys. Rev. B*, 12:2777–2788, Oct 1975.

[73] Frederic J. Kahn, P. S. Pershan, and J. P. Remeika. Ultraviolet magneto-optical properties of single-crystal orthoferrites, garnets, and other ferric oxide compounds. *Physical Review*, 186(3):891–918, October 1969.

[74] Martin Veis. *Optical interactions in thin films of selected magnetic oxides*. PhD thesis, Charles University, Prague, March 2009.

[75] Carl J. Ballhausen. *Introduction to Ligand Field Theory*. McGraw-Hill Book Company, Inc., 1962.

[76] Pochi Yeh. Optics of anisotropic layered media: A new 4×4 matrix algebra. *Surface Science*, 96:41–53, June 1980.

[77] Š. Višňovský. Magneto-optical ellipsometry. *Czechoslovak Journal of Physics B*, 36(5):625–650, May 1986.

[78] P. S. Pershan. Magneto-optical effects. *Journal of Applied Physics*, 38(3):1482–1490, March 1967.

[79] Š. Višňoský. *Optics in Magnetic Multilayers and Nanostructures*. Taylor & Francis Group, 2006.

[80] Howard M. Smith and A. F. Turner. Vacuum deposited thin films using a ruby laser. *Applied Optics*, 4(1):147–148, January 1965.

[81] G. Hass and J. B. Ramsey. Vacuum deposition of dielectric and semiconductor films by a CO_2 laser. *Applied Optics*, 8(6):1115–1118, June 1969.

[82] D. Dijkkamp, T. Venkatesan, X. D. Wu, S. A. Shaheen, N. Jisrawi, Y. H. Min-Lee, W. L. McLean, and M. Croft. Preparation of Y-Ba-Cu oxide superconductor thin films using pulsed laser evaporation from high T_C bulk material. *Applied Physics Letters*, 51(8):619–621, August 1987.

[83] A. Inam, M. S. Hegde, X. D. Wu, T. Venkatesan, P. England, P. F. Miceli, E. W. Chase, C. C. Chang, J. M. Tarascon, and J. B. Wachtman. As-deposited high T_C and J_C superconducting thin films made at low temperatures. *Applied Physics Letters*, 53(10):908–910, September 1988.

[84] Robert Eason, editor. *Pulsed Laser Deposition of Thin Films: Applications-Led Growth of Functional Materials*. John Wiley & Sons, Hoboken, New Jersey, second edition, 2007.

[85] K. R. Chen, J. N. Leboeuf, R. F. Wood, D. B. Geohegan, J. M. Donato, C. L. Liu, and A. A. Puretzky. Mechanisms affecting kinetic energies of laser-ablated materials. *Journal of Vacuum Science & Technology A*, 14(3):1111–1114, May 1996.

[86] W. Prellier, Ph. Lecoeur, and B. Mercey. Colossal-magnetoresistive manganite thin films. *Journal of Physics: Condensed Matter*, 13:R915–R944, November 2001.

[87] B.D. Josephson. Possible new effects in superconductive tunnelling. *Physics Letters*, 1(7):251 – 253, 1962.

[88] B. D. Josephson. The discovery of tunnelling supercurrents. *Rev. Mod. Phys.*, 46:251–254, Apr 1974.

[89] Materials properties measurement laboratory, available at https://mltl.eu.

[90] Eva Jesenska, Takahiro Hashinaka, Takayuki Ishibashi, Lukas Beran, Jan Dusek, Roman Antos, Kiyoshi Kuga, Ken-ichi Aoshima, Kenji Machida, Hidekazu Kinjo, and Martin Veis. Optical and Magneto-Optical Properties of $Gd_{22}Fe_{78}$ Thin Films in the Photon Energy Range From 1.5 to 5.5 eV. *Materials*, 9(1), 2016.

[91] Eva Jesenska, Tomohiko Yoshida, Kenji Shinozaki, Takayuki Ishibashi, Lukas Beran, Martin Zahradnik, Roman Antos, Miroslav Kučera, and Martin Veis. Optical and magneto-optical properties of Bi substituted yttrium iron garnets prepared by metal organic decomposition. *Opt. Mater. Express*, 6(6):1986–1997, Jun 2016.

[92] Mehmet C. Onbasli, Lukas Beran, Martin Zahradnik, Miroslav Kucera, Roman Antos, Jan Mistrik, Gerald F. Dionne, Martin Veis, and Caroline A. Ross. Optical and magneto-optical behavior of Cerium Yttrium Iron Garnet thin films at wavelengths of 200-1770 nm. *Scientific Reports*, 2016.

[93] Jeffrey McCord. Progress in magnetic domain observation by advanced magneto-optical microscopy. *Journal of Physics D: Applied Physics*, 48(33):333001, 2015.

[94] Michael C. Martin, G. Shirane, Y. Endoh, K. Hirota, Y. Moritomo, and Y. Tokura. Magnetism and structural distortion in the $La_{0.7}Sr_{0.3}MnO_3$ metallic ferromagnet. *Phys. Rev. B*, 53:14285–14290, Jun 1996.

[95] Q. Gan, R. A. Rao, and C. B. Eom. Control of the growth and domain structure of epitaxial $SrRuO_3$ thin films by vicinal (001) $SrTiO_3$ substrates. *Applied Physics Letters*, 70(15):1962–1964, 1997.

[96] Aurélie Solignac. *Realization and study of magnetic heterostructures based on the manganite $La_{0.7}Sr_{0.3}MnO_3$ for ultra-sensitive magnetic sensors*. Theses, Université Pierre et Marie Curie - Paris VI, November 2012.

[97] David Nečas and Petr Klapetek. Gwyddion: an open-source software for SPM data analysis. *Central European Journal of Physics*, 10:181–188, 2012.

[98] V. Holý and P. F. Fewster. Dynamical diffraction in layered systems - a quest for the final formula. *Journal of Physics D: Applied Physics*, 36(10A):A5, 2003.

[99] D. Pesquera, X. Marti, V. Holy, R. Bachelet, G. Herranz, and J. Fontcuberta. X-ray interference effects on the determination of structural data in ultrathin $La_{2/3}Sr_{1/3}MnO_3$ epitaxial thin films. *Applied Physics Letters*, 99(22):221901, 2011.

[100] X. Ke, C. Adamo, D. G. Schlom, M. Bernhagen, R. Uecker, and P. Schiffer. Low temperature magnetism in the perovskite substrate $DyScO_3$. *Applied Physics Letters*, 94(15):152503, 2009.

[101] X. Xiong, B. Dabrowski, O. Chmaissem, Z. Bukowski, S. Kolesnik, R. Dybzinski, C. W. Kimball, and J. D. Jorgensen. Correlation between coherent jahn-teller distortion and magnetic spin orientation in $La_{1-x}Sr_xMnO_3$. *Phys. Rev. B*, 60:10186–10192, Oct 1999.

[102] J. A. Woollam Co., Inc. *CompleteEASE^{TM} Data Analyses Manual, version 4.63*, 2011.

[103] A. S. Ferlauto, G. M. Ferreira, J. M. Pearce, C. R. Wronski, R. W. Collins, Xunming Deng, and Gautam Ganguly. Analytical model for the optical functions of amorphous semiconductors from the near-infrared to ultraviolet: Applications in thin film photovoltaics. *Journal of Applied Physics*, 92(5):2424–2436, 2002.

[104] S. Yamaguchi, Y. Okimoto, K. Ishibashi, and Y. Tokura. Magneto-optical Kerr effects in perovskite-type transition-metal oxides: $La_{1-x}Sr_xMnO_3$ and $La_{1-x}Sr_xCoO_3$. *Physical Review B*, 58(11):6862–6870, September 1998.

[105] Patrick Thoma, Manuel Monecke, Oana-Maria Buja, Dmytro Solonenko, Roxana Dudric, Oana-Tereza Ciubotariu, Manfred Albrecht, Iosif G. Deac, Romulus Tetean, Dietrich R.T. Zahn, and Georgeta Salvan. Polycrystalline $La_{1-x}Sr_xMnO_3$ films on silicon: Influence of post-Deposition annealing on structural, (Magneto-)Optical, and (Magneto-)Electrical properties. *Applied Surface Science*, 427:533 – 540, 2018.

[106] J. Mistrík, T. Yamaguchi, M. Veis, E. Lišková, Š. Višňovský, M. Koubaa, A.-M. Haghiri-Gosnet, Ph. Lecoeur, J.-P. Renard, W. Prellier, and B. Mercey. Magneto-optical and optical spectroscopic ellipsometries of $La_{2/3}Sr_{1/3}MnO_3$ thin films. *Journal of Applied Physics*, 99:08Q317–08Q317–3, April 2006.

[107] H. L. Liu, K. S. Lu, M. X. Kuo, L. Uba, S. Uba, L. M. Wang, and H.-T. Jeng. Magneto-optical properties of $La_{0.7}Sr_{0.3}MnO_3$ thin films with perpendicular magnetic anisotropy. *Journal of Applied Physics*, 99(4), February 2006.

[108] M. Quijada, J. Černe, J. R. Simpson, H. D. Drew, K. H. Ahn, A. J. Millis, R. Shreekala, R. Ramesh, M. Rajeswari, and T. Venkatesan. Optical conductivity of manganites: Crossover from Jahn-Teller small polaron to coherent transport in the ferromagnetic state. *Phys. Rev. B*, 58:16093–16102, Dec 1998.

[109] M. Veis, Š. Višovský, Ph. Lecoeur, A.-M. Haghiri-Gosnet, J.-P. Renard, P. Beauvillain, W. Prellier, B. Mercey, J. Mistrík, and T. Yamaguchi. Magneto-optic spectroscopy of $La_{2/3}Sr_{1/3}MnO_3$ films on $SrTiO_3$ (100) and (110) substrates. *Journal of Physics D: Applied Physics*, 42(19), September 2009.

[110] R. Rauer, G. Neuber, J. Kunze, J. Bäckström, M. Rübhausen, T. Walter, and K. Dörr. Magneto-optical investigation of spin polarisation of $La_{0.7}Ca_{0.3}MnO_3$ and $La_{0.7}Sr_{0.3}MnO_3$. *Journal of Magnetism and Magnetic Materials*, 290-291, Part 2:948–951, 2005. Proceedings of the Joint European Magnetic Symposia (JEMS' 04).

[111] L. Uba, S. Uba, L. P. Germash, L. V. Bekenov, and V. N. Antonov. Electronic structure and magneto-optical spectra of $La_xSr_{1-x}MnO_3$ perovskites: Theory and experiment. *Physical Review B*, 85(12):125124, March 2012.

[112] Chunlan Ma, Zhongqin Yang, and Silvia Picozzi. Ab initio electronic and magnetic structure in $La_{0.66}Sr_{0.33}MnO_3$: strain and correlation effects. *Journal of Physics: Condensed Matter*, 18(32):7717, 2006.

[113] G. Kresse and J. Furthmüller. Efficient iterative schemes for ab initio total-energy calculations using a plane-wave basis set. *Phys. Rev. B*, 54:11169–11186, Oct 1996.

[114] G. Kresse and J. Furthmüller. Efficiency of ab-initio total energy calculations for metals and semiconductors using a plane-wave basis set. *Computational Materials Science*, 6(1):15 – 50, 1996.

[115] D. Petti, A. Stroppa, S. Picozzi, S. Brivio, M. Cantoni, and R. Bertacco. Effect of Au proximity on the LSMO surface: An ab initio study. *Journal of Magnetism and Magnetic Materials*, 324(17):2659 – 2663, 2012.

[116] Tomáš Bučko, Jürgen Hafner, and János G. Ángyán. Geometry optimization of periodic systems using internal coordinates. *The Journal of Chemical Physics*, 122(12):124508, 2005.

[117] Zhu Chen, Yong Zeng, Cheng-tao Yang, Bang-chao Yang, Sheng Wang, Jin-long Li, and Ming-xia Sun. Lattice constant alpha calculation of PZT films prepared by a new modified sol-gel method. *Journal of Electronic Science and Technology*, 3(2):168–171, 2005.

[118] Seung-Hyun Kim, Jeong-Suong Yang, Chang Young Koo, Jung-Hoon Yeom, Euijoon Yoon, Cheol Seong Hwang, Joon-Shik Park, Sung-Goon Kang, Dong-Joo Kim, and Jowoong Ha. Dielectric and Electromechanical Properties of $Pb(Zr,Ti)O_3$ Thin Films for Piezo-Microelectromechanical System Devices. *Japanese Journal of Applied Physics*, 42(9S):5952, 2003.

[119] Seok Kil Han, Su Jae Lee, Jeha Kim, and Kwang-Yong Kang. Measurement of Microwave Dielectric Constant for Ferroelectric $Pb(Zr,Ti)O_3$ Thin Films. *Journal of the Korean Physical Society*, 32:364–366, February 1998.

[120] D. Czekaj, M.J.M. Gomes, M. Vasilevskiy, M. Pereira, and M.P. Dos Santos. Deposition of PZT thin film and determination of their optical properties. *Journal of the European Ceramic Society*, 19(6):1489 – 1492, 1999.

[121] Ji-Ping Xu, Rong-Jun Zhang, Zhi-Hui Chen, Zi-Yi Wang, Fan Zhang, Xiang Yu, An-Quan Jiang, Yu-Xiang Zheng, Song-You Wang, and Liang-Yao Chen. Optical properties of epitaxial $BiFeO_3$ thin film grown on $SrRuO_3$-buffered $SrTiO_3$ substrate. *Nanoscale Research Letters*, 9(1):188, Apr 2014.

[122] D. Estève, T. Maroutian, V. Pillard, and Ph. Lecoeur. Step velocity tuning of $SrRuO_3$ step flow growth on $SrTiO_3$. *Phys. Rev. B*, 83:193401, May 2011.

[123] S.N. Bushmeleva, V.Yu. Pomjakushin, E.V. Pomjakushina, D.V. Sheptyakov, and A.M. Balagurov. Evidence for the band ferromagnetism in $SrRuO_3$ from neutron diffraction. *Journal of Magnetism and Magnetic Materials*, 305(2):491 – 496, 2006.

[124] H. Zijlstra. Coping with brown's paradox: The pinning and nucleation of magnetic domain walls at antiphase boundaries. *IEEE Transactions on Magnetics*, 15(5):1246–1250, Sep. 1979.

[125] D. T. Margulies, F. T. Parker, M. L. Rudee, F. E. Spada, J. N. Chapman, P. R. Aitchison, and A. E. Berkowitz. Origin of the Anomalous Magnetic Behavior in Single Crystal Fe_3O_4 Films. *Phys. Rev. Lett.*, 79:5162–5165, Dec 1997.

[126] J. C. Jiang, X. Q. Pan, and C. L. Chen. Microstructure of epitaxial $SrRuO_3$ thin films on (001) $SrTiO_3$. *Applied Physics Letters*, 72(8):909–911, 1998.

[127] N. D. Zakharov, K. M. Satyalakshmi, G. Koren, and D. Hesse. Substrate temperature dependence of structure and resistivity of $SrRuO_3$ thin films grown by pulsed laser deposition on (100) $SrTiO_3$. *Journal of Materials Research*, 14(11):4385–4394, 1999.

[128] Sang Ho Oh, Ju Hyung Suh, and Chan Gyung Park. Defects in Strained Epitaxial $SrRuO_3$ Films on $SrTiO_3$ Substrates. *MATERIALS TRANSACTIONS*, 48(10):2556–2562, 2007.

[129] L. Straka, L. Fekete, and O. Heczko. Antiphase boundaries in bulk Ni-Mn-Ga Heusler alloy observed by magnetic force microscopy. *Applied Physics Letters*, 113(17):172901, 2018.

List of Abbreviations

AF	-	antiferromagnetic
AFM	-	atomic force microscopy
APB	-	anti-phase boundaries
CCD	-	charge-coupled device
CMR	-	colossal magnetoresistance
DC	-	direct current
DE	-	double-exchange
DOS	-	density of states
DSO	-	$DyScO_3$
DW(s)	-	domain wall(s)
IBE	-	ion beam etching
LAO	-	$LaAlO_3$
LD	-	linear dichroism
LSAT	-	$(LaAlO_3)_{1/3}(Sr_2AlTaO_6)_{2/3}$
LSMO	-	$La_{2/3}Sr_{1/3}MnO_3$
MBE	-	molecular beam epitaxy
MFM	-	magnetic force microscopy
MO	-	magneto-optical
MOCVD	-	metalorganic chemical vapour deposition
MOKE	-	magneto-optical Kerr effect
MPMS	-	Magnetic Properties Measurement System
NGO	-	$NdGaO_3$
OOC	-	oxygen octahedra coupling
OOR	-	oxygen octahedra rotations
PLD	-	pulsed laser deposition
PZT	-	$PbZr_{1/2}Ti_{1/2}O_3$
RF	-	radio frequency
RHEED	-	reflection high-energy electron diffraction
RSM(s)	-	reciprocal space map(s)
RSO	-	reciprocating sample option
SE	-	spectroscopic ellipsometry
SQUID	-	superconducting quantum interference device
SRO	-	$SrRuO_3$
TDOS	-	total density of states
XAS	-	X-ray absorption spectroscopy
XRD	-	X-ray diffraction

List of publications

1. **M. Zahradník**, T. Maroutian, M. Zelený, L. Horák, G. Kurij, T. Maleček, L. Beran, Š. Višňovský, G. Agnus, Ph. Lecoeur, and M. Veis. Electronic structure of $La_{2/3}Sr_{1/3}MnO_3$: Interplay of oxygen octahedra rotations and epitaxial strain. *Phys. Rev. B*, 99(19):195138, May 2019.

2. **M. Zahradník**, K. Uhlířová, T. Maroutian, M. Veis, G. Kurij, G. Agnus, and Ph. Lecoeur. Magnetic domain wall motion in $SrRuO_3$ thin films. *J. Magn. Magn. Mater.*, under review.

3. M. Veis, J. Minár, G. Steciuk, L. Palatinus, C. Rinaldi, M. Cantoni, D. Kriegner, K. K. Tikuišis, J. Hamrle, **M. Zahradník**, R. Antoš, J. Železný, L. Šmejkal, X. Marti, P. Wadley, R. P. Campion, C. Frontera, K. Uhlířová, T. Duchoň, P. Kužel, V. Novák, T. Jungwirth, K. Výborný. Band structure of CuMnAs probed by optical and photoemission spectroscopy. *Phys. Rev. B*, 97(12):125109, March 2018.

4. Y. Zhang, C. T. Wang, X. Liang, B. Peng, H. P. Lu, P. H. Zhou, L. Zhang, J. X. Xie, L. J. Deng, **M. Zahradník**, L. Beran, M. Kučera, M. Veis, C. A. Ross, L. Bi. Enhanced magneto-optical effect in $Y_{1.5}Ce_{1.5}Fe_5O_{12}$ thin films deposited on silicon by pulsed laser deposition. *J. Alloys Compd.* 703:591-599, 2017.

5. M. C. Onbasli, L. Beran, **M. Zahradník**, M. Kučera, R. Antoš, J. Mistrík, G. F. Dionne, M. Veis, C. A. Ross. Optical and magneto-optical behavior of Cerium Yttrium Iron Garnet thin films at wavelengths of 200-1770 nm. *Sci. Rep.*, 6:23640, March 2016.

6. E. Jesenská, T. Yoshida, K. Shinozaki, T. Ishibashi, L. Beran, **M. Zahradník**, R. Antoš, M. Kučera, M. Veis. Optical and magneto-optical properties of Bi substituted yttrium iron garnets prepared by metal organic decomposition. *Opt. Mater. Express*, 6(6):1986-1997, 2016.

7. M. Veis, **M. Zahradník**, L. Ohnoutek, L. Beran, M. Kučera, X. Y. Sun, C. Zhang, N. M. Aimon, T. Goto, M. C. Onbasli, D. H. Kim, H. K. Choi, C. A. Ross. Magneto-optical studies of $SrGa_{0.7}Co_{0.3}O_{3-\delta}$ perovskite thin films with embedded cobalt nanoparticles. *J. Appl. Phys.*, 117(17):17A746, May 2015.

8. M. Veis, L. Beran, **M. Zahradník**, R. Antoš, L. Straka, J. Kopeček, L. Fekete, O. Heczko. Magneto-optical spectroscopy of ferromagnetic shape-memory Ni-Mn-Ga alloy. *J. Appl. Phys.*, 115(17):17A936, May 2014.

9. M. Veis, M. Kučera, **M. Zahradník**, R. Antoš, J. Mistrík, L. Bi, H.-S. Kim, G. F. Dionne, C. A. Ross. Optial and magneto-optical properties of Co-doped $CeO_{2-\delta}$ films in the 0.5 to 4 eV range. *J. Appl. Phys.*, 115(17):17A940, May 2014.

10. M. Veis, **M. Zahradník**, R. Antoš, Š. Višňovský, Ph. Lecoeur, D. Esteve, S. Autier-Laurent, J.-P. Renard, P. Beauvillain. Interface effects and

the evolution of ferromagnetism in $La_{2/3}Sr_{1/3}MnO_3$ ultrathin films. *Sci. Technol. Adv. Mater.*, 15(1):015001, February 2014.

université PARIS-SACLAY

ÉCOLE DOCTORALE
Physique et ingénierie : électrons, photons, sciences du vivant (EOBE)

Titre : Contrôle dynamique de l'aimantation pour applications spintroniques étudié par des méthodes magnéto-optiques

Mots clés : effet Kerr magnéto-optique, dépôt par ablation laser pulsé, contrainte épitaxiale, tenseur de permittivité, oxydes pérovskites

Résumé : Deux mécanismes importants reliant la préparation des couches ultraminces d'oxydes magnétiques à leurs propriétés physiques ont été étudiés dans ce travail. En premier lieu, l'influence de la contrainte épitaxiale sur les propriétés magnéto-optiques de la manganite $La_{2/3}Sr_{1/3}MnO_3$ (LSMO) a été étudiée. Les couches ultraminces ont été déposées par ablation laser pulsé sur quatre substrats différents, ce qui a fourni différentes valeurs statiques de la contrainte épitaxiale. Les propriétés magnétiques ont été révélées comme se détériorant avec l'augmentation de la contrainte, ce qui était prévisible à cause de la distorsion grandissante de la maille unitaire ainsi qu'à cause de l'effet de la couche magnétiquement inerte. La combinaison de l'ellipsométrie spectroscopique et de la spectroscopie Kerr magnéto-optique a été utilisée afin de déterminer les spectres des éléments diagonaux et non diagonaux du tenseur de permittivité. L'étude des éléments non-diagonaux a confirmé la présence déjà rapportée de deux transitions électroniques dans les spectres de toutes les couches. De plus, elle a révélé une autre transition électronique autour de l'énergie de 4.3 eV, mais seulement dans les spectres des couches déposées avec une contrainte compressive. Nous avons proposé la classification de cette transition comme une transition paramagnétique du champ cristallin Mn $t_{2g} \rightarrow e_g$. Cette classification a été confortée par des calculs *ab initio*. Nous avons ainsi montré le rôle clé de la contrainte dans le contrôle des propriétés magnéto-optiques des couches pérovskites ultraminces. En revanche, l'application dynamique de la contrainte par l'utilisation d'une sous-couche piézoélectrique est restée peu concluante. Le transfert de la contrainte entre la sous-couche piézoélectrique et la couche LSMO nécessite des améliorations ultérieures. En second lieu, l'influence de la désorientation du substrat a été étudiée par rapport à la dynamique de l'aimantation dans l'oxyde $SrRuO_3$ (SRO). Comme attendu, nous avons trouvé qu'un grand angle de désorientation mène à la suppression de la croissance de plusieurs variants cristallographiques du SRO. Au moyen de la microscopie à force magnétique, nous avons montré que la présence de plusieurs variants de SRO mène à l'augmentation de la densité de défauts agissant comme points d'ancrage ou de nucléation pour les domaines magnétiques. Nous avons donc montré que l'emploi d'un substrat vicinal est important pour la fabrication des couches ultraminces de SRO de haute qualité, avec une faible densité de défauts cristallographiques et d'excellentes propriétés magnétiques.

Université Paris-Saclay
Espace Technologique / Immeuble Discovery
Route de l'Orme aux Merisiers RD 128 / 91190 Saint-Aubin, France

ÉCOLE DOCTORALE
Physique et ingénierie : électrons, photons, sciences du vivant (EOBE)

Title : Dynamic control of magnetization for spintronic applications studied by magneto-optical methods

Keywords : magneto-optical Kerr effect, pulsed laser deposition, epitaxial strain, permittivity tensor, perovskite oxides

Abstract : Two important mechanisms in preparation of ultrathin films of magnetic oxides were systematically investigated in this work. First, influence of epitaxial strain on resulting magneto-optical properties of $La_{2/3}Sr_{1/3}MnO_3$ (LSMO) ultrathin films was studied. The investigated films were grown by pulsed laser deposition on four different substrates, providing a broad range of induced epitaxial strains. Magnetic properties were found to deteriorate with increasing value of the epitaxial strain, as expected due to the unit cell distortion increasingly deviating from the bulk and effect of the magnetically inert layer. A combination of spectroscopic ellipsometry and magneto-optical Kerr effect spectroscopy was used to determine spectra of the diagonal and off-diagonal elements of permittivity tensor. The off-diagonal elements confirmed presence of two previously reported electronic transitions in spectra of all films. Moreover, they revealed another electronic transition around 4.3 eV only in spectra of films grown under compressive strain. We proposed classification of this transition as crystal field paramagnetic Mn $t_{2g} \rightarrow e_g$ transition, which was further supported by *ab initio* calculations. A key role of strain in controlling electronic structure of ultrathin perovskite films was demonstrated. Dynamic application of strain via use of piezoelectric underlayer remained inconclusive, requiring further improvement of the strain transfer from the piezoelectric layer into the LSMO. Second, influence of substrate miscut on magnetization dynamics in $SrRuO_3$ (SRO) was studied. As expected we found that high miscut angle leads to suppression of multi-variant growth. By means of magnetic force microscopy we showed that presence of multiple SRO variants leads to higher density of defects acting as pinning or nucleation sites for the magnetic domains, which consequently results in deterioration of magnetic properties. We demonstrated that use of vicinal substrate with high miscut angle is important for fabrication of high quality SRO ultrathin films with low density of crystallographic defects and excellent magnetic properties.

Université Paris-Saclay
Espace Technologique / Immeuble Discovery
Route de l'Orme aux Merisiers RD 128 / 91190 Saint-Aubin, France